Low to High Strain Rate Characterization of DP600, TRIP780, AA5182-O

by

M. Taamjeed Rahmaan

A thesis

presented to the University of Waterloo

in fulfillment of the

thesis requirement for the degree of

Master of Applied Science

in

Mechanical Engineering

Waterloo, Ontario, Canada, 2015

ABSTRACT

Advanced High Strength Steels (AHSS) and aluminum alloys are currently of great interest in the automotive industry due to their superior strength-to-weight ratio and good formability. This research work presents the results of an investigation into the rate sensitivity of DP600, TRIP780, and AA5182-O, three sheet alloys that are viewed as candidates for automotive structural applications to reduce vehicle weight. The effect of strain rate on both the flow stress and anisotropy characteristics was examined. Uniaxial tensile tests are the standard method used to characterize the strain-rate dependent mechanical properties of sheet metals. Tensile tests were performed at room temperature under conditions ranging from quasi-static to high strain rate loading on the three alloys along three orientations (0°, 45°, and 90°) with respect to the rolling direction. An Instron servo-hydraulic testing machine, a Hydraulic Intermediate Strain Rate (HISR) apparatus, and a split-Hopkinson tensile bar apparatus were used for the low, intermediate, and high strain rate experiments, respectively. The longitudinal and width strains were measured with a biaxial extensometer for the quasi-static tests and using Digital Image Correlation (DIC) methods for the elevated strain rate tests. DP600 and TRIP780 showed moderate rate sensitivity while AA5182-O showed relatively low or even negative rate sensitivity. The Portevin–Le Châtelier (PLC) effect was observed in AA5182-O up to a strain rate of 1 s^{-1}. The PLC effect was considered the cause of the negative rate sensitivity observed in the material. The hardening behavior of the TRIP780 at a strain rate of 1000 s^{-1} differed from that observed at lower rates of strain. This difference is attributed to the effect of the adiabatic temperature rise on the transformation induced plasticity (TRIP) effect. An increase in strain rate from 0.001 to 100 s^{-1} led to an average increase of 85 and 110 MPa in engineering stress (at 0.10 engineering strain) for all three sheet orientations for DP600 and TRIP780, respectively. The degree of anisotropy, characterized in terms of the Lankford coefficients and the variation in flow stress with material orientation, was relatively insensitive to strain rate for all three alloys.

A primary objective of this work was to develop rate-dependent constitutive models suitable for metal forming and vehicle crash analysis. A number of constitutive fits, including Johnson-Cook, Zerilli-Armstrong, and a Voce hardening law with different strain rate functions, were considered. The Voce–Modified (VM) model with a combined logarithmic and exponential type strain rate term was able to capture the strain rate dependence of all three materials (along all three material directions) up to the end of uniform elongation. The one exception to this outcome was the TRIP780 behavior at a strain rate of 1000 s^{-1}.

The proposed Voce-Modified constitutive model was implemented within finite element simulations of the tensile experiments. The model provided good predictions of hardening response up until the onset of necking. A post-necking hardening response was added to the VM model (referred to as the VM-extrapolated or VME model) and calibrated to the post-necking measured response, providing accurate simulations of the tensile behavior well into the post-necking regime.

ACKNOWLEDGMENTS

First and foremost I would like to thank my supervisor, Prof. Michael J. Worswick for giving me the opportunity to be a part of his research team. His vast knowledge and systematic guidance in every step of my research elevated my work to a new and more significant level. His humbleness and passion for science motivated me to work through difficult problems. Lastly, I would also like to thank him for his continuous support and solicitous responses, making my Master’s research a pleasant and worthwhile experience. I would like to thank Automotive Partnership Canada (APC), Ford Research, Amino Corporation, and ArcelorMittal for the financial support towards my research work.

I would like to thank Dr. Alex Bardelcik and Dr. Jose Imbert for being the backbone of my work. They not only helped me to learn all the basic and intricate aspects of this work but also patiently guided me through every hurdle I had. I would also like to thank Dr. Cliff Butcher for his incredible help in the simulation and validation portions of this work. His extraordinary knowledge and expertise helped to shape my work in a meaningful way. Thanks to Dr. Srihari Kurkuri for having all the constructive discussions related to this work. I would like to thank Samuel Kim for helping with the low rate experiments. The work environment was always helpful and friendly with Yonathon, Nikky, Kaab, Luke, Dariush, Nima, Rayan, Armin, Harpreet, Rohit, Ekta, Amir, Sante, Delawar, Chris, Luis and everybody else around, thanks guys.

The experimental portion of this work would not be completed without the continuous help and assistance from MME technical experts. There was only handful of days when I didn’t bother them with critical problems. Tom Gawel deserves huge thanks for extending his selfless helping hand every time I bumped into issues in the lab. Remarkable expertise and support from Jeff Wemp, Eckhard Budziarek, Neil Griffett and Andy Barber are much appreciated. An important role was played by the engineering machine shop experts to prepare the specimens and expedite the machining work whenever it was needed. I owe big thanks to each member of the EMS team, especially Rick Forgett, Karl Janzen, Fred Bakker, Charlie Boyle, Rob Kaptein, Rob Kraemer, Mark Kuntz, and Jorge Cruz.

Finally, I would like to thank my family. Ammu–Abbu, all good in me is because of you and all the successes I will ever get in my life are dedicated to you. I try to work harder everyday by remembering the sacrifices you made for me. Ma–Baba, can't express enough gratitude for making me feel like your own son with endless love in such short time and keeping me in your prayers at all the time. Mamu, you are the peace of my mind and core of my happiness. Buin–Dula, your love always makes me feel so special and confident like nothing else can. You guys are the most wonderful combination of a guardian and true friend to me. Sebring, I'm truly glad to have you as my beloved friend and a sister from another mother, I always wanted a younger sister. Last but not the least, my beautiful wife and the greatest support of my life in every up and down, I don't think I could ever accomplish anything without you being in my side. Your love, tolerance, intelligence, and humor are the energy of my hard work. I love each one of you a lot; this work would not be even initiated without the encouragements from all of you.

For my loving family

TABLE OF CONTENTS

LIST OF FIGURES

LIST OF TABLES

CHAPTER 1

INTRODUCTION

The current environmental challenges and need to increase fuel efficiency have led to the demand to incorporate lightweight metal alloys within automotive structures and body panels to reduce overall product weight, while maintaining strength and crash performance. The weight of the automotive body and chassis structures can potentially be reduced while maintaining a sufficient amount of strength and formability by using high strength steels and lower density materials such as aluminum. Advanced High Strength Steels (AHSS) and aluminum alloys are attractive for light weighting applications due to their superior strength-to-weight ratio. Compared to other materials, the percentage of steels used in vehicles in North America has increased from approximately 53–55 percent to approximately 60 percent between 1980 and 2010 [1]. The usage of aluminum materials has also increased by over 80 percent in automotive applications in order to reduce vehicle weight and improve corrosion resistance [2]. Dual Phase (DP) and Transformation Induced Plasticity (TRIP) steels are typical examples of AHSS steels that have been adopted by the automotive industry, while 5000-series aluminum alloys are commonly utilized for building inner body panels [2]. Understanding the behavior of these materials under different strain rate conditions is required to further their application within the automotive industry.

In automobile crash events, deformation occurs at strain rate on the order of 10^2 s^{-1}, with local hinge points and folds reaching strain rates as high as 10^3 s^{-1} [3]. Therefore, it is important to understand the low ($10^{-3} – 10^0$ s^{-1}), intermediate ($10^1 – 10^2$ s^{-1}), and high strain rate (10^3 $s^{-1}\geq$) behavior of steel and aluminum metals in order to develop accurate constitutive models for the simulation of metal forming processes and in-service dynamic loading such as during vehicle crash. The strain rate dependent behavior of metal alloys necessitate the development of constitutive models based on low to high strain rate experimental data for improved crash modeling [4].

In addition to capturing material stress-strain behavior over a range of strain rates, the anisotropy (r–value) of automotive sheet metals may vary with strain rate, the characterization of which is another motivation behind the current work. Although work has been done to characterize and model the stress-strain behavior of these metal alloys from quasi-static to high strain rate conditions [4-7], studies of the effect of strain rate on their anisotropic response is limited.

In this work, the low to high strain rate behavior of DP600, TRIP780, and AA5182-O was measured to obtain the strain rate dependant constitutive data. The strain rate-dependant characterization of these materials can be used not only in numerical modeling of vehicle crash and high speed metal forming process, but also for machining, armor and anti-armor studies as well as for basic scientific understanding. The material anisotropy is characterized in terms of the differences in stress-strain response and Lankford coefficient or r–value (the ratio of transverse to thickness strain during uniaxial tensile straining) [8] measured along different material orientations. The focus herein is on whether anisotropy changes with strain rate for the three alloys considered.

In order to characterize the materials over a complete range of strain rates, uniaxial tensile testing were conducted on each sheet material at nominal strain rates ranging from 0.001 to 1000 s^{-1}. Experiments were performed at room temperature on the as-received sheet materials along three orientations (0°, 45°, and 90°) with respect to the rolling direction in order to capture the anisotropic behavior of the materials. The low strain rate tests were conducted on an Instron servo-hydraulic tensile testing machine. The intermediate strain rate tests were carried out using a Hydraulic Intermediate Strain Rate (HISR) apparatus, and the high strain rate tests were carried out using a tensile split–Hopkinson bar apparatus. A biaxial extensometer was used to measure the longitudinal and width strains for the quasi-static testing while high speed Digital Image Correlation (DIC) techniques were employed to measure the longitudinal and width strains for the elevated strain rate tests.

In the current research, the parameters of different constitutive functions (including Johnson – Cook [9], Zerrili–Armstrong [10], and Voce constitutive models [11]) were fit to experimental results for each sheet materials. The true stress versus effective plastic strain (flow stress) curves was used to develop strain rate sensitive empirical constitutive models based on the Voce model referred herein as: the Voce-Modified and Voce-Modified-Extrapolated models. The proposed strain rate dependent models were validated successfully through finite element analysis simulations of the experiments.

For the remainder of this chapter, a review of the literature pertinent to this research is presented. This includes a general overview of the high strain rate characteristics of the materials as well as the review of characteristics and properties of dual phase (DP) and transformation induced plasticity (TRIP) steels, aluminum alloys, and their anisotropic behavior. A brief review of the different testing methods and apparatus utilized in this work to obtain constitutive data from low to high strain rates is presented, which is followed by a review of different material constitutive models used in the constitutive fitting portion of this work including the Johnson–Cook [9], Zerrili–Armstrong [10], and Voce constitutive models [11]. This encompasses the background material, experimental apparatus, and constitutive model information necessary to carry out this research.

1.1 HIGH STRAIN RATE MATERIAL BEHAVIOR

Over the years, strain rate sensitivity of different materials has been extensively studied in order to understand constitutive behavior under various strain rate conditions [12-15]. The flow stress of most metals has been shown to be dependent on the logarithm of the strain rate for a certain range of strain rates. It is generally accepted that strain rate-dependent behavior can be demarcated with three strain rate regimes which are defined by different mechanisms governing the plastic flow [16]. Figure 1.1 shows the three regions of strain rates for En3B steel [17]. In region I, the deformation is reported to be governed by the long-range internal stress fields due to dislocations, precipitate particles, grain boundaries, etc. [17,18]. The deformation in region II is controlled by the thermally activated dislocation motion, while drag mechanisms are typically attributed for the deformation that occurs within region III [16]. A transition from thermal activation mechanism to dislocation drag mechanism is often construed to be the cause of the increased strain rate sensitivity for many metals at higher strain rates [19]. However, this transition is likely to occur at strain rates on the order of $1x10^4$ s^{-1} [20]. Follansbee and Weertman [21] have concluded that the dislocation drag effects are not rate-controlling at strain rates below $1x10^4$ s^{-1}; hence thermally activated dislocation motion can be considered to be the primary governing mechanism over the range of strain rates considered in the present work (0.001-1000 s^{-1}).

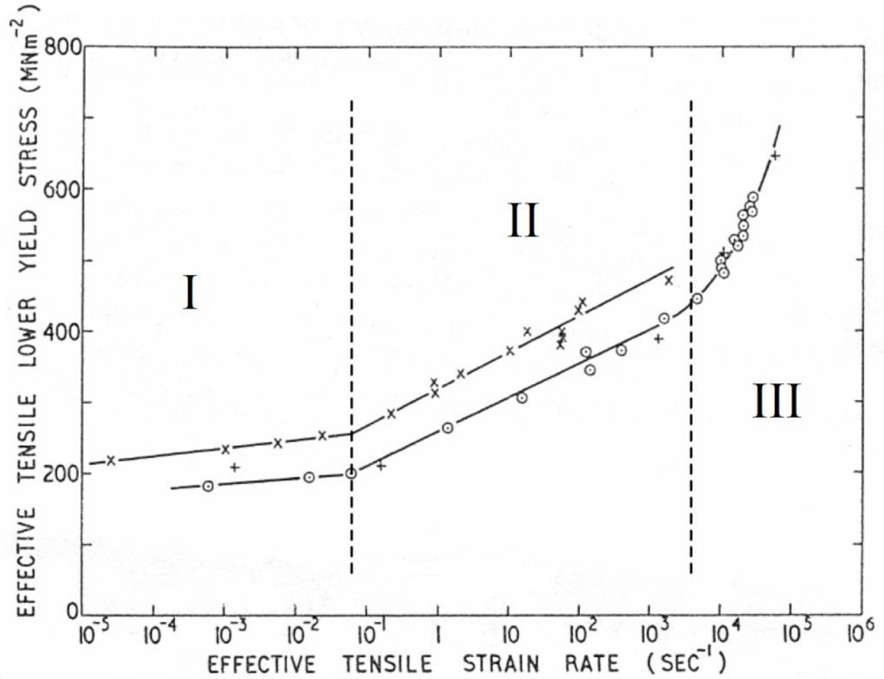

Figure 1.1: Effective tensile stress as a function of strain rate for En3B Steel [17]. The present author added the labels and vertical dashed lines.

Dislocations encounter obstacles such as solute atoms, vacancies, grain boundaries, and other dislocations during their movement through lattice [16]. As a result, the motions of the dislocations become more difficult. Energy can be provided to overcome these obstacles either by an increase in applied stress or by random thermal fluctuations at temperatures above absolute zero [22]. As shown in Figure 1.2(a), the thermal energy is sufficient to overcome the short-range obstacles, while the long-range obstacles that depend on the structure of the material cannot be overcome by thermal energy. Therefore, applied stress required to overcome the obstacle is consists of athermal and thermal components. The athermal component of this applied stress is a function of material structure alone, while the thermal component is a function of material structure, temperature, and strain rate [16].

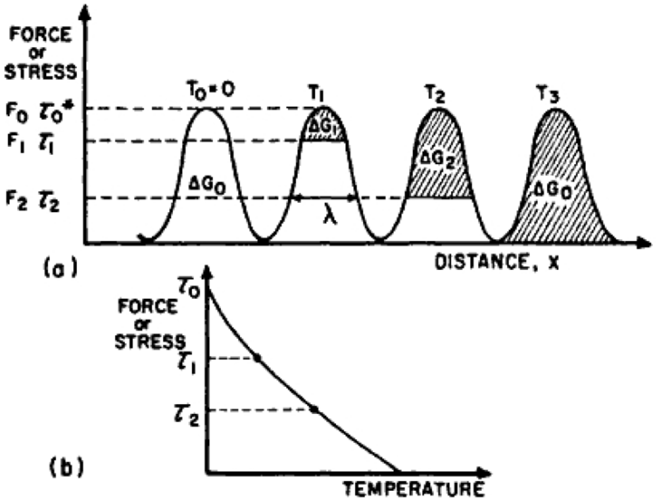

Figure 1.2: (a) Overcoming of barriers by thermal energy, (b) stress required to overcome obstacles as a function of temperature [16].

The average strain rate ($\dot{\varepsilon}_0$) can be described by an Arrhenius equation of the form presented in Eq. (1.1) [16]:

$$\dot{\varepsilon} = \dot{\varepsilon}_0 \exp\left(-\frac{\Delta G}{kT}\right) \qquad \text{Eq. (1.1)}$$

where, $\dot{\varepsilon}_0$ is the limiting strain rate, ΔG is the energy required by thermal fluctuations to overcome the obstacle, k is the Boltzmann constant, and T is the absolute temperature. Eq. (1.1) can be transformed to express the thermal energy ΔG as a function of temperature and strain rate as shown in Eq. (1.2). This equation shows that the short-range energy barrier (and the material strength) reduces as the temperature increases, while it increases with increasing strain rate.

$$\Delta G = kT \ln\left(\frac{\dot{\varepsilon}_0}{\dot{\varepsilon}}\right) \qquad \text{Eq. (1.2)}$$

The thermal energy ΔG can be expressed as a function of stress in a linear relationship of the form presented in Eq. (1.3) [23]; where, ΔG_0 is the activation energy at 0 K, V is the activation volume, σ is the applied stress, and σ^* is the athermal component of stress. According to Eq. (1.3), the additional thermal energy required to overcome obstacles decreases with an increase of applied stress which agrees with the diagram shown in Figure 1.2(b).

$$\Delta G\ (\sigma) = \Delta G_0 - V(\sigma - \sigma^*) \qquad \text{Eq. (1.3)}$$

The applied stress can be obtained by substituting Eq. (1.3) into Eq. (1.1), and solving for stress (σ):

$$\sigma = \sigma^* + \frac{\Delta G_0}{V} + \frac{kT}{V} ln\left(\frac{\dot{\varepsilon}_0}{\dot{\varepsilon}}\right) \qquad \text{Eq. (1.4)}$$

Typically, $\dot{\varepsilon}_0$ and ΔG_0 are assumed to be constant, while σ^* and V are taken to be functions of strain only [22,23]. Eq. (1.4) shows a logarithmic dependence of flow stress upon the strain rate, which agrees with the trends within region I and II of Figure 1.1. The material behavior of most metals has been shown to agree with this equation.

1.2 DUAL PHASE STEEL

The good combination of both strength and formability of Dual Phase (DP) steels has already led to their widespread use within the automotive industry. DP steel alloys are low-carbon steels which consist of hard martensitic islands dispersed throughout a soft ferritic matrix (shown in Figure 1.3). DP steels typically contain carbon (0.1-0.2 wt. %), manganese (1-2 wt. %), silicon (0.05-0.2 wt. %), and small amounts of several different micro-alloying elements, such as vanadium, titanium, molybdenum, nickel, and aluminum [24-27]. The dual phase microstructure is achieved by heating a low-carbon steel alloy up to the intercritical temperature and then rapidly quenching it to room temperature. The austenite phase within the ferrite matrix transforms to martensite during this quenching process which results in the ferrite-martensite dual phase microstructure [26-28].

A volumetric expansion occurs in the martensite particles after quenching which causes residual stresses at the martensite-ferrite interfaces [26,29]. As a result of the phase transformation during quenching, the mobile dislocation density within the soft ferrite matrix becomes very high which contributes to the excellent continuous yielding behaviour and accommodates the majority of the plastic deformation [29]. The role of the martensitic islands is to strengthen the material by introducing a high strength phase which introduces dislocation obstacles. The dispersed martensite islands are responsible for the strength of the material due to the presence of majority of the alloying elements within it [26-28]. Leidl et al. [29] showed that the residual stresses in the ferrite matrix increase with increasing amount of martensite content, which causes the yield strength to increase (shown in Figure 1.4). As seen in Figure 1.4, the total martensite content has a significant effect upon the stress-strain behavior of the material.

A partial conversion of austenite to epitaxial ferrite will occur in case of lower cooling rates during processing, while austenite may also be converted partially into bainite depending on the cooling rate [27,28,30]. The epitaxial ferrite forms a stress concentration in the martensite grains, which causes a drastic drop in strength and a slight increase in ductility [31]. Thus, it is essential to prevent the formation of epitaxial ferrite during quenching process in order to avoid the negative impact of epitaxial ferrite on the mechanical properties of the dual-phase steel. It is important to acknowledge that the annealing temperature and cooling rate in the quenching process mainly controls the total volume fraction of martensite in the final microstructure, and therefore plays an important role in determining the strength of the material [26-28].

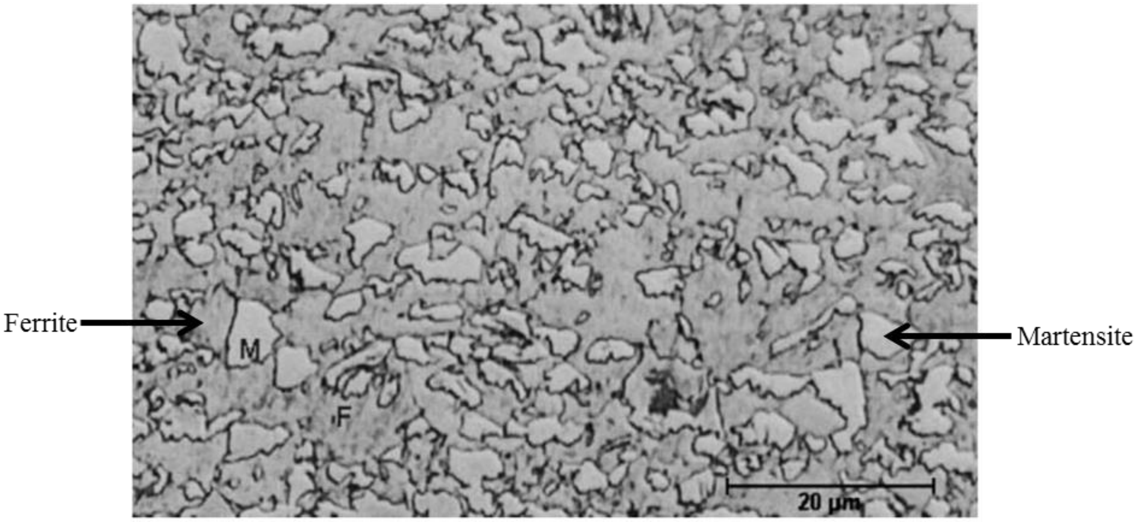

Figure 1.3: Microstructure of dual phase steel consisting ferrite and martensite [29]. Present author added the labels.

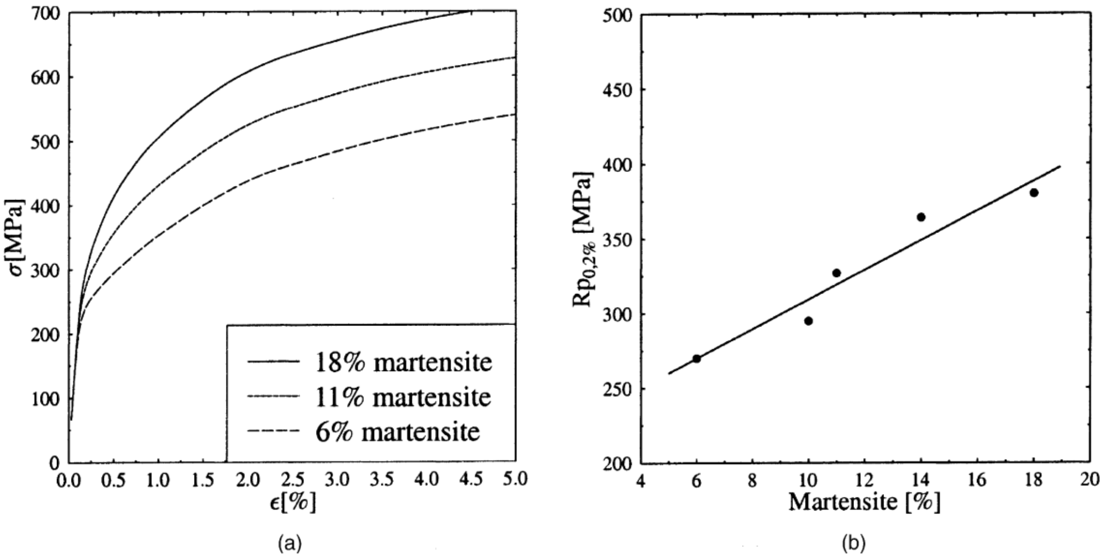

Figure 1.4: (a) Stress-strain curves for different martensite volume contents (b) increase in 0.2% yield strength with increasing martensite volume content [29].

Typically, three strain regions signifying different work hardening rate are used to outline the work hardening behavior of the dual-phase steel under uniaxial tension conditions [24]. Three stage work hardening behavior of dual-phase steel is analyzed by Cribb and Rigsbee [32] with respect to the deformation mechanisms correlated with microstructure. Rapid work hardening occurs in first stage, in which the residual stresses are eliminated and back stresses are created rapidly in the ferrite due to the plastic incompatibility of the two phases [32]. In the second stage, the constrained deformation of ferrite caused by the presence of the rigid martensite mitigates the decrease of work hardening. In the third stage, the work hardening is due to the formation of dislocation cell structures; further deformation in the ferrite is governed by dynamic recovery and cross-slip, and yielding of the martensite phase [24,32]. As seen in Figure 1.4a, the stresses below 0.5% strain corresponds to the first stage, between 0.5% and 2% strain corresponds to the second stage, and beyond 2% strain corresponds to the third stage of the work hardening behavior [6,24,32].

The strain rate sensitivity of dual-phase steels has been studied at various strain rates. Curtze et al. [33] performed tensile tests at different strain rates using an Instron 8800 servo-hydraulic testing machine and tensile split–Hopkinson bar apparatus. Moderate strain rate sensitivity was reported by Curtze et al. [33] for DP600 sheet metal alloys, but they only considered low (10^{-3}-10^{0} s^{-1}) and high strain rates (750-1250 s^{-1}). Beynon et al. [34] also performed tests on DP600 using a servo-hydraulic high rate impact machine at strain rates of 10^{-3} and 10^{2} s^{-1} and found positive rate sensitivity within the tested strain rate region as well.

Thompson [6] showed similar strain rate sensitivity for DP600 sheet metals for a range of strain rates from 0.003 to 800 s^{-1}. Although, Thompson [6] performed testing from low to high strain rates but utilized an Instrumented Falling Weight Impact (IFWI) apparatus for intermediate strain rate (30 s^{-1} and 80 s^{-1}) tests which resulted in a high level of noise in the data set, as shown in Figure 1.5.

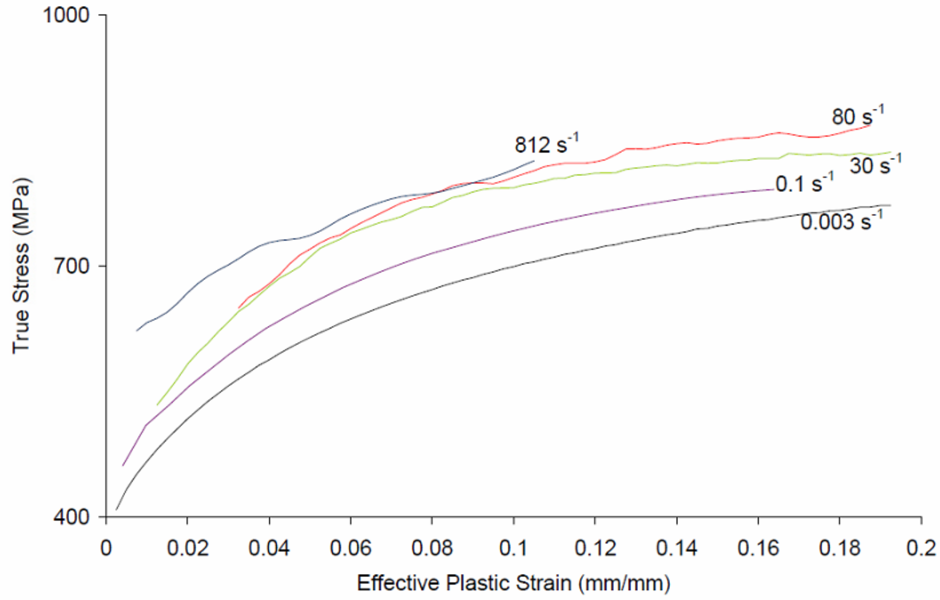

Figure 1.5: Flow stress curves for DP600 sheet specimen at room temperature and strain rates from 0.003 to 812 s^{-1} [6].

The mechanical properties and strain rate sensitivity of dual-phase steels have been studied in great detail. Dual-phase steel has good strain redistribution capacity due to high strain hardenability; thus, provides promising formability and mechanical properties. Given the good combination of strength and energy absorption capacity, dual-phase steel can be used to reduce the weight of the automotive structural parts by decreasing thickness, while maintaining satisfactory crashworthiness at the event of high velocity impact.

1.3 TRANSFORMATION INDUCED PLASTICITY (TRIP) STEEL

Multiphase TRIP steels have gained popularity in recent years due to their high strength and good formability, which is a result of their unique phase transformation characteristics. TRIP steels are essentially low-carbon low-alloy steels that contain a large amount of manganese (1.3-2 wt.%), aluminum (0.4-2 wt.%), and silicon (0.05-1.5 wt.%) as well as small amount of microalloying elements, such as chromium, molybdenum, and niobium [33,35,36]. The stability of the retained austenite is controlled by the manganese content, while silicon and/or aluminum are used to inhibit the precipitation of cementite [37]. Xia et al. [38] showed that an improved surface finish and weldability that is favourable to the auto industry can be achieved by using aluminum instead of silicon. The microstructure of TRIP steels contains retained austenite and bainite in a ferritic matrix, along with a small amount of martensite [35]. Isothermal holding just below bainite start temperature during the rapid cooling process followed by intercritical annealing transforms the austenite to bainite, while some of the austenite is retained in the microstructure [35,39,40]. Figure 1.6 shows the typical microstructure of TRIP steels [36]. During plastic deformation, the retained austenite transforms into hard martensite, strengthening the material [35].

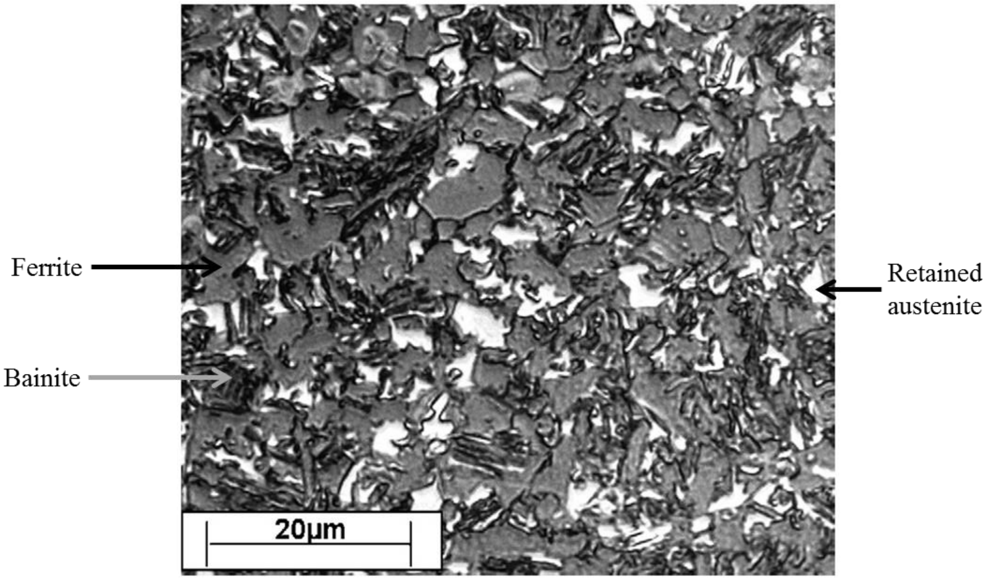

Figure 1.6: Optical microstructure of TRIP steel before deformation [36]. Present author added the labels.

Olson and Cohen [41,42] discussed two different mechanisms for martensitic transformation: stress-assisted transformation and strain-induced transformation. The type of transformation mechanism varies according to the imposed stress and resultant thermo-dynamical stability of retained austenite, as shown in Figure 1.7 [43]. The start temperature of martensitic transformation can be expressed by the parameter, M_S. Martensitic transformation that occurs below the M_S temperature (point A) is considered to be spontaneous, while stress-assisted transformation occurs in the elastic region between the M_S and M_S^σ temperatures along line AB [35,41-43]. The temperature M_S^σ, is defined as the temperature at which the stress required for stress-assisted martensitic transformation equals the yield strength of the parent austenite phase [41,42]. Martensite nucleation occurs within the stress-assisted region due to the driving force provided thermodynamically by the external applied stress which is lower than the austenite yield stress [35]. The strain-induced transformation occurs within the M_S^σ and M_D temperature range following the line BC, where the stress level of the plastic flow remains below that of stress-assisted nucleation [35,43]. M_D is defined as the highest temperature beyond which there is no austenite to martensite phase transformation [44]. Andrews [45] developed an empirical formula to define the start temperature of martensitic transformation (M_S), as shown in Eq. (1.5) (element concentration in weight percent):

$$M_S = 539 - 423\mathrm{C} - 30.4\mathrm{Mn} - 17.7\mathrm{Ni} - 12.1\mathrm{Cr} - 7.5\mathrm{Mo} \qquad \text{Eq. (1.5)}$$

Haidemenopoulos and Vasilakos [46,47] defined the stability of the retained austenite as follows:

$$\begin{aligned} M_S^\sigma = (6.7891 - 33.45X_C)^{-1}[A &+ 5712.6 - 78224X_C \\ &- 21542X_{Mn} + 18876X_C X_{Mn} \\ &+ \sigma_Y\left(0.715 + 0.3206\frac{\sigma_h}{\bar{\sigma}}\right)] \end{aligned} \qquad \text{Eq. (1.6)}$$

where,

$$A = \frac{\dfrac{2\alpha\gamma_s}{\rho}}{\ln\left\{-\dfrac{\ln(1-f)}{N_v^0 V_p}\right\}}$$

Here, X_C is the mole fraction of carbon in austenite, X_{Mn} is the mole fraction of manganese in austenite, σ_Y is the yield stress, σ_h is hydrostatic stress, $\bar{\sigma}$ is the equivalent stress, α is a material constant, γ_s is the martensitic nucleus specific interfacial energy, ρ is the density of atoms in the close packed plane, f is the fraction of particles transformed, N_v^0 is the total number of nucleation sites of all potencies, and V_p stands for austenite particle volume.

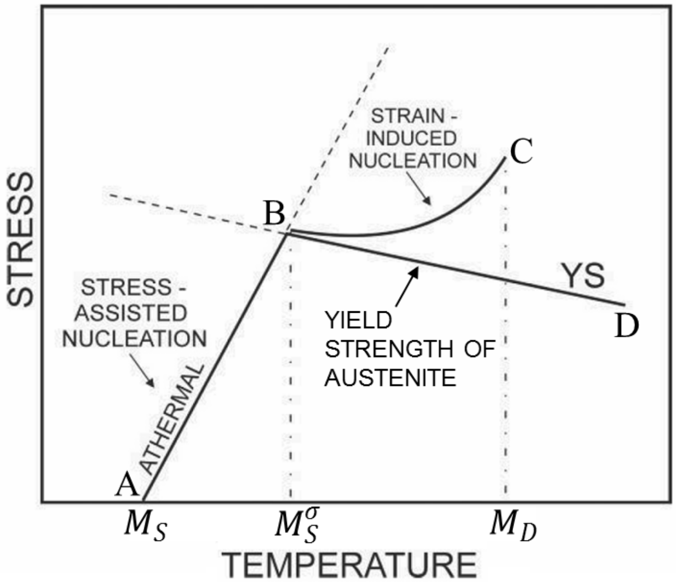

Figure 1.7: Thermo-dynamical stability of retained austenite [43].

The TRIP effect is controlled by the total amount of transformed retained austenite, the strain range over which transformation occurs, and the amount of retained austenite within the microstructure [48]. The martensitic transformation is influenced by the chemical composition, particle size, location of retained austenite in the microstructure, the resistance of the surrounding matrix, and the applied stress state [46,47]. The strain level at which the transformation of retained austenite to martensite occurs during plastic deformation depends on the chemical composition and size of the retained austenite grains [48].

An increased amount of retained austenite can be achieved with higher weight percentage of carbon content [49,50], as shown in Figure 1.8. Carbon content less than 0.5-0.6 wt.% and higher than 1.8 wt.% is considered to be optimum for TRIP steels [51]. Gajda and Lis [44] showed reductions in the volume fraction of retained austenite in the microstructure due to the martensitic transformation during the heat treatment process for higher cooling rates. The authors [44] reported that a cooling rate in the range from 10 to 20 °C/s should be applied in order to obtain typical multiphase TRIP microstructures [44].

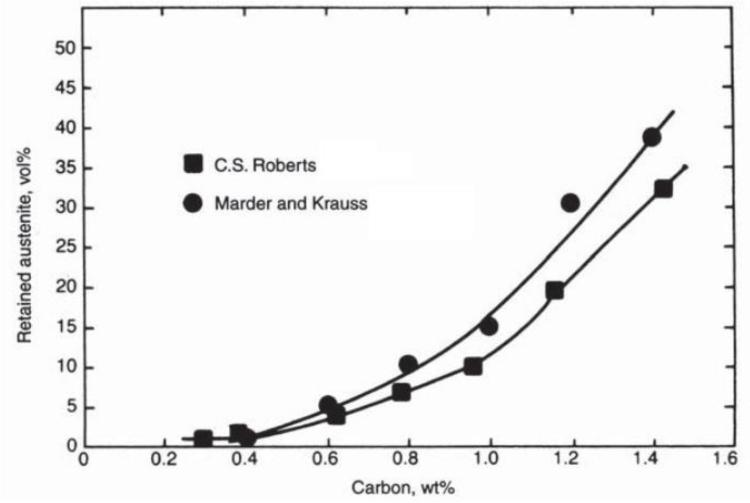

Figure 1.8: Variation of volume percent retained austenite with respect to carbon content [49,50].

Azrin et al. [52] performed tensile tests on TRIP steel at different strain rates (0.005, 0.05, and 0.5 min^{-1}) and showed strong dependence of the rate of transformation of retained austenite to martensite on strain rate. At a nominal strain rate of 0.5 min^{-1}, the authors reported a temperature rise within the specimen due to adiabatic heating that significantly lowered the rate of martensitic transformation [52]. The adverse effect of adiabatic heating is reported to be aggravated by a local increase of strain rates of up to 20 times the nominal crosshead strain rate associated with Lüders-band formation [35,52]. In order to produce a TRIP steels suitable for dynamic application, the authors in [52] suggested decreasing the apparent strain rate sensitivity by either eliminating the initial inhomogeneous flow or reducing the temperature sensitivity of the strain-induced martensitic transformation. Further theoretical investigation conducted by Tomita and Iwamoto [53] showed accelerated martensitic transformation resulting in an increase in the martensite volume fraction with an increase in strain rate for low strains, while martensitic transformation was reported to be reduced for the higher strains at the same strain rate. The decrease in martensitic transformation was explained by the increase in temperature due to the plastic work at higher strains.

More recently, Wei et al. [54] performed tensile testing on Si-Mn TRIP-aided steel at low (10^{-3} s^{-1}) and high (10^{3} s^{-1}) strain rates. A pneumatic indirect bar-bar tensile impact tester was used in their study. As shown in Figure 1.9a, the stress-strain curve for 1300 s^{-1} strain rate testing showed thermal softening at low (up to 8%) strain levels resulting in lower stress at 1300 s^{-1} strain rate than at 950 s^{-1} strain rate. However, the strength of the material recovered for the higher strain rate as the strain increased. The volume fraction of transformed retained austenite in TRIP steels with respect to strain rate and strain is thoroughly studied by Wei et al. [54] and Slycken et al. [36], who reported that under high strain rate conditions, the volume fraction of transformed martensite (from retained austenite) decreased due to the adiabatic temperature rise (as shown in Figure 1.9b). However, the increase in the volume fraction of transformed retained austenite is similar for higher strain under both high and quasi-static strain rate conditions. Kim et al. [4] conducted low to intermediate strain rate tests at rates up to 200 s^{-1} on TRIP780. The authors reported that for plastic strains up to 10%, the flow stress was higher at a low strain rate (10^{-3} s^{-1}) than it was at strain rates up to 10 s^{-1}, as shown in Figure 1.10; a form of negative strain rate sensitivity. This result suggests that the austenite to martensite transformation may have been retarded by the adiabatic temperature increase at the higher strain rate.

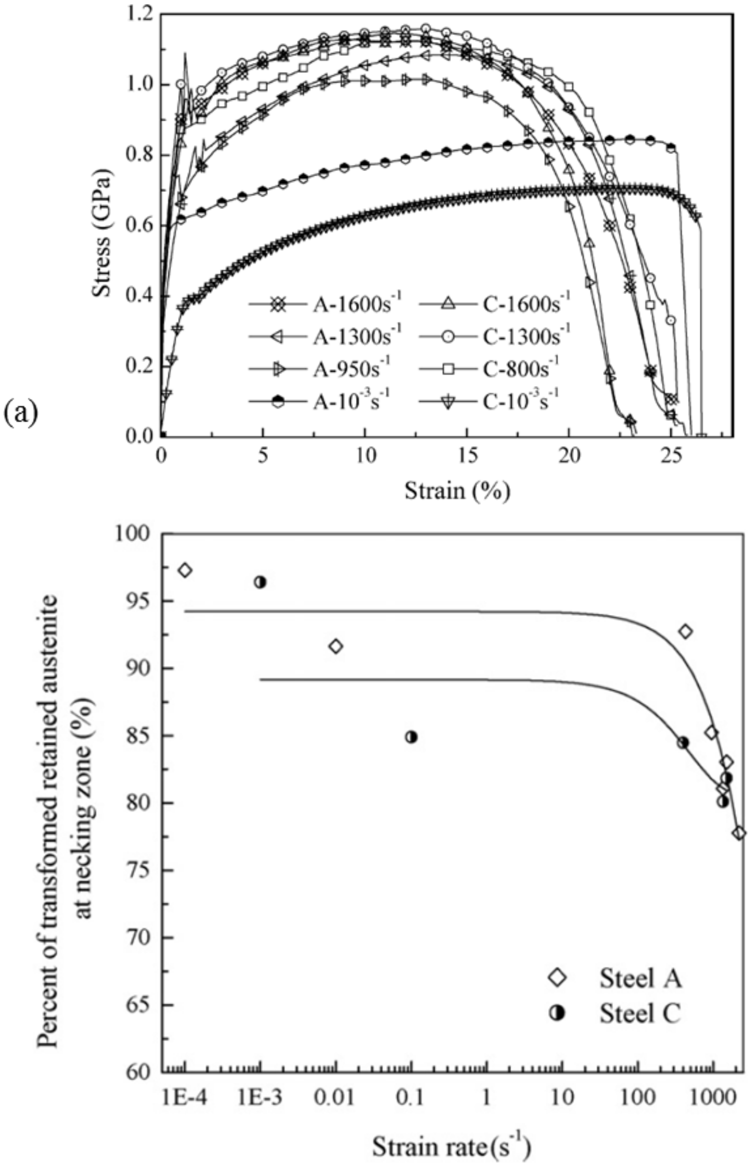

Figure 1.9: (a) Stress-strain curve and (b) volume fraction of transformed retained austenite as a function of strain rate at the necking zone for TRIP steels. Note: Steel A corresponds to the typical TRIP steels [54].

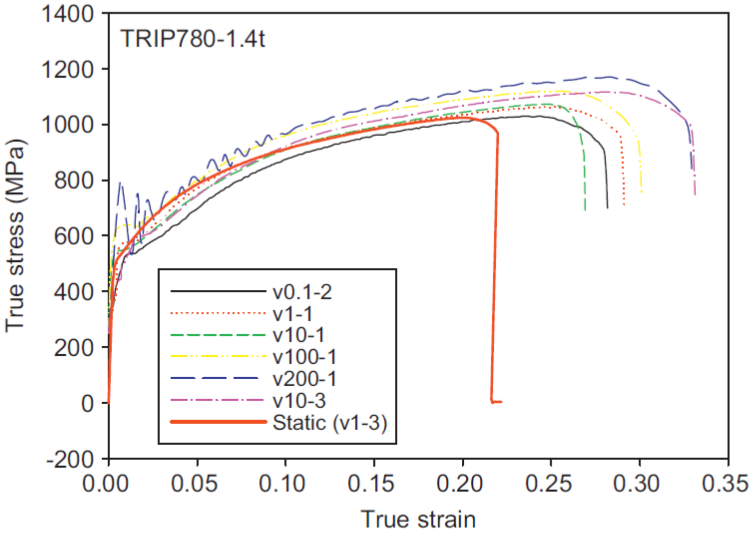

Figure 1.10: True stress-strain curves of TRIP780 steels under various strain rates. (Note: In the legend, v100-1 represents velocity strain rate 100 s^{-1} for sample number 1) [4].

Curtze et al. [33] performed tensile testing on TRIP 700 sheet material at strain rates ranging from 10^{-3} to 1250 s^{-1} using an Instron 8800 servo-hydraulic testing machine and a tensile split–Hopkinson bar device for low (10^{-3}-10^{0} s^{-1}) and high (750-1250 s^{-1}) strain rate testing, respectively. Unlike other researchers [4,36,52-54], Curtze et al. [33] have not reported any severe thermal softening or reduction in martensitic transformation rate at any given strain rate. Instead, the authors showed moderate strain rate sensitivity throughout the complete plastic deformation range tested. However, the strain hardening behavior is reported to be dependent strongly on the initial test temperature. Nevertheless, the transformation phenomena and behavior of the material at higher rates of strain are not well-understood.

Despite being a complex material, low alloy TRIP steels have gained prominence due to their superior strength and ductility, as well as only requiring a low content of expensive alloying elements. The high strength of TRIP steels has the capability to provide excellent crash and dent resistance, while enhanced stretch formability makes it a potential candidate for applications involving deep drawing processes. Thus, TRIP steels are of great interest to the automotive industry due to their good combination of high strength and formability at reasonable cost.

1.4 ALUMINUM ALLOYS

The density of aluminum alloys is approximately one-third that of steel, making them attractive for implementation within vehicle architectures. Within the automotive industry, 5000-series aluminum alloys are commonly utilized for deep drawn inner body panels [2]. The primary alloying element of 5000-series aluminum alloys is Mg, with Fe, Mn, and Si also present in their microstructure. A typical microstructure of AA5182 is shown in Figure 1.11[5]. Second phase particles and voids are usually found in the matrix. The second phase particles are essentially iron, manganese, or silicon compounds [5,55].

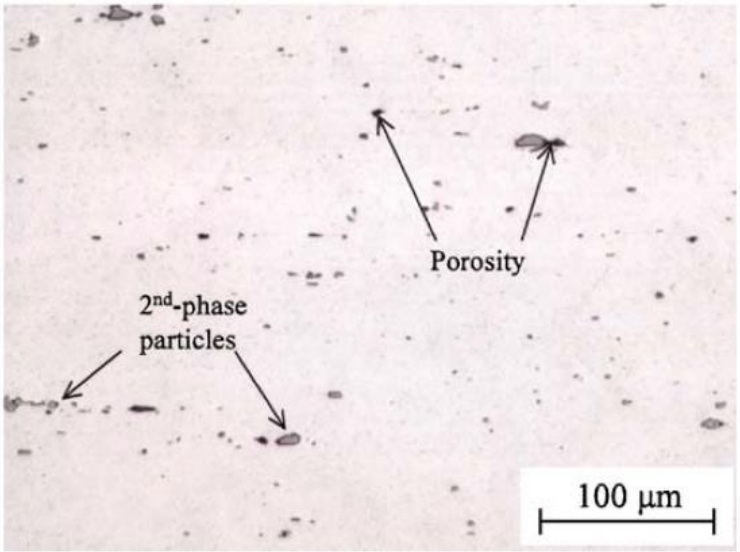

Figure 1.11: Optical micrograph of AA5182 in the long transverse plane, polished only [5].

The strain rate sensitivity of aluminum alloys has always been an important matter of discussion within the research community. Aluminum alloys are typically considered to have low strain rate sensitivity behavior at room temperature.

Smerd et al. [5] conducted room temperature tensile tests on AA5182 sheet metal at low (0.003 s^{-1}) and high (600-1,500 s^{-1}) strain rates using an Instron servo-hydraulic testing machine and a tensile split–Hopkinson bar apparatus for low and high strain rate testing, respectively. Comparing quasi-static and dynamic stress-strain response in the range of strain rates tested (shown in Figure 1.12), AA5182 was reported to be strain rate insensitive. Similarly, strain rate sensitivity studies were performed by Abotula and Chalivendra [56] by conducting compression tests on the same alloy at low (0.006 s^{-1}) and high (1,000-10,500 s^{-1}) strain rates. The authors showed a slight increase in flow stress at higher strain rates compared to quasi-static conditions. As seen in Figure 1.13, their data showed severe oscillations in the stress-strain curves at strain rates above 10^3 s^{-1}. The oscillations appeared in the stress-strain curve possibly as a result of wave reflection and distortion occurred in the split–Hopkinson bar apparatus and therefore, cannot be considered as the typical constitutive response [19]. Nevertheless, based on a lack of intermediate strain rate test data (10^0 to 10^2 s^{-1}), both studies [5,56] reported nearly zero strain rate sensitivity at room temperature for the range of strain rates tested.

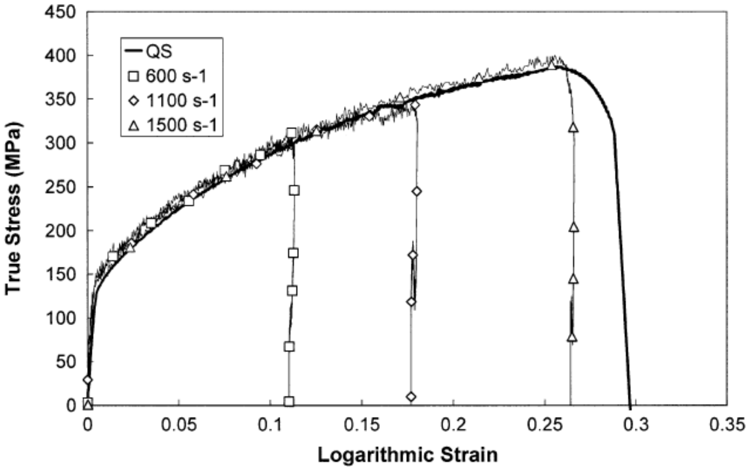

Figure 1.12: Effects of strain rate on flow stress for AA5182 [5].

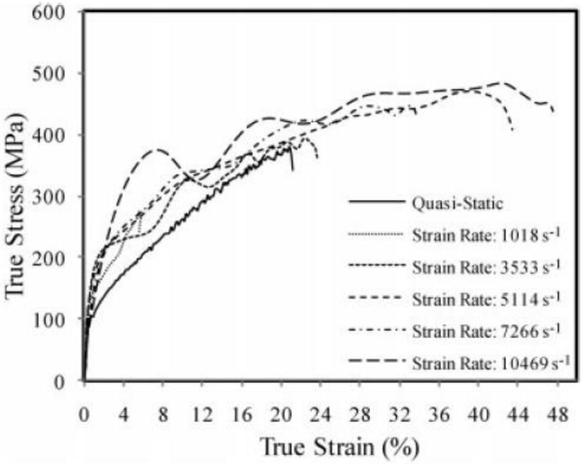

Figure 1.13: True compressive stress-strain curve for AA5182-O alloy [56].

Negative strain rate sensitivity has been observed for room temperature tensile testing of AA5182 at quasi-static strain rates ranging from 10^{-6}-1 s^{-1} by Lademo et al. [57], and for strain rates ranging from 7.05x10^{-6}–0.1 s^{-1} by Abbadi et al. [58], and Picu et al. [59]. Those studies attributed the negative strain rate sensitivity to the Portevin-Le Châtelier (PLC) effect which is a result of plastic strain inhomogeneity and appears as a serrated flow stress-strain curve at specific test temperatures and strain rates [58]. PLC is a macro-scale manifestation of nano-scale dynamic strain aging (DSA) caused by the smaller scale transient interactions between diffusing solute atoms and glide dislocations [60,61].

Different types of deformation bands induced by the PLC effect appear as different types of stress-strain curve serrations. Chihab et al. [62] showed the shapes of the classic serrations on the deformation curves by testing Al-5at%Mg alloy at low strain rates (up to 10^{-2} s^{-1}). The PLC bands are typically designated as type A, type B, and type C serrations, as shown in Figure 1.14 [62-64]. According to their investigation, type C bands characteristically occur at the strain rates equal or below 5x10^{-5} s^{-1}, type B bands occur in the range of strain rates between 10^{-4} and 10^{-3} s^{-1}, and type A bands occur at strain rates equal or higher than 5x10^{-3} s^{-1}.

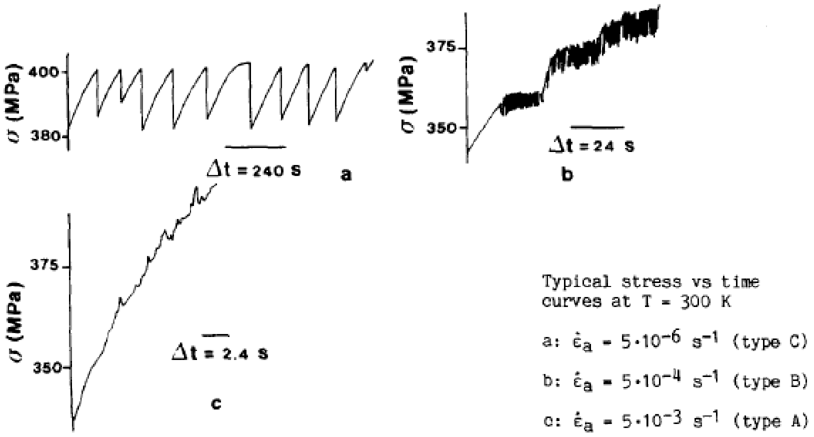

Figure 1.14: Typical stress vs. time curves at temperature of 300 K [62].

Ait-Amokhtar and Fressengeas [65] performed velocity driven tensile tests at room temperature on an Al-3.2% Mg alloy over a range of strain rates from 10^{-4} to 10^{-2} s^{-1}. The authors showed different types of PLC bands on the stress-strain curves at different strain rates, including a mixed band type A-B at the strain rate of 5x10^{-3} s^{-1}. The type C bands propagates randomly along a tensile sample, while type B appears as discontinuous propagation (hopping bands) and type A bands are typically characterized by continuous propagation [65]. The shapes or so-called “teeth” of different PLC bands are further investigated and well explained elsewhere [62-64,66].

Negative strain rate sensitivity of an annealed AA5182 at room temperature was also reported by Higashi et al. [55] for strain rates below 10^2 s^{-1}. Unlike the previously mentioned research [57-59,62,65], Higashi et al. [55] did not correlate the observed negative strain rate sensitivity to the PLC effect; rather, they suggested that the decrease in dislocation density resulting from the arrangement of the network-like deformation bands by dislocations during straining to be the main cause of the negative strain rate behavior.

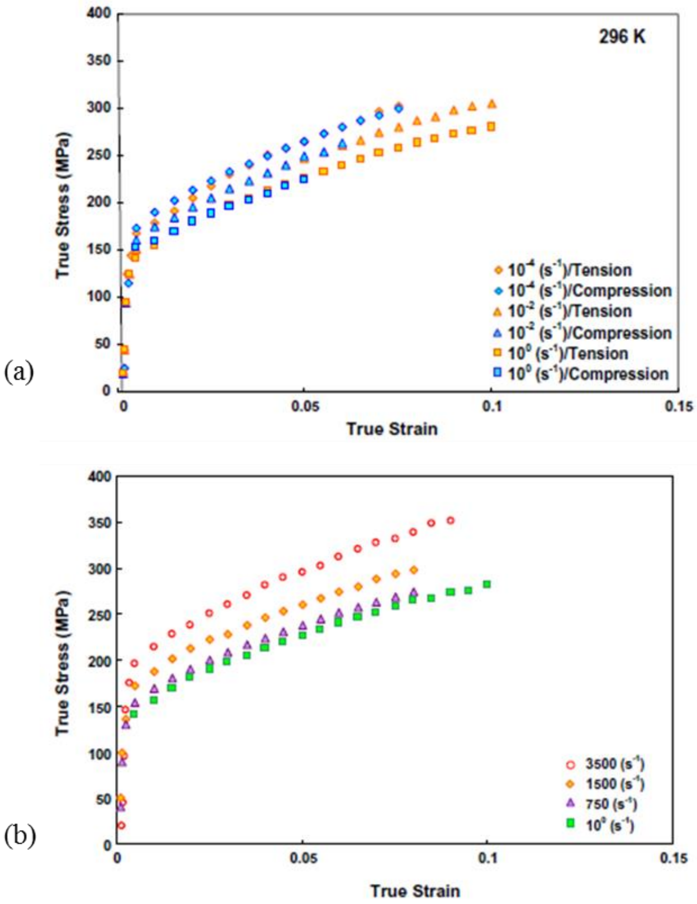

Figure 1.15: Stress-strain response for AA5182-O sheet material at 296 K (a) from compression and tensile testing at low strain rates and (b) at dynamic strain rates (from 10^0-3500 s^{-1}) [67].

More recently, Kabirian et al. [67] performed both tensile and compression tests on AA5182-O sheet material at low (10^{-4}-10^{0} s^{-1}) and high (750-3500 s^{-1}) strain rates using an MTS axial/torsion servo-hydraulic system and compression split–Hopkinson pressure bar apparatus, respectively. As seen in Figure 1.15a, the authors reported no asymmetry in the stress-strain responses between the tension and compression testing. At a temperature of 296 K and plastic strain of 0.05, moderate negative strain rate sensitivity was reported for an increase of strain rate from 10^{-4} to 10^{0} s^{-1} (as shown in Figure 1.15a). During the transition from the low (10^{0} s^{-1}) to high (above 750 s^{-1}) strain rate, a drastic increase in the flow stress was reported, as shown in Figure 1.15b. Although, the negative strain rate sensitivity was attributed to DSA therein, but no PLC effect in the experimental data was reported [67]. Due to the lack of intermediate strain rate (10^{1}-10^{2}) data, the level of strain rate at which the transition of strain rate sensitivity (from negative to positive) occurs was not well understood. Therefore, additional characterization of the rate sensitivity of 5000-series aluminum alloys is required to improve simulation of their forming and crashworthiness behavior.

1.5 ANISOTROPY

Directional variation of mechanical properties (or anisotropy) exists in most automotive sheet metal alloys. During the rolling operation, the grains acquire a non-random orientation distribution or crystallographic texture, leading to a change in directional response in the sheet plane [68]. Such crystallographic texture is manifest in sheet alloys as a difference in yield strength with direction relative to the sheet rolling direction. Furthermore, the Lankford coefficient or r-value, the ratio of width to thickness strain during uniaxial tensile testing, is no longer equal to unity indicating a difference in resistance to deformation in the in-plane versus through-thickness directions. [69].

In metal forming, the anisotropy of a sheet metal is important because it affects formability along different directions with respect to its rolling direction. Modern simulation techniques for crashworthiness prediction that account for material anisotropy are becoming more common. Finite element constitutive models accounting for sheet anisotropy in for the simulation of the sheet metal forming processes or crashworthiness need to be calibrated with respect to the measured anisotropy in order to accurately model the sheet behavior.

The r–value or Lankford coefficient is measured during uniaxial tensile testing and is calculated from the ratio of true plastic strain in the sample width versus thickness directions [70],

$$r = \frac{\varepsilon_w}{\varepsilon_t} \quad \text{Eq. (1.7)}$$

where, ε_w and ε_t are the true plastic width strain and true plastic thickness strain, respectively. The r–value will be unity for an isotropic sheet material, while r–values greater than unity indicate greater resistance to through-thickness thinning [71].

The attainable plastic strain ratio used for calculating the r–value is affected by the number of slip systems which can operate during the plastic deformation [72]. The plastic deformation of face-centered cubic (FCC) metal occurs on twelve equivalent systems, and r–values of less than 1 are typically obtained for commercial polycrystalline sheet [73]. However, the typical strain ratio value of metals such as aluminum is found to be around 0.6 [72]. In body-centered cubic (BCC) metals, the plastic deformation primarily occurs on four similar types of slip directions from a packet of slip planes. However, the plastic deformation of BCC metals can occur on more slip systems; therefore, a higher and lower plastic strain ratio can be obtained for such metals [72,74]. Heyer and Newby [75] reported that r–values up to 2.2 can be obtained for extra deep drawing low carbon steels.

Table 1.1 summarizes reported r-value data for the three alloys considered in the current study. Filho et al. [76] reported that the highest r–value within DP600 sheet occurs along the 45° orientation with respect to sheet rolling direction, while Wang et al. [77] found the highest r–value along the rolling direction (as shown in Table 1.1). Differing from these authors, Panda et al. [78] and Nasser et al. [79] reported the highest r–values for DP600 sheet at 90° to the rolling direction.

Room temperature uniaxial tensile testing was performed by Nasser et al. [79] on TRIP780 sheet to determine the r–values. As seen in Table 1.1, they report the highest r–value for TRIP780 sheet metal to occur at 45° to rolling direction, while Dunand et al. [80] measured the highest r–values at 90° to rolling direction.

Butuc et al. [81] and Brem et al. [82] reported minimal variation of the r–value along different orientations of AA5182 sheet, with values in the range 0.59-0.67. Higher r–values were reported along rolling direction by Butuc et al. [81], while Brem et al. [82] have found higher r–values along the transverse direction.

Table 1.1: r–values available in literature for DP600, TRIP780, and AA5182 sheet material along 0°, 45°, and 90° to rolling direction of the metal sheets.

	$r_{0°}$	$r_{45°}$	$r_{90°}$
DP600 (Filho et al.) [76]	0.674	1.035	0.998
DP600 (Wang et al.) [77]	1.160	0.670	1.020
DP600 (Panda et al.) [78]	0.800	0.960	1.030
DP600 (Nasser et al.) [79]	0.942	1.010	1.080
TRIP780 (Nasser et al.) [79]	0.498	0.872	0.583
TRIP780 (Dunand et al.) [80]	0.890	0.820	1.010
AA5182 (Butuc et al.) [81]	0.670	0.660	0.590
AA5182 (Brem et al.) [82]	0.957	0.934	1.058

Huh et al. [83] investigated the effect of strain rate on plastic anisotropy of DP780 and TRIP590 sheet at strain rates ranging from 0.001 to 100 s^{-1}. As seen in Figure 1.16, the authors [83] reported variation in yield stress and tensile strength with respect to the loading angle due to the in-plane anisotropy for the entire range of strain rates tested, as well as a moderate dependence of r–value upon the strain rate (Figure 1.17).

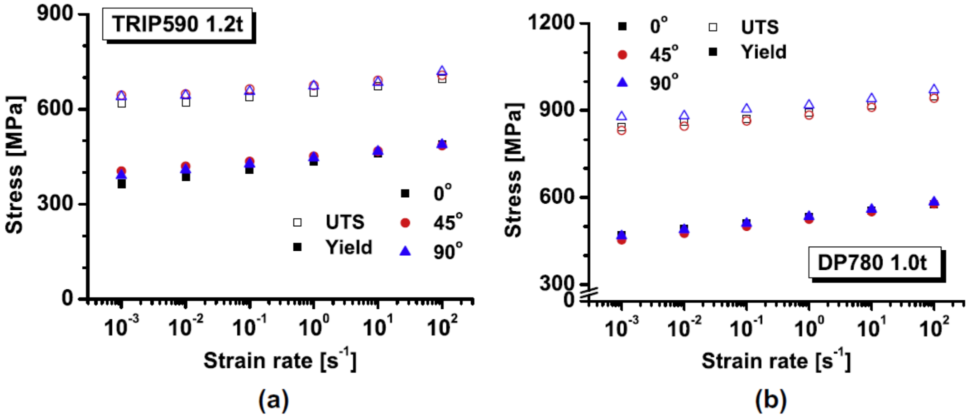

Figure 1.16: Yield stresses and ultimate tensile strength along 0°, 45°, and 90° to rolling direction of the metal sheet at various strain rates for: (a) TRIP590 (b) DP780 [83].

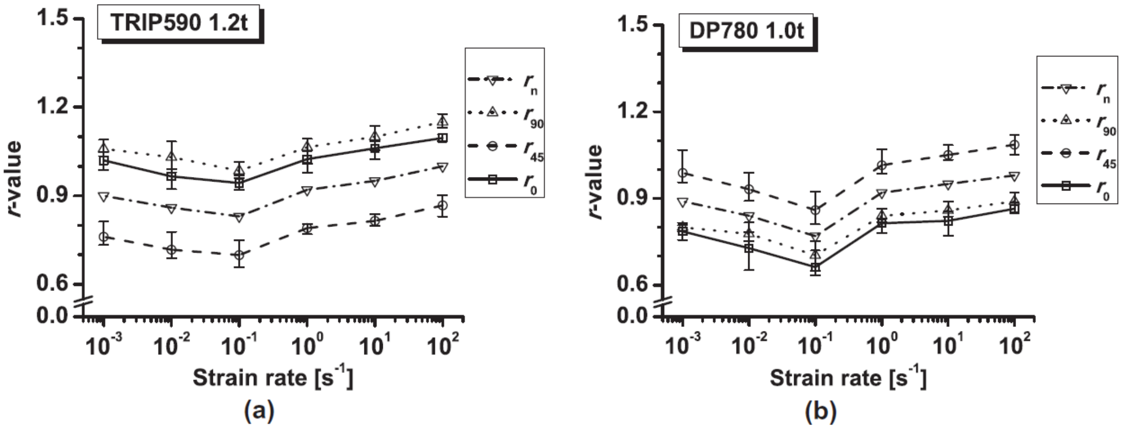

Figure 1.17: Distribution of r–values with respect to strain rate for (a) TRIP590 (b) DP780 [83].

In summary, most of the previous studies of the mechanical behavior of DP600 [27-30], TRIP780 [31,32] and AA5182-O [33,34] have reported mild to moderate anisotropy. Few studies have examined the variation in anisotropy with strain rate.

1.6 ELEVATED STRAIN RATE TESTING METHODS

1.6.1 Intermediate Strain Rate Testing

As discussed in section 1.1, the constitutive behavior of most metals is affected by the strain rate. The deformation occurs at strain rate higher than 10 s^{-1} is influenced by the effects of material inertia and stress wave propagation, causing a notable change in tensile properties of most metals [84]. The split–Hopkinson pressure bar apparatus, also known as the Kolsky bar [85] is a widely used experimental technique for dynamic material characterization at higher strain rates. However, as discussed in section 1.6.2, the Kolsky [85] theory for the split–Hopkinson bar apparatus is based on one-dimensional wave propagation assumption; therefore, it is no longer valid at the strain rates less than 500 s^{-1} due to the simultaneous deformation involving both quasi-static and dynamic aspects [84]. Thus, the split–Hopkinson bar apparatus is not suitable for intermediate strain rate (10^1-10^2) testing.

The material properties at the intermediate strain have been obtained using several different loading methods, such as mechanical, pneumatic, and servo-hydraulic [16]. Dudder [86], Ambur et al. [87], and Thompson [6] obtained the mechanical properties of sheet specimens using a drop weight testing method, while Hawkyard et al. [88] and Bouix et al. [89] have implemented a cam platostometer set-up and a flywheel apparatus, respectively for intermediate strain rate testing. The dynamic nature of drop weight-type testing method poses a challenge due to the inertia of the dropped weight and associated ringing effects in the measured results [6]. At present, so-called "fast" servo-hydraulic tensile testing machines are typically employed in intermediate strain rate testing [34,84,90-92].

A Hydraulic Intermediate Strain Rate (HISR) apparatus was developed at the University of Waterloo [92,93] to perform uniaxial tension tests at the strain rates up to 100 s^{-1}. The HISR apparatus utilizes a slack type engagement assembly which accelerates up to a constant velocity, at which point it contacts a lower grip that pulls the specimen in tension [92,94]. An enhanced laser velocity system (ELVS) was implemented to measure the specimen elongation across the shoulders of the specimen, as illustrated in Figure 1.18(b). In the ELVS system, a diode laser is used to emit a diverging sheet of light on a plano-cylindrical lens, which collimates the light to a rectangular aperture of fixed width of 25.4 mm. The sheet of light is focused to a point at the other end of ELVS by a convex lens, where the intensity is measured by a high-speed PIN photo-detector. The data acquisition system captures the voltage converted from the light intensity detected by the PIN photo-detector, which is then converted to the elongation for further strain calculation [92,93]. However, the axial and width strains can be measured utilizing digital image correlation (DIC) techniques as well, as described in Section 2.4.

The HISR apparatus has a metal-on-metal contact interface within the engagement piston/sleeve assembly as shown in Figure 1.18(a). As a result, the wave effects created by the contacting surface can cause ringing in the force-time signal, resulting in mechanical oscillation in the measured data. In order to reduce the oscillations caused by the ringing, a rubber o-ring is placed at the piston and sleeve interface to act as a damper. It is worth noting that the rise time to reach the constant strain rate is delayed due to the addition of this damper; however, the rise time associated with the damper in the system is found to be acceptable as it is confined to within low strain levels (approximately 2%) [92,93].

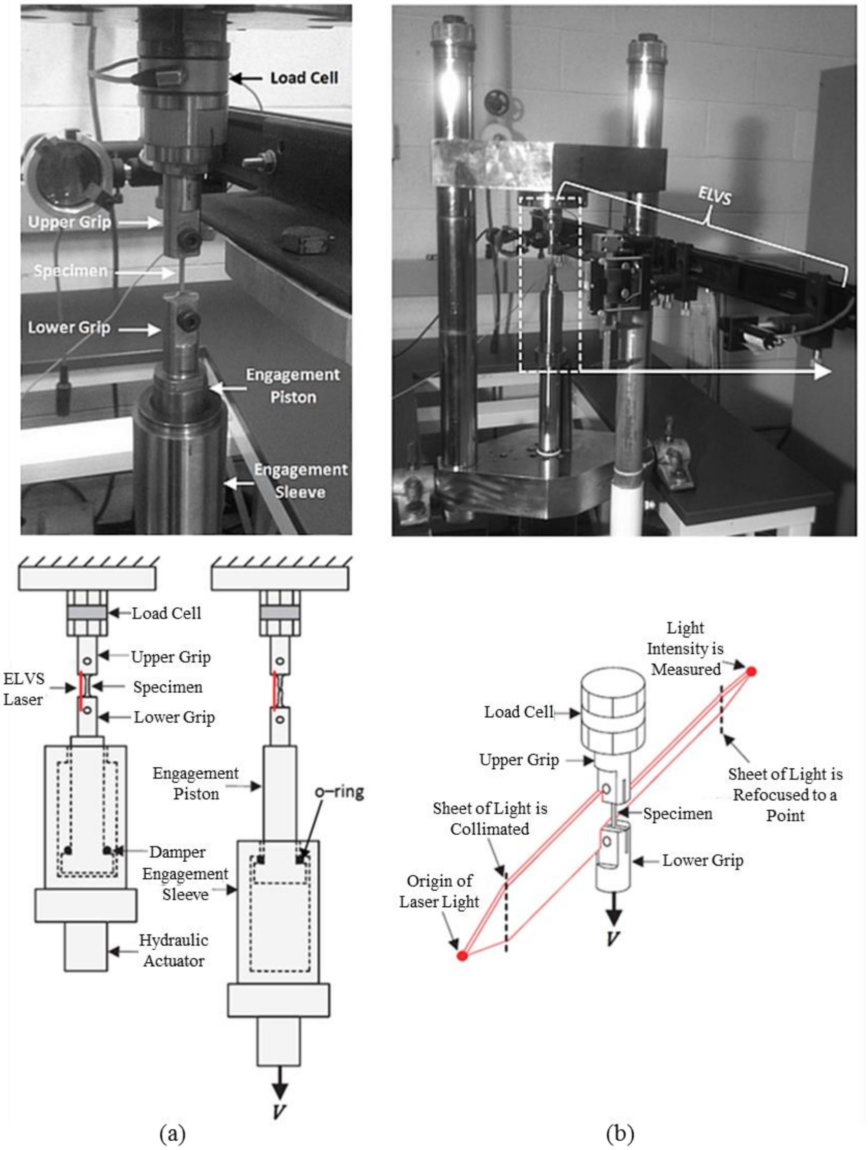

(a) (b)

Figure 1.18: (a) Hydraulic Intermediate Strain Rate (HISR) apparatus at the University of Waterloo with (b) enhanced laser velocity system (ELVS) system [92].

1.6.2 High Strain Rate Testing

The split–Hopkinson bar technique is one of the most widely established and utilized methods to obtain mechanical properties at high strain rates ranging between 10^2-10^4 s^{-1} [16,85,95]. In 1914, Bertrand Hopkinson [85] first described the method to measure the detonation energy of explosives by using a long elastic steel bar suspended as a ballistic pendulum. The pressure was applied at one end of the steel bar by the impact of a bullet or by the detonation of an explosive, while a cylindrical pellet (known as the *time piece*) was attached to the other end of the bar. The material and diameter used for the pellet was same as the steel bar. A compression pulse generated by the applied pressure would transmit through the bar into the pellet, causing the pellet to fly off. The section of the pulse that had a length twice that of the pellet characterized the momentum trapped in the pellet. The nature of the pressure-time relationship for the pulse could be investigated by repeating the procedure using pellets of different length and measuring the momentum in each pellet by capturing it in a ballistic pendulum [85,96].

In 1949, Kolsky [85] utilized the concept of the Hopkinson pressure bar to develop an apparatus that could be used to measure the dynamic response of materials. The apparatus is referred to as a split–Hopkinson pressure bar (SHB) or Kolsky bar. Two cylindrical steel bars were used to deform a specimen by placing it in between the flat faces of two bars. A detonator was used to apply transient pressure at the end of one of the bars, while the displacement-time relationship of each bar was measured using a parallel-plate condenser microphone as the stress wave propagated through the bars and the specimen. The pressure end of the bars was protected by placing a hardened anvil between the bar and the detonator. The amplitude of the pressure pulse arriving at the specimen could be measured using the cylindrical condenser microphones, and the deformation of the specimen then could be deduced [85]. As long as the bars remained elastic, Kolsky [85] was able to determine the stress-strain response of the specimen from the measured data.

The configuration for the split–Hopkinson bar apparatus similar to that used by Kolsky [85] is the most commonly used in practice (shown in in Figure 1.19). It consists of a striker bar, an incident bar, and a transmitter bar. The test specimen is sandwiched or attached in between the incident and transmitter bars. The striker bar impacts at the free end of the incident bar. Typically, a gas gun is used to propel the striker bar. As a result of the impact, an elastic compression wave (commonly referred to as the incident wave) is generated in the incident bar which is twice the length of the striker bar [95]. The amplitude of the wave is proportional to the striker velocity. The incident wave travels down to the specimen end of the bar, and is divided into two parts at the bar-specimen interface. One part of the wave is transmitted through the specimen into the transmitter bar (referred to as the transmitted wave), and the remainder is reflected back along the incident bar as a tensile wave (referred to as the reflected wave). The specimen deforms plastically as soon as the amplitude of the loading pulse exceeds the yield strength of the specimen material. Both the incident and transmitter bar are assumed to be elastically deformable structures, where the waves generated in the bars remain within the elastic region of the bar material preventing any plastic deformations. Strain gauges attached on the bars are used to measure the waves. Figure 1.20 shows an example of the three waves produced in a SHB as they travelled along the respective bars.

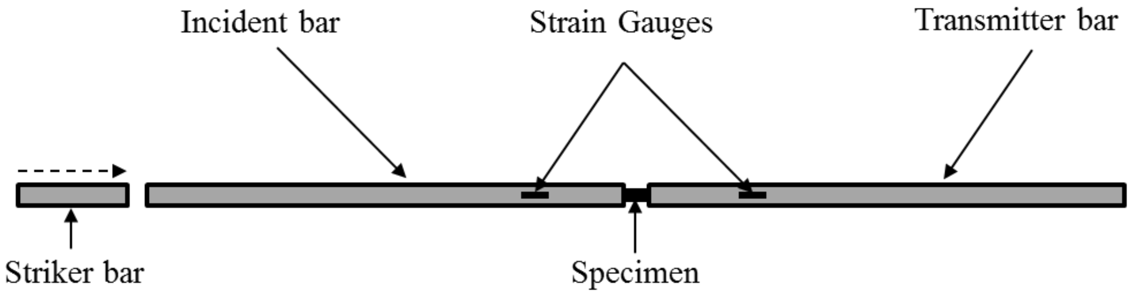

Figure 1.19: Schematic of a compressive split–Hopkinson bar Apparatus.

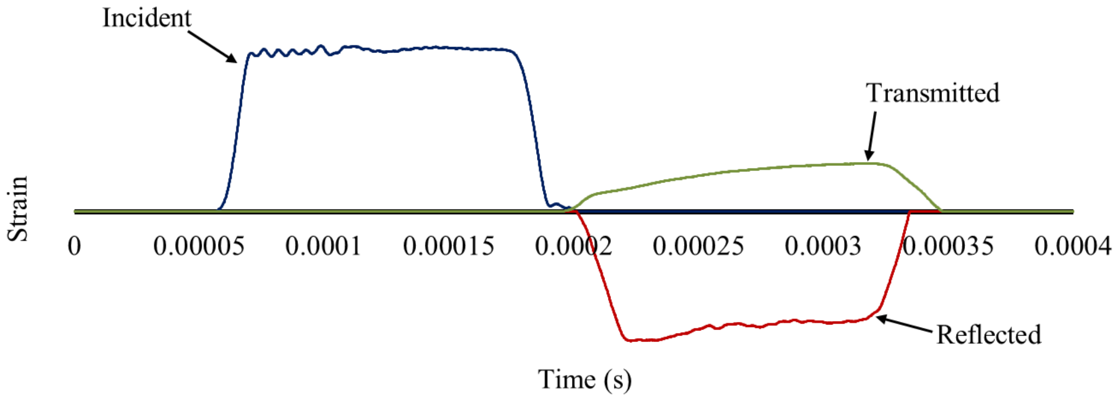

Figure 1.20: Waves generated in a compressive split–Hopkinson bar experiment.

Assuming one-dimensional longitudinal wave propagation along the bars, Kolsky [85] derived the equations to determine stress, strain, and strain rate from the reflected and transmitted waves. In case of a uniform deformation of the specimen during the experiment, the strain can be defined as [95]:

$$\varepsilon\,(t) = \frac{u_i(t) - u_t(t)}{L} \qquad \text{Eq. (1.8)}$$

where, L is the gauge length of the specimen, and $u_i(t)$ and $u_t(t)$ correspond to the instantaneous displacements of the incident and transmitter bar ends, respectively. The displacements of bar ends are determined using the Eq. (1.9) and Eq. (1.10) [97], where $\varepsilon_i(t), \varepsilon_r(t)$, and $\varepsilon_t(t)$ are the strain in the incident, reflected, and transmitter bars, respectively.

$$u_i(t) = \int_0^t C_i[\varepsilon_i(t) - \varepsilon_r(t)]dt \qquad \text{Eq. (1.9)}$$

$$u_t(t) = \int_0^t C_t\varepsilon_t(t)dt \qquad \text{Eq. (1.10)}$$

$$C = \sqrt{\frac{E}{\rho}} \qquad \text{Eq. (1.11)}$$

C_i and C_t represents the elastic sound speed for incident and transmitter bars which are determined as expressed in Eq. (1.11). E and ρ are the elastic modulus and density for the corresponding bars. The strain can be determined by substituting Eq. (1.9) and Eq. (1.10) into Eq. (1.8), as shown in Eq. (1.12). Therefore, the strain rate is shown to be as determined in Eq. (1.13) [95].

$$\varepsilon(t) = \frac{C_i}{L}\int_0^t [\varepsilon_i(t) - \varepsilon_r(t)]dt - \frac{C_t}{L}\int_0^t \varepsilon_t(t)dt \qquad \text{Eq. (1.12)}$$

$$\dot{\varepsilon}(t) = \frac{C_i}{L}[\varepsilon_i(t) - \varepsilon_r(t)] - \frac{C_t}{L}\varepsilon_t(t) \qquad \text{Eq. (1.13)}$$

The split–Hopkinson bar analysis assumes force equilibrium in the specimen [95]. Considering the same material and cross-sectional area for both incident and transmitter bars, the forces at the incident bar end ($F_i(t)$) and the transmitter bar end ($F_t(t)$) can be defined as shown in Eq. (1.14) and Eq. (1.15). A_b and E are the cross-sectional area and the elastic modulus of the bars, respectively.

$$F_i(t) = A_b E[\varepsilon_i(t) + \varepsilon_r(t)] \qquad \text{Eq. (1.14)}$$

$$F_t(t) = A_b E \varepsilon_t(t) \qquad \text{Eq. (1.15)}$$

In order to determine the engineering stress-time history of the specimen, the average stress in the specimen can be considered equal to the average of the forces at each bar end divided by the initial cross sectional area of the specimen (A_s), as shown in Eq. (1.16) [98].

$$\sigma(t) = \frac{F_i(t) + F_t(t)}{2A_0} = \frac{A_b E(\varepsilon_i + \varepsilon_r + \varepsilon_t)}{2A_s} \qquad \text{Eq. (1.16)}$$

At equilibrium, the forces at both ends of the bars are equal, and equating the two forces shown in Eq. (1.14) and Eq. (1.15) yields the following result:

$$\varepsilon_i(t) = \varepsilon_t(t) - \varepsilon_r(t) \qquad \text{Eq. (1.17)}$$

Assuming same elastic sound speed (C) for both incident and transmitter bars and substituting Eq. (1.17) into Eq. (1.12), Eq. (1.13), and Eq. (1.16), the strain, strain rate, and stress can be expressed as shown in Eq. (1.18), Eq. (1.19), and Eq. (1.20), respectively [85].

$$\varepsilon(t) = -2\frac{C}{L}\int_0^t \varepsilon_r(t)dt \qquad \text{Eq. (1.18)}$$

$$\dot{\varepsilon}(t) = -2\frac{C}{L}\varepsilon_r(t) \qquad \text{Eq. (1.19)}$$

$$\sigma(t) = E\frac{A_b}{A_s}\varepsilon_t(t) \qquad \text{Eq. (1.20)}$$

Eq. (1.18)-Eq. (1.20) are considered to be the final forms of Hopkinson bar equations [85]. These equations only take into account the reflected wave for strain and strain rate calculations, and only the transmitted wave for calculating the stress. Therefore, they are also referred to as a single-wave analysis [85]. Although the data analysis for the split–Hopkinson bar experiments is conventionally performed with the single-wave equations, they are only valid for the dynamic equilibrium condition. Therefore, in cases where the dynamic equilibrium assumption is not valid, all three waves are required to be considered in the analysis [22,85,95,97,98].

Various configurations of the split–Hopkinson bar apparatus are used in practice for material testing at different loading states, including compression, tension, torsion, and some complex loading tests such as three-point bending [16,99]. The compressive split–Hopkinson bar (CSHB) apparatus is widely used due to the simplicity of the setup, while tensile split–Hopkinson bar (TSHB) apparatus has gained popularity in performing tensile testing due to simple specimen geometry requirements. Similar principles and components are used for both types of SHB apparatus with the exception of the type of loading applied to the specimen and the methods to generate the loading in incident bar.

Lindholm et al. [97] performed tensile testing using a CSHB apparatus with a hat-shaped specimen. The specimen was fit between a solid cylindrical incident bar and a tubular transmitter bar, as shown in Figure 1.21. A compression pulse generated in the incident bar loads the cylindrical section of the specimen in tension and deforms plastically. The failure in the hat specimen normally occurred near the midsection with occasional failure at the fillet [97]. This configuration has the advantage of to maintaining a planar loading surface and avoiding possible wave dispersion due to direct contact condition between the pressure bars and specimen. However, precise machining of the specimen is required in order to ensure a proper contact condition between the specimen and bar surfaces. Additionally, difficulties involving strain measurements and fabricating hat-shaped specimens with sheet materials has limited the adoption of this test setup.

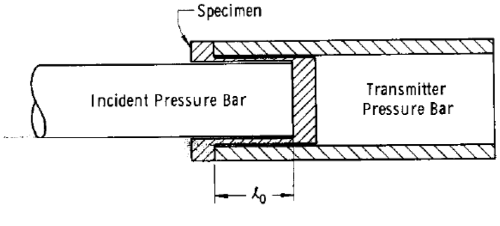

Figure 1.21: Tension specimen configuration used by Lindholm et al. [97]

An experimental method using the split–Hopkinson bar apparatus has been developed by Nicholas [100] for performing high strain rate tensile testing. As shown in Figure 1.22, a cylindrical specimen is screwed into the ends of the bars where a split shoulder or collar is also placed over the specimen. The specimen is screwed in until the pressure bars are snug against the shoulder such that the shoulder remains in contact with both of the pressure bars, while the specimen remains unloaded. In order to avoid wave reflections, the same material is used to fabricate the shoulder and the pressure bars [100]. In this configuration, a compression wave is generated in the incident bar which travels down towards transmitter bar. Ideally, the wave is transmitted through the collar without any wave reflection or causing any plastic deformation in the specimen. Upon reaching the free end of transmitter bar, the wave returns as tensile wave and loads the specimen in tension. Since the shoulder is not fastened in any manner to the bars, it is unable to support any tensile loads. As a result, partial wave is transmitted through the specimen causing plastic deformation, and rest is reflected back into the transmitter bar [100]. Similar to the method used by Lindholm et al. [97], this configuration is easily adapted for testing sheet materials. Additionally, poor assembly fit condition of the specimen and collar to the bars, failure to remove all play out of the threaded joint, and slight inaccuracy in specimen or collar machining will result in uneven loading of the specimen and wave distortion [100].

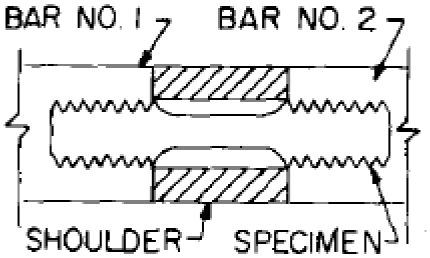

Figure 1.22: Schematic of tensile experiment setup [100].

Due to the limitations of the specimen geometry and experimental setup involved in the testing methods utilizing CSHB apparatus, the TSHB apparatus is used most often for high strain rate tensile testing. As shown in Figure 1.23, a typical configuration of the TSHB apparatus consists a hollow striker bar, incident bar, transmitter bar, and end cap. The hollow striker bar is propelled by a gas gun and travels over the incident bar till it impacts an end cap threaded onto the free end of the incident bar. A direct tensile wave is generated in the incident bar due to this impact and travels through the incident bar towards the transmitter bar. As the tensile wave reaches the specimen, which is attached to both bars, a part of the wave is reflected back to the incident bar and the rest is transmitted through the specimen to the transmitter bar causing the specimen to load in tension. This method has gained popularity since it allows a simple specimen geometry.

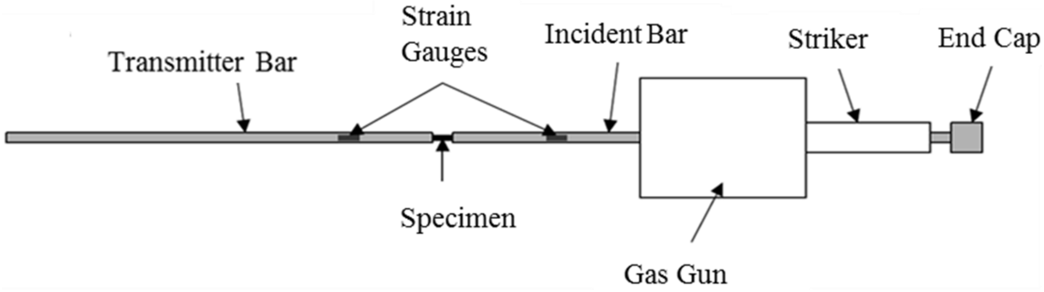

Figure 1.23: Schematic of a typical tensile split–Hopkinson bar apparatus.

Most commonly, dog-bone shaped specimen geometries, similar to ASTM-specified samples [95] (shown in Figure 1.24) with some dimensional variations, are adopted for high rate tensile experiments. The effect of specimen geometry was thoroughly studied by Staab and Gilat [101], who found that the classical Hopkinson bar equations (Eq. (1.18)-Eq. (1.20)) are valid so long as the gauge length-to-diameter ratio of the specimen is greater than 1.6. Smerd et al. [5] also studied specimen geometry effects for split-Hopkinson bar apparatus, and concluded that a short gauge length is desired in order to reduce the specimen ring-up time. They determined a proper specimen geometry for high strain rate tensile testing using split– Hopkinson bar apparatus, with a gauge length of 12.5 mm and a width of 1.75 mm, as shown in Figure 1.25 [5]. Further studies on this miniature tensile specimen performed by Thompson [6] and Bardelcik et al. [92,102,103] have demonstrated that the resultant engineering stress versus strain curves from the ASTM (E 8M-04) and miniature specimens are in agreement until the ultimate tensile strength (UTS) is reached which coincides with the onset of localized necking.

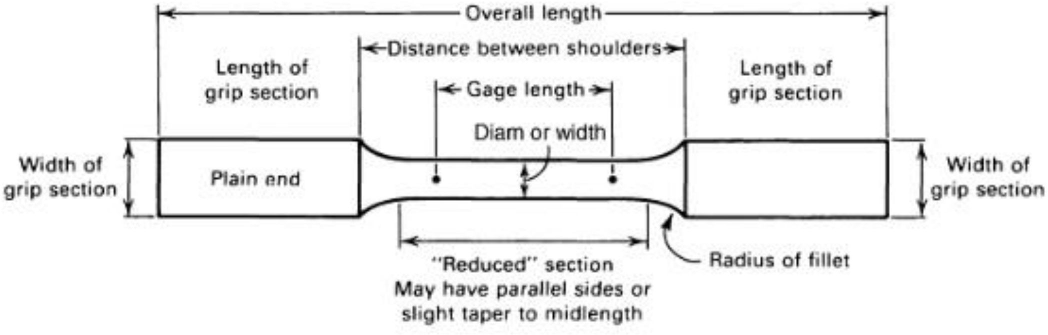

Figure 1.24: Nomenclature for a typical tension test piece [95].

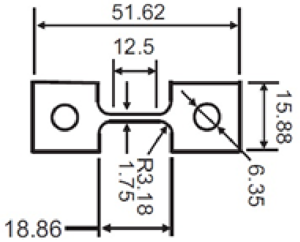

Figure 1.25: Tensile specimen geometry developed by Smerd et al.[5]. All dimensions are in mm.

The specimen is usually fixed into the bars either by threading, mechanical clamping, or adhesive bonding. The use of the threaded components for attaching the specimen into the bars increases the likelihood of wave distortion [19], while mechanical clamping can result in distortion of the elastic stress waves due to the sliding of the specimen and/or inertial effects associated with the mass of the clamp [104]. Adhesive has been successfully used by many researchers [104-107] to attach the specimen into the pressure bars, which provided adequate bond strength to prevent the specimen from sliding in the grip region during the experiments, as well as good quality strain measurements from the experiments.

In SHB testing, the pressure bar is excited by a pulse that is composed of a spectrum of frequencies (similar to a trapezoid-shaped pulse) rather than by a pure sinusoid pulse, where the velocity of each frequency component can be determined independently [108]. For a given material, Davies [109] showed a relationship between a dimensionless ratio r/λ and the ratio of the propagation velocity (c) to the elastic sound velocity (c_0), where r is the radius of the bar and λ is the wavelength of the pulse component. For a bar material with a Poisson's ratio of 0.29, c is equals to c_0 for small values (<<1) of r/λ. As r/λ increases, c/c_0 decreases rapidly at first and then much more slowly. For a large value (≈1) of r/λ, c asymptotically approaches to $0.5764c_0$, the velocity of Rayleigh surface wave [109]. Therefore, the higher frequency components of the pulse travel slowly and lag behind the lower frequency components [108]. As a result, a variation in phase velocity occurs leading to the dispersion of an initially sharp wave, which is typically attributed to the oscillations in the measured waves [108], as seen in Figure 1.20. Follansbe and Frantz [108] performed a wave dispersion correction by transforming the waves to the frequency domain from the time domain, then introducing the variation of the phase velocity with wavelength, and finally converting back to the time domain. However, Clarke [110] concluded that the correction for dispersion is not required in most SHB experiments as the wavelengths of the pulse are much greater than the diameter of the bar. Traditionally, pressure bars made of high strength metal, such as 4340 steel or a nickel alloy, are used in the SHB setup [95]. As shown in [22,95,111-113], the stress wave data can be captured successfully using 4340 steel pressure bars without implementing the dispersion correction as long as the bar length is significantly larger than the bar diameter.

The nature of the pulse generated upon the impact between striker and incident bar is highly complex due to the side-by-side propagation of longitudinal waves and many other types of elastic waves such as spherical dilatational waves [108]. The equations developed by Pochhammer [114] and Chree [115] describe the wave propagation in an infinitely long cylindrical bar, and showed the variation in longitudinal stress across the cross-section of the bar. However, at wave propagation distances further than 10 bar diameters from the striker bar, the non-longitudinal waves dissipate to a point where the one-dimensional wave assumption is valid and the vibrational behavior of an elastic bar excited by a longitudinal pulse is fully described by the equations of motion [98,109].

Eq. (1.18)-Eq. (1.20) assumes dynamic equilibrium stress state in the specimen. The time required for a sample to achieve a uniform state of stress is referred to as ring-up time [95]. For plastically deforming solids, Davies and Hunter [116] have derived the value for the ring-up time, T, as shown in Eq. (1.21):

$$T = \sqrt{\frac{\pi^2 \rho_s h^2}{\frac{d\sigma}{d\varepsilon}}} \qquad \text{Eq. (1.21)}$$

where, ρ_s is the density of the specimen, h is the length of the specimen, and $d\sigma/d\varepsilon$ is the slope of the true stress-strain response of the material. Davies and Hunter [116] showed that the pressure wave has to be reflected inside the specimen π (pi) times before a uniform stress state is reached. Deformation occurring in the specimen prior to the ring-up time cannot be considered to be uniform, and the stress-strain curves acquired from a SHB experiment for times less than ring-up time are not considered valid [95,98]. Thus, obtaining the elastic (low strain) behavior of a material from SHB experiments is difficult. The reduction in ring-up time for a specimen can be achieved in several ways [95,98,117]: (1) reducing the specimen length accompanied by a reduction in cross-sectional area, (2) reducing the pressure bar diameter, (3) increasing the rise time of the incident wave through using pulse shapers such as a soft metal shim between the striker and incident bar.

1.7 STRAIN RATE-SENSITIVE MATERIAL MODELS

The description of the constitutive behavior of the material being modelled is an important aspect of finite element analysis (FEA) simulations. For a specific material, constitutive models are utilized by the FEA software to predict the material flow stress as a function of strain, strain rate, temperature and other state variables. Therefore, the accuracy of the FEA analysis result is directly related to the constitutive response utilized in the simulation. For this project, three different rate-sensitive constitutive models were considered to fit the experimental data so that the best fit can be used in numerical simulations: the Johnson-Cook model [9], the Zerilli-Armstrong model [10], and the Voce constitutive model [11].

1.7.1 Johnson-Cook Material Model

In 1983, Johnson and Cook [9] presented a constitutive model for flow stress which accounted for the effects of strain hardening, strain rate hardening, and thermal softening. An evaluation of the model and data was made by comparing the computed results with the data from cylinder impact tests for 12 different materials including OFHC copper, Cartridge brass, Nickel 200, Armco iron, Carpenter electrical iron, 1006 steel, 2024-T351 aluminum, 7039 aluminum, 4340 steel, S-7 tool steel, Tungsten alloy, and DU 75Ti (depleted uranium). The model has the following form:

$$\sigma = (A + B\varepsilon^n)(1 + C\ln(\dot{\varepsilon}^*))(1 - T^{*m}) \qquad \text{Eq. (1.22)}$$

where, σ is the true stress, ε is the equivalent plastic strain, $\dot{\varepsilon^*} = \dot{\varepsilon}/\dot{\varepsilon_o}$ is a dimensionless plastic strain rate, with reference strain rate $\dot{\varepsilon_o}$, and $T*$ is a form of homologous temperature (Eq. (1.23)). A, B, n, C, and m are material constants fit to data collected for a particular material where A is the yield stress of the material, B and n represent the effects of strain hardening, C describes the strain rate sensitivity, and m describes the thermal softening [9].

$$T^* = \frac{T - T_{ROOM}}{T_{MELT} - T_{ROOM}} \qquad \text{Eq. (1.23)}$$

where, T, T_{ROOM}, and T_{MELT} are the temperature condition of the experiment, room temperature, and melting temperature of the material, respectively. Eq. (1.24) is also used by many researchers to define the homologous temperature in order to consider the effect of test temperatures below room temperature [118].

$$T^* = \frac{T}{T_{MELT}} \qquad \text{Eq. (1.24)}$$

The expression within the first set of parentheses in Eq. (1.22) gives the stress as a function of strain for $\dot{\varepsilon}_0$=1.0 s^{-1} and T^*=0. The expression in the second set of bracket represents the effects of strain rate, while the final term within the third bracket imparts an exponential thermal softening response.

Gray et al. [118] fitted Johnson-Cook model to data for several materials at various test conditions. Fits for Al-7039 are shown in Figure 1.26. They reported that the model fails to describe the material behavior for the full range of temperatures and strain rates due to the simplified power law treatment of the hardening response and the multiplicative coupling of the rate hardening and thermal softening response in Eq. (1.22) (in contrast to the coupled treatment seen, for example, in Eq. (1.4)).

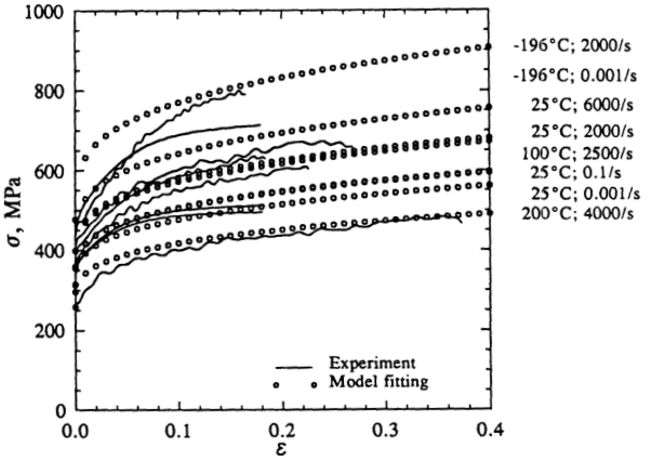

Figure 1.26: Fit of Al-7039 data from various test conditions using Johnson-Cook equations referencing room temperature. The parameters used to fit the data are A=475 MPa, B=550 MPa, n=0.275, C=0.0125, m=1.0, and T_{MELT}=933 K [118].

It is also important to consider that the Johnson-Cook [9] constitutive model does not capture the behavior of complex materials, such as Al-5083, OFHC copper where effect of strain rate and temperature on the flow stress is dependent on the strain [118]. Furthermore, the strain rate and temperature sensitivity terms are assumed to be independent of each other in this model, whereas the effect of strain rate and temperature is typically found to be coupled in real materials [119].

1.7.2 Zerilli-Armstrong Material Model

Zerilli and Armstrong [10] proposed a dislocation mechanics-based constitutive relation in an attempt to better describe material rate sensitivity. The effects of strain hardening, strain rate hardening, and thermal softening have been incorporated into a constitutive relation based on the thermal activation analysis. Compared to other dislocation based constitutive models, this relation has a relatively simple expression to define the material behavior [120]. Zerilli-Armstrong [10] proposed different equations to predict the constitutive behavior for each material structure type such as, face-centre-cubic (FCC) and body-centre-cubic (BCC). Different rate-controlling mechanisms define the constitutive behavior for each particular structure type. Eq. (1.25) shows the general form of the Zerilli-Armstrong [10] model:

$$\sigma = \Delta\sigma_G + \sigma_{THERMAL} + kl^{-1/2} \qquad \text{Eq. (1.25)}$$

where, σ is the von Mises equivalent stress, $\Delta\sigma_G$ represents the athermal components of stress that considers the influence of solutes (alloying elements) and the initial dislocation density of inclusions, $\sigma_{THERMAL}$ includes the strain rate and temperature effects on the flow stress, and the final term, $kl^{-1/2}$ is the influence of grain size.

For BCC materials, the contribution of strain, strain rate, and temperature on the thermal component of stress, $\sigma_{THERMAL}$ is expressed in Eq. (1.26), where $\dot{\varepsilon}$ is the plastic strain rate, T is the absolute temperature, and C_1, C_3, and C_4 are material constants.

$$\sigma_{THERMAL} = C_1 \exp(-C_3 T + C_4 \cdot T \cdot ln\dot{\varepsilon}) \qquad \text{Eq. (1.26)}$$

In order to account for strain rate-independent plastic hardening for BCC metals, a separate power-law term (as shown in Eq. (1.27) is added to Eq. (1.25).

$$\Delta\sigma = C_5 \varepsilon^n \qquad \text{Eq. (1.27)}$$

where, ε is the equivalent plastic strain and parameters C_5 and n are material parameters. So, the final form of Zerilli-Armstrong [10] constitutive equation for BCC metals is:

$$\sigma = \Delta\sigma_G + C_1 \exp(-C_3 T + C_4 \cdot T \cdot ln\dot{\varepsilon}) + C_5 \varepsilon^n + kl^{-1/2} \qquad \text{Eq. (1.28)}$$

For FCC metals, the Zerilli-Armstrong [10] model coupled the contribution of strain, strain rate, and temperature within one single term to express the thermal stress component, σ_{THERMAL}, given as:

$$\sigma_{THERMAL} = C_2 \varepsilon^{1/2} \exp(-C_3 T + C_4 T ln\dot{\varepsilon}) \qquad \text{Eq. (1.29)}$$

where ε is the equivalent plastic strain, $\dot{\varepsilon}$ is the strain rate, T is the absolute temperature, and C_2, C_3, and C_4 are the material constants. Thus, the final form of Zerilli-Armstrong [10] for FCC metals is shown in Eq. (1.30). Unlike Zerilli-Armstrong [10] constitutive model for BCC metals, the strain rate and temperature effect on flow stress are dependent on the strain hardening in the Zerilli-Armstrong [10] constitutive model for FCC metals.

$$\sigma = \Delta\sigma_G + C_2 \varepsilon^{1/2} \exp(-C_3 T + C_4 \cdot T \cdot ln\dot{\varepsilon}) + kl^{-1/2} \qquad \text{Eq. (1.30)}$$

This form results in a material response in which the yield strength is relative rate-independent whereas the hardening rate is strongly rate- and temperature-dependent.

Both Zerilli-Armstrong constitutive models were evaluated by simulating Taylor impact and tensile tests performed on OFHC and Armco iron [10]. Although the data fitting for Zerilli-Armstrong [10] constitutive model has more accuracy than Johnson-Cook [9] constitutive model, some limitations were observed in predicting the constitutive behavior of materials that exhibit very strong sensitivity to strain rate or other complex material behavior such as dynamic strain aging [118,120]. Furthermore, continuously the increasing hardening rate characteristics of the Zerilli-Armstrong models has the potential to predict unrealistic stress levels at larger strains; particularly for materials that exhibit stress-saturation type behavior.

1.7.3 Voce Material Model

In 1948, Voce [11] proposed a saturation-type constitutive model to predict the hardening behavior of the materials, given as:

$$\sigma_V(\varepsilon_p) = \left[\sigma_{sat} + (\sigma_y - \sigma_{sat})e^{\left(-\frac{\varepsilon_p}{\varepsilon_r}\right)}\right] \qquad \text{Eq. (1.31)}$$

where, σ_{sat} is the saturation stress, i.e. the stress level at which the strain-hardening rate lowers to zero, σ_y is the yield stress, ε_p and ε_r are the effective plastic and relaxation strain, respectively. Plastic deformation below and above the relaxation strain is assumed to be caused by planar glide and cross slip mechanisms, respectively [121]. Thus, the rate at which the stress approaches its saturation value is determined by the relaxation strain [122]. Figure 1.27 shows the Voce parameters and the corresponding deformation mechanisms [123].

The Voce constitutive model [11] is not purely empirical in nature; rather it does have physical meaning as discussed by Bissot [124]. The parameters of the Voce constitutive model [11] can directly relate with the stress-strain behavior of a material from a dislocation point of view. A small portion of the strain sites get blocked in the case where some finite number of strain hardening sites and a small increment of strain is applied to the material. The ratio of the blocked sites to the total number of hardening regions is equal to the ratio of the plastic stress capacity used in the material to the total plastic stress capacity of the material (as shown in Eq. (1.32)) [124]. The initial asymptotic portion of stress-strain curve exists because dislocations are free to move with none, or very few being blocked. An increased amount of dislocations become blocked with the increase of plastic deformation until the stress asymptotically approaches saturation stress, σ_{sat}. This is due to the balance between blockage rate and annihilation rate of dislocations [124,125].

$$\frac{n}{N} = \frac{\sigma - \sigma_0}{\sigma_{sat} - \sigma} \qquad \text{Eq. (1.32)}$$

The Voce [11] model alone is neither strain rate- nor temperature-sensitive, therefore the integration of a strain rate and temperature dependent term with the Voce hardening law is typically added to capture the changes in flow stress with respect to strain rate. Kocks [126] expanded the classical Voce law [11] by describing the saturation stress σ_{sat} as function of temperature and strain rate, as shown in Eq. (1.33).

$$\sigma_{sat} = \sigma_{s0}\left(\frac{\dot{\varepsilon}}{\dot{\varepsilon}_{s0}}\right)^{\left(kT/A_s\right)} \qquad \text{Eq. (1.33)}$$

$$\text{where, } A_s = \mu b^3 A \qquad \text{Eq. (1.34)}$$

where k represents the Boltzmann constant, μ represents the temperature dependent shear modulus, b is the Burgers vector, and $\dot{\varepsilon}_{s0}$, A, and σ_{s0} are material constants.

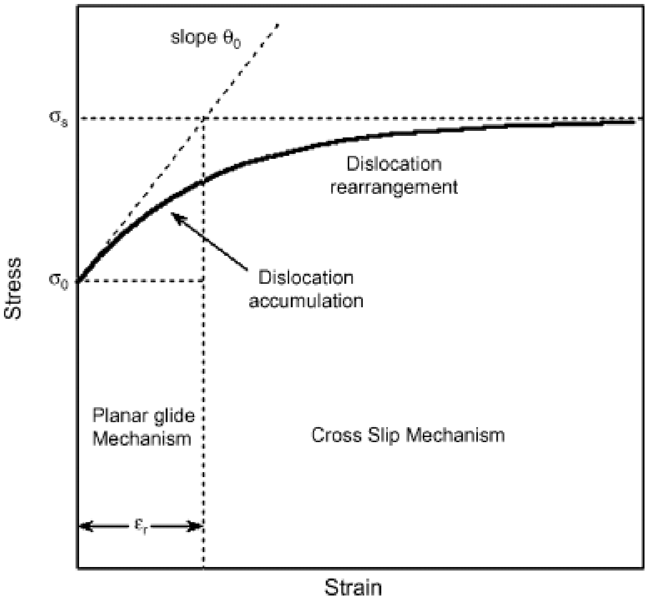

Figure 1.27: Deformation mechanisms corresponding to the Voce parameters [123].

An exponential-type strain rate function was integrated with the Voce hardening law by Bardelcik et al. [92,102,103] in order to capture the strain rate dependent material behavior. Bardelcik et al. [92,102,103] added a multiplicative strain rate sensitive term of the form adopted by Camacho and Ortiz [127] and implemented within a Johnson-Cook model for high strength steel by Børvik et al. [128]. The rate-sensitive form of the Voce law becomes [92]:

$$\sigma_V(\varepsilon_p) = \left[\sigma_{sat} + (\sigma_y - \sigma_{sat})e^{\left(-\frac{\varepsilon_p}{\varepsilon_r}\right)}\right][1 + \dot{\varepsilon}^D] \qquad \text{Eq. (1.35)}$$

where D is the strain rate parameter.

Eq. (1.35) was validated by Bardelcik et al. [92,93,103] for die quenched boron steel for a range of microstructural conditions (hardness) as shown in Figure 1.28. The method implemented by Bardelcik et al. [92,102,103] to integrate the strain rate function with the Voce hardening law is less complicated compared to the method proposed by Kock [126]. Furthermore, constitutive models with fewer parameter are preferable in order to increase the computational cost efficiency. Other strain rate sensitivity functions, such as logarithmic or power-law types, can also be integrated with the Voce model.

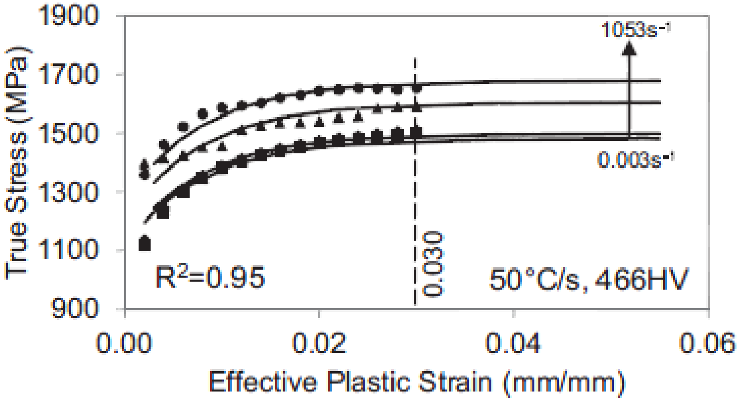

Figure 1.28: Results of the Voce constitutive model (solid lines) fits to the measured flow stress data (data points) for quenched boron steel with tailored properties [92].

1.8 PRESENT RESEARCH

The focus of the current work is to assess the room temperature strain rate sensitivity of three important sheet materials utilized in light weight automotive structures, namely TRIP780, DP600, and AA5182-O. Based upon the review of the pertinent literature presented above, a number of studies have been performed characterizing and modelling the strain rate sensitivity of these metals [4-7]. However, studies capturing the entire strain rate range operative over the metal forming and crashworthiness life cycle experienced by these materials (10^{-3} - 10^{3} s^{-1}) are less common. In addition, there appears to be considerable variation in the anisotropic response of these alloys, in particular TRIP780 (Table 1.1), reported in the literature and very little work has been done on systematic characterization of the effect of strain rate on sheet anisotropy.

Thus, in the current work, experiments at strain rates of 10^{-3}, 10^{-1}, 10^{0}, 10^{1}, 10^{2}, and 10^{3} s^{-1} have been performed on single lots of these three alloys. The effect of strain rate on the anisotropy of these metals was examined by characterizing the flow stresses and r–values along the rolling (0°), diagonal (45°) and transverse (90°) directions of the sheet metal for the entire range of strain rates tested. Beyond their significance as alloys of choice in automotive structural light weighting applications, the three alloys chosen for this work were selected due to their rather different rate sensitivities. DP600 offers relatively conventional positive rate sensitivity, whereas both TRIP780 and AA5182-O display negative rate sensitivity in certain strain rate and temperature regimes. Thus, one goal of this thesis is to contrast these rather different strain rate sensitivities. To this end, high speed digital image correlation (DIC) techniques are applied to characterize the PLC effect as a function of strain rate within the AA5182-O samples. The experimental results were fit to various constitutive models such as, Johnson-Cook, Zerilli-Armstrong, and the Voce hardening law with both logarithmic and exponential strain rate functions. Finally, strain rate-sensitive constitutive models are proposed and fit to the measured data sets.

The balance of this thesis is organized as follows. In Chapter 2, the materials tested and experimental apparatus methods are described. In Chapter 3, the experimental results are presented for all of the sheet metal alloys and testing conditions considered herein. In Chapter 4, the fits of the parameters to various constitutive models are compared to the experimental results and the accuracy of each fit is presented. In Chapter 5, numerical models of the experiments are presented for different strain rate conditions and the performance of the constitutive models is evaluated through comparison of the predicted and measured engineering stress-strain responses and the area reductions. Chapter 6 provides a discussion of the results, along with conclusions from the current work and recommendations for future work.

CHAPTER 2

EXPERIMENTS

2.1 MATERIALS

The materials studied in this research were DP600, TRIP780, and AA5182-O sheet metal alloys. They were selected due to their importance in lightweight automotive applications and their differences in observed rate sensitivity. The chemical compositions of the materials are shown in Table 2.1. The specimens used in the testing were extracted from nominal 1.5 mm thick metal sheets, oriented along the sheet rolling direction (RD), transverse direction (TD) (90° to rolling direction), and diagonal direction (DD) (45° to rolling direction), (as shown in Figure 2.1).

Table 2.1: Chemical compositions of the materials (wt%).

	C	Mn	P	Si	Al	Cu	Ni	Cr	Mo	V	Nb	Ti
DP600	0.11	1.50	0.01	0.18	0.04	0.06	0.02	0.18	0.21	<0.01	<0.01	0.03
TRIP780	0.21	1.74	0.01	0.05	0.49	<.02	<.02	0.20	<.02	<0.01	0.02	<0.01
	Mg	Mn	Cr	Cu	Zn	Si	Ti	Fe				
AA5182	4.50	0.35	0.03	0.05	0.05	0.08	0.10	0.27				

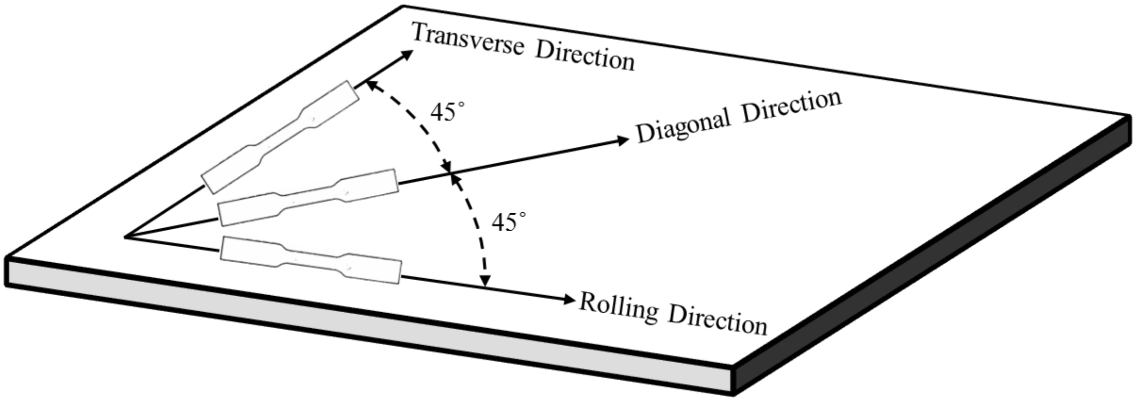

Figure 2.1: Sheet metal orientations used for extracting the specimens.

2.2 SPECIMEN GEOMETRY

Two different dog-bone specimen geometries were used in this work, an ASTM (E 8M-04) specimen and a miniature dog-bone specimen (Figure 2.2). The ASTM specimens were used for testing at 0.001 and 0.1 s^{-1}, while the miniature dog-bone specimens were used for the testing at strain rates of 1 s^{-1} and above. The justification for using the miniature dog-bone style specimens for the high strain rate uniaxial tensile testing is presented by Smerd et al. [5] for aluminum alloys and Bardelcik et al. [92,102,103] for high strength steels. Those studies have demonstrated that the resultant engineering stress versus strain curves from the ASTM (E 8M-04) and miniature specimens are in agreement until the ultimate tensile strength (UTS) is reached which coincides with the onset of localized necking. Since the measured uniaxial stress-strain data used in constitutive fitting is only valid until the UTS, the miniature specimens are a valid alternative to the ASTM specimens for high rate material characterization. The post uniform and total elongation measured from the miniature specimen geometry tests are exaggerated and therefore cannot be used in comparison with test results conducted on standard ASTM specimens. The total elongation measured from the miniature specimens is used, however, to rank the relative ductility of the metals tested in this work.

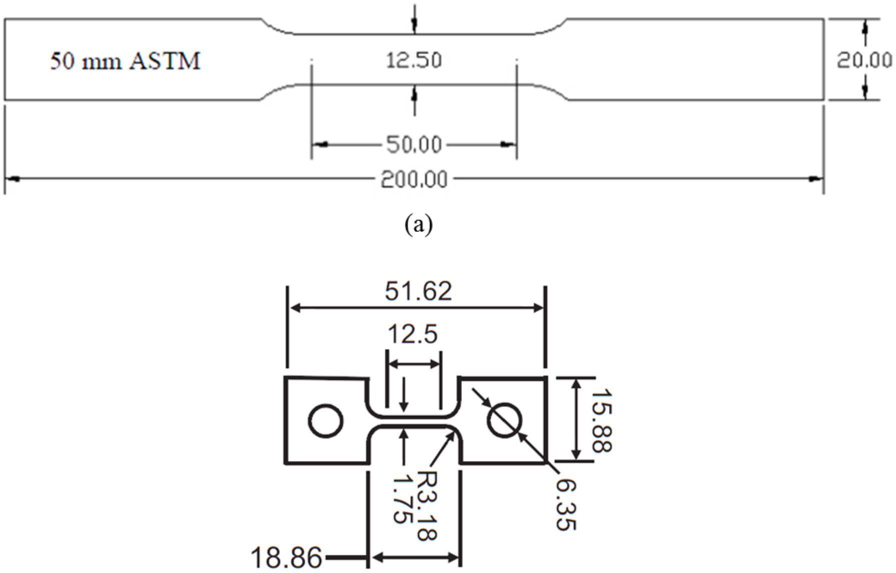

(a)

(b)

Figure 2.2: Specimen geometry of the (a) ASTM (E 8M-04) specimen and the (b) miniature specimen (dimensions are in mm)

2.3 TESTING APPARATUS

2.3.1 Instron Servo – Hydraulic Testing Machine

An Instron model 1331 servo-hydraulic testing machine was used to conduct uniaxial tensile tests at strain rates of 0.001, 0.1, and 1 s^{-1}. As noted above, the miniature dog-bone specimen was used for the Instron experiments at 1 s^{-1}. Cross-head velocities for the experiments were 3 mm/min, 300 mm/min, and 750 mm/min while the data was collected at a sampling rate of 1.67 Hz, 167 Hz, and 5000 Hz, corresponding to the experiments at 0.001, 0.1, and 1 s^{-1}, respectively. The force was measured using a load cell with a capacity of 112 kN and the axial and width strains (for the ASTM samples) were measured using a ±12.5mm biaxial extensometer. A pair of custom grips was used to mount the miniature specimen for testing at 1 s^{-1}, as shown in Figure 2.3 with the extensometer. In order to minimize possible bending loads applied to the specimen, the grips were positioned as to align the specimen concentrically with respect to the loading axis of the machine.

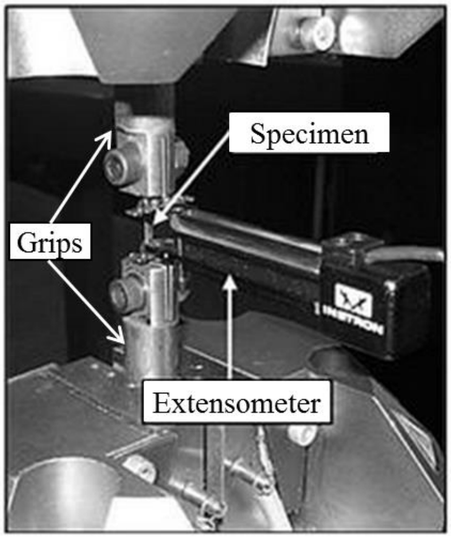

Figure 2.3: Grips and extensometer setup in the Instron testing machine for uniaxial tension test [94].

2.3.2 Hydraulic Intermediate Strain Rate (HISR) Apparatus

A Hydraulic Intermediate Strain Rate (HISR) apparatus developed at the University of Waterloo was used to perform uniaxial tension tests at strain rates of 10 and 100 s^{-1} [92,93]. The HISR apparatus utilizes a slack type engagement assembly which accelerates up to a constant velocity, at which point it contacts a lower grip that pulls the specimen in tension. The apparatus is equipped with a 13.3 kN (3,000 lbf) hydraulic actuator with 101.6 mm (4″) stroke. The maximum stroke rate of 1500 mm/s can be achieved using a MOOG high performance servo-valve with a 15 GPM flow capacity. The load is measured using a KISTLER 9500A4 ±30kN piezoelectric load cell. Cross-head velocities of 325 mm/s and 3,000 mm/s were used to achieve nominal strain rates of 10 and 100 s^{-1}, respectively.

The load and displacement are acquired within the HISR system using a National Instruments 6212 USB data acquisition module coupled with a desktop computer. The existing system has a capability to capture the data with a maximum sampling rate of 250,000 samples per second [92]. In some cases, a DIC system is integrated to the HISR system for overall strain field and elongation measurement. In such cases, the load cell signal can also be simultaneously acquired by the DIC data acquisition system which serves to synchronize the load data with the DIC video images.

The strain distributions within the samples were measured using digital image correlation (DIC) techniques, as described in Section 2.4. This data was used to calculate the axial and width strains over the gauge length needed for stress-strain characterization and r-value determination at high rates. The load cell signal was simultaneously acquired by the DIC data acquisition system and synchronized with the video images.

2.3.3 Tensile Split Hopkinson Bar

A tensile split Hopkinson bar (TSHB) apparatus located at University of Waterloo was used to test the metals at a strain rate of 1000 s^{-1}. A photograph of the TSHB apparatus used in this work is shown in Figure 2.4. A detailed description of the design of this apparatus can be found in [5,6,110]. In the present work, 15.88 mm diameter 4340 steel round bars with a length of 2,159 mm and 1,829 mm were used for the incident and transmitter bars respectively, while a 508 mm long hollow tube was used as a striker. High speed amplifiers and a 20 M sample/s data acquisition system were used to measure the strain gauge data. Loctite 490 instant adhesive was used to fix the specimens within slots cut into the bar ends.

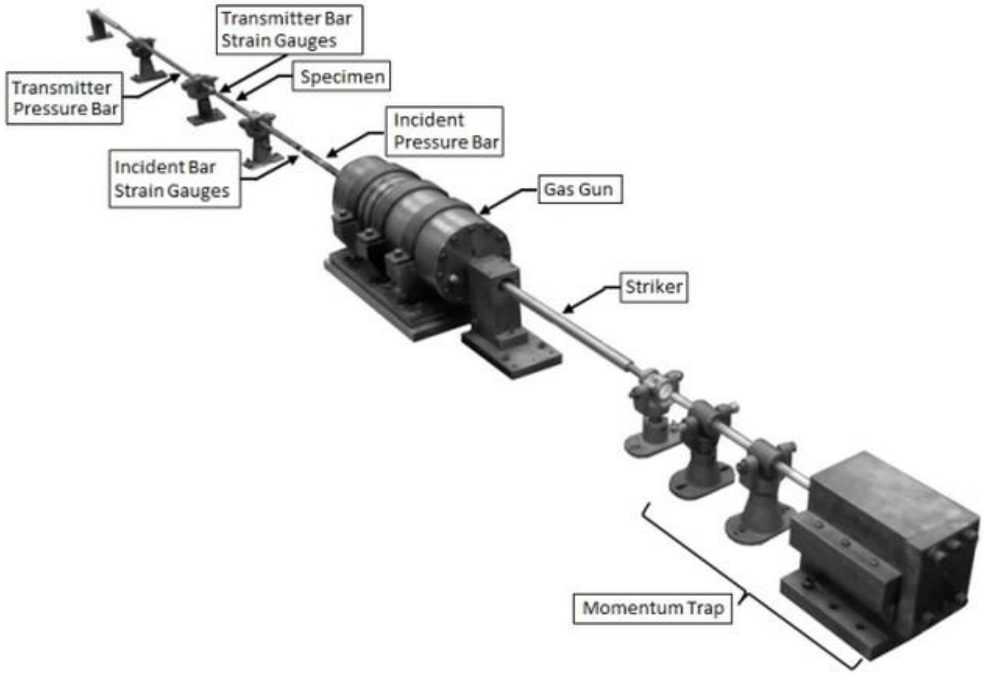

Figure 2.4: Photograph of TSHB apparatus at the University of Waterloo [94].

In a typical TSHB experiment, the specimens are fixed between the incident and transmitter bars, and loaded in tension by a tensile wave produced by the striker bar striking the back of the transmitter bar. A portion of the wave is transmitted through the specimen and into the transmitter bar, with the remainder of the wave being reflected back as a compressive wave into the incident bar. The incident, transmitted, and reflected waves are measured at strain gauge stations mounted on the incident and transmitter bar and the classic Hopkinson bar equations [129] (shown in Eq. (1.18)-Eq. (1.20)) are applied to them to generate the engineering stress-strain curves and strain rate data, where σ is the stress in the specimen, A_b is the cross-sectional area of the bars, A_s is the cross-sectional area of the specimen, and ε_t is the strain in the transmitter bar. ε_r is the reflected strain, ε is the specimen strain, $\dot{\varepsilon}$ is the specimen strain rate, C is the elastic wave speed in the bars, and L is the specimen gauge length. These equations are discussed in detail in Section 1.6.2. Further detailed description of the equipment and methods used for data reduction can be found in [5,130].

$$\varepsilon(t) = -2\frac{C}{L}\int_0^t \varepsilon_r(t)dt \qquad \text{Eq. (1.18)}$$

$$\dot{\varepsilon}(t) = -2\frac{C}{L}\varepsilon_r(t) \qquad \text{Eq. (1.19)}$$

$$\sigma(t) = E\frac{A_b}{A_s}\varepsilon_t(t) \qquad \text{Eq. (1.20)}$$

Foil-type strain gauges were used on both the incident and transmitter bars to capture incident, reflected, and transmitted waves (an example of the waves is shown in Figure 2.5). Two strain gauges were placed on the opposite sides of the bars in a half-bridge configuration in order to cancel any possible bending. The nominal resistance of the gauges used on the incident and transmitter bars were 120 Ω and 1000 Ω, respectively.

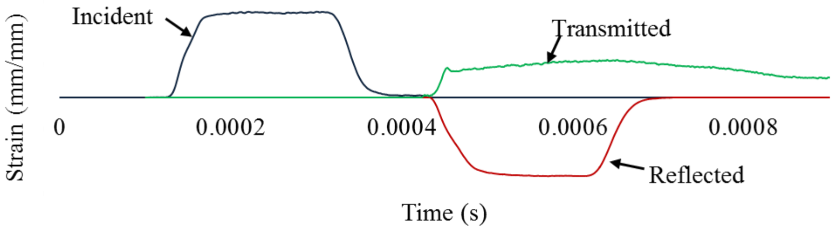

Figure 2.5: Incident, reflected, and transmitted waves of a TSHB experiment on DP600 along rolling direction at 1000 s^{-1} strain rate.

As shown in Figure 2.6, the half Wheatstone bridge was completed using two resistors of the appropriate resistance [19].

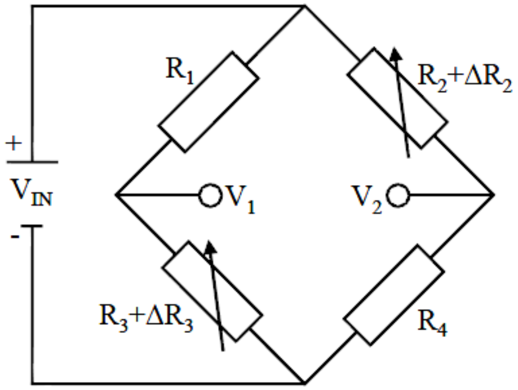

Figure 2.6: Configuration of half Wheatstone bridge [19].

A 10V DC input voltage was used to excite the Wheatstone bridge. The output signal from the Wheatstone bridge is measured across V_1 and V_2. The output signal is amplified by a VISHAY 2210B Signal Conditioning Amplifier with an amplifier gain, G_0 = 300, and frequency response of 120 kHz. Assuming, the same gauge factors for both strain gauges and equal nominal resistances in the configuration, the input and output voltages of the Wheatstone bridge can be expressed by Eq. (2.1) [131].

$$V_{OUT} = V_1 - V_2 = G_0 \left(\frac{\Delta R}{2R + \Delta R}\right) V_{IN} \qquad \text{Eq. (2.1)}$$

$$\text{where, } \Delta R = \varepsilon \cdot G.F \cdot R \qquad \text{Eq. (2.2)}$$

where G_0 is the amplifier gain, R is the nominal resistance of the strain gauges, ΔR is the change in resistance per unit strain of the strain gauges, V_{IN} is the bridge excitation voltage, $G.F.$ is the strain gauge factor, and ε is the applied strain. From Eq. (2.1) and Eq. (2.2), the strain can be expressed as a function of measured voltage, as shown in Eq. (2.3).

$$\varepsilon = \frac{2V_{OUT}}{G.F(G_0 V_{IN} - V_{OUT})} \qquad \text{Eq. (2.3)}$$

2.4 DIGITAL IMAGE CORRELATION (DIC) SYSTEM

A Digital Image Correlation (DIC) system was employed to measure the full-field strain distribution within the samples during the tensile tests ranging from low to high rates of strain, a feature that is not available for the conventional techniques utilizing extensometer [132]. The digital image correlation technique is an optical method, in which the digital image data captured during mechanical testing is examined by mathematical correlation analysis [133].

In the DIC method, the displacement/deformation is measured using a correlation algorithm by tracking the position of multiple surface points (known as speckles) in two successive images [133]. The correlation algorithm tracks the intensity (gray value) patterns within small areas (referred to as subsets) to compute the local in-plane displacements (u, v) at the centre point (x_C, y_C) of the subsets by comparing the two consecutive images [132]. The cross-correlation term for two consecutive images is expressed as in Eq. (2.4) [134].

$$c(u,v) = \sum_i \sum_j I_1(x_i, y_j) I_2(x_i + u_L, y_j + v_L) \qquad \text{Eq. (2.4)}$$

$$\text{where, } u_L = u + \frac{du}{dr}(x_L - x_C) + \frac{du}{ds}(y_L - y_C) \qquad \text{Eq. (2.5)}$$

$$\text{and } v_L = v + \frac{dv}{dr}(x_L - x_C) + \frac{dv}{ds}(y_L - y_C) \qquad \text{Eq. (2.6)}$$

Here, u_L and v_L represent the displacements of an arbitrary point (x_L, y_L) in the subset and I_1 and I_2 represent the intensity of the subset pixel in the reference and deformed images, respectively. A normalized correlation is defined to achieve better performance, as shown in Eq. (2.7) [132]. In order to determine the in-plane displacements, a subset around a point at one position in the reference image is compared with the subset around a point in the deformed image having the same intensity distribution. Further detailed discussion on the principals of DIC analysis can be found in [132,133].

$$C(u,v) = \frac{\sum_i \sum_j I_1(x_i, y_j) I_2(x_i + u_L, y_j + v_L)}{\sqrt{\sum_i \sum_j I_1^2(x_i, y_j) \sum_i \sum_j L_2^2(x_i + u_L, y_j + v_L)}} \qquad \text{Eq. (2.7)}$$

The preparation of the specimen surface and speckle pattern has significant effect on the quality of the image and resulting data. A high quality speckle pattern allows the post-processing software to identify and calculate the displacements accurately. Therefore, it is important to get an adequate speckle pattern, as well as an initially flat and smooth specimen surface. A considerable quantity of black speckles arranged randomly with different shapes and sizes are required to achieve an adequate speckle pattern. Examples of typical speckle patterns are shown in Figure 2.7 [133].

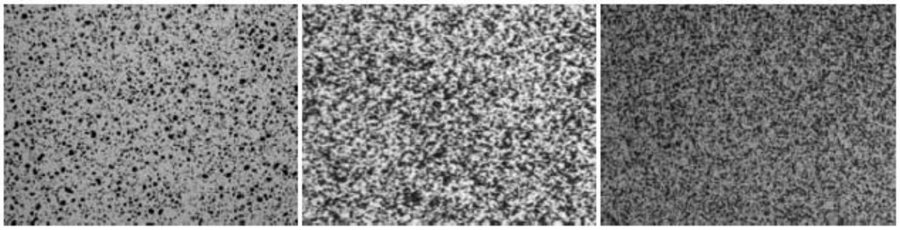

Figure 2.7: Typical speckle patterns [133].

In the present work, for the 1, 10 100 and 1000 s^{-1} tests, two-dimensional Digital Image Correlation (DIC) techniques with high speed video image acquisition were utilized to obtain longitudinal and width strain data using virtual extensometers with respective gauge lengths of X and Y. A random speckle pattern was applied by first painting the specimens white and then applying a random black speckle pattern (shown in Figure 2.8a). A Photron SA5 high speed camera was used to capture the images. In the present work, the frame rates used were (values in parenthesis indicate image size): 1,500 fps (640 x 848 pixels), 10,000 fps (320 x 872 pixels), 35,000 fps (192 x 880 pixels), and 175, 000 fps (320 x 104 pixels) for strain rates of 1, 10, 100, and 1000 s^{-1}, respectively. Figure 2.8b shows the DIC setup for an intermediate strain rate tensile test on the HISR apparatus.

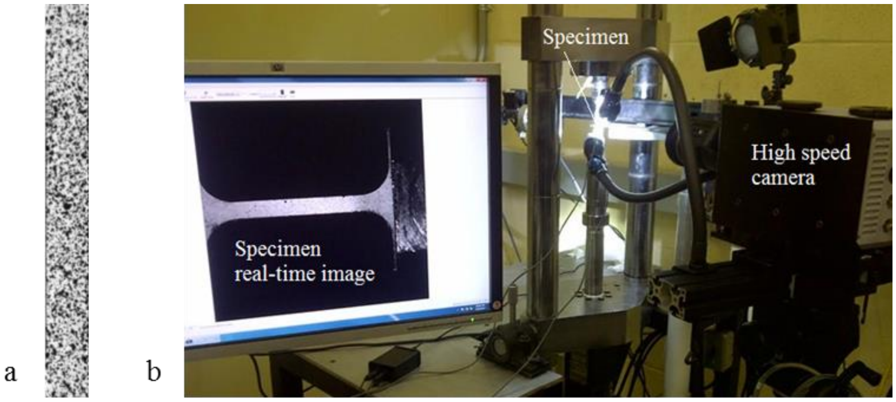

Figure 2.8: (a) Speckle pattern on specimen, (b) DIC testing setup on the HISR.

Data processing of the recorded images was conducted using the Correlated Solutions Vic2D software. Two-dimensional digital image correlation measures full-field surface displacement with accuracy on the order of ±0.1 pixels on nominally planar specimens undergoing arbitrary in-plane rotations and/or deformations [133].

2.5 ANALYSIS OF EXPERIMENTAL DATA

2.5.1 True Stress–Effective Plastic Strain

All of the raw load-displacement data was converted into engineering and true stress-strain data. The true stress (prior to necking) was calculated using Eq. (2.8), where σ_T is the true stress, σ_{ENG} is the engineering stress, and ε_{ENG} is the engineering strain.

$$\sigma_T = \sigma_{ENG}(1 + \varepsilon_{ENG}) \qquad \text{Eq. (2.8)}$$

The true strain was further reduced to effective plastic strain, $\varepsilon_{effective}$ by taking into account the apparent Young's modulus, as shown in Eq. (2.9).

$$\varepsilon_{effective} = \ln(1 + \varepsilon_{ENG}) - \frac{\sigma_T}{E} \qquad \text{Eq. (2.9)}$$

where, ε_{ENG} is engineering strain and E represents the apparent Young's modulus.

For each individual test, the average true plastic strain rate was calculated from the true strain from yield to the end of the test. True strain rate versus true strain data from representative individual experiments, conducted at each nominal strain rate, are shown in Figure 2.9. A relatively constant nominal strain rate was observed throughout the loading duration for each test condition, as indicated in Figure 2.9. Therefore, all of the flow stress data from the onset of yielding until the UTS was used for constitutive fitting.

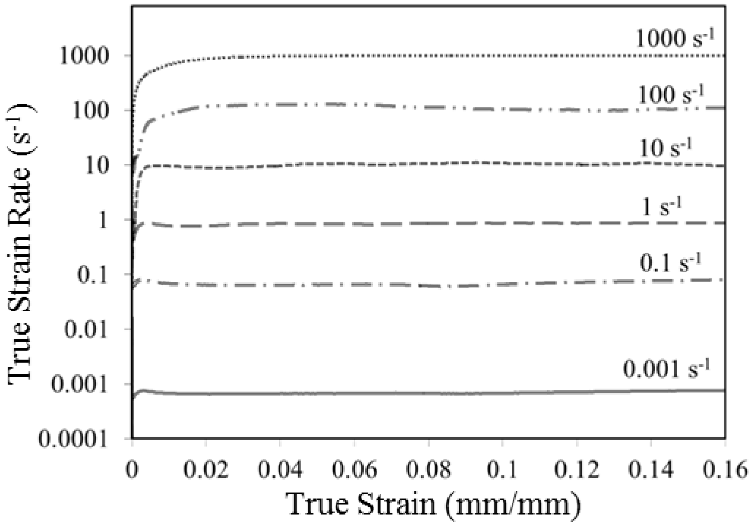

Figure 2.9: True strain rate versus true strain curves.

2.5.2 r–values

The r–value (Lankford coefficient) extracted from a tensile test oriented at an angle, θ, relative to the sheet rolling direction is defined in Eq. (2.10). The biaxial extensometer (0.001 and 0.1 s^{-1}) and DIC (1 to 1,000 s^{-1}) strain data provided the true elongation ($\varepsilon_{elongation}$) and width (ε_{width}) strain, which was then used to calculate the plastic components of the true thickness ($\varepsilon_{thickness}$) strain using the principle of volume conservation (Eq. (2.11)).

$$r_\theta = \frac{\varepsilon_{width}}{\varepsilon_{thickness}} \qquad \text{Eq. (2.10)}$$

$$\varepsilon_{elongation} + \varepsilon_{width} + \varepsilon_{thickness} = 0 \qquad \text{Eq. (2.11)}$$

2.5.3 Adiabatic Heat Rise

The temperature is assumed to be constant (isothermal assumption) in case of the low rate experiments due to the slow nature of the experiments. Thus, all of the heat generated within the specimen during the low rate experiments was assumed to be dissipated either through conduction to the grip regions or through convection to air.

Since, there is very little time for the heat to leave the specimens during the intermediate and high strain rate experiments, the heat generated in the specimens are only partially dissipated [6]. The maximum temperature rise, ΔT due to adiabatic heating from plastic work was calculated using Eq. (2.12).

$$\Delta T = \frac{\beta}{\rho \cdot C_p} \int_0^{\varepsilon_p} \sigma \, d\varepsilon_p \qquad \text{Eq. (2.12)}$$

Where β is the ratio of plastic work converted into heat, ρ is the material density, C_p is the heat capacity of the material, and the remainder is the integral of the flow stress curve which is calculated as the area under the flow stress curve.

MacDougall [135] found that, approximately 90% of the plastic work within the specimen is converted to heat energy, while rest is converted to other types of energy, such as sound, microstructural change, etc. For high strain rate experiments, β is taken to be equal to 0.9, while β is assumed to be 0 for low strain rate testing due to isothermal assumption. For intermediate strain rate testing, a condition that is intermediate to both isothermal and adiabatic conditions is typically considered [6]. A detailed method for calculating the amount of heat generated within the specimen during intermediate strain rate testing can be found in [6].

2.5.4 Data Manipulation

The raw flow stress data converted from raw engineering stress-strain was interpolated at strain increments of 0.2% effective plastic strain (eg. 0.2%,0.4%,0.6%,etc.), and the individual interpolated curves were used to create a single average flow stress curve for each strain rate condition. The averaged curves were used for the constitutive modeling so that each experiment condition is weighted equally in the constitutive fits since they each have the same number of data points.

CHAPTER 3

EXPERIMENTAL RESULTS

In this chapter, the experimental results for each material are discussed, beginning with the stress-strain behavior that includes a discussion of strain rate sensitivity of flow stress, followed by the effect of strain rate on anisotropy. For AA5182-O, the influence of strain rate on the observed PLC effect is also discussed. The raw measured engineering stress-strain curves for all three materials along three (0˚, 45˚, and 90˚) sheet orientations at strain rates ranging from low (0.001 s^{-1}) to high (1000 s^{-1}) are presented in Appendix A.

3.1 STRESS-STRAIN BEHAVIOR

3.1.1 DP600

The effect of strain rate on the true stress versus effective plastic strain (or flow stress) along all three orientations is shown for DP600 steel in Figure 3.1-Figure 3.3. As expected, an increase in strength with increasing strain rate was observed for all three sheet orientations. The yield stress scales upwards with increasing strain rate and the shape of the flow stress curve (or the hardening behavior) remains consistent for all of the strain rates. The average true stress versus strain rate at 3%, 6%, and 12% effective plastic strain is plotted in Figure 3.4 with the error bars indicating the maximum and minimum measured values from the population of repeat tests. The error bars are greatest at a strain rate of 1000 s^{-1} due to minor oscillations within the stress signal as measured using the TSHB apparatus. It is worth noting that the specimens did not fail on the first loading pulse (~0.17 strain) for the TSHB tests due to limitations on the available striker length. The strain rate dependence of true stress is similar for all of the sheet metal orientations. The highest strength is observed along the transverse direction, while the stress along diagonal and rolling directions is found to be similar. The data indicates a small increase in strength from 0.001 s^{-1} to 0.1 s^{-1}, and high or moderate increase in stress as the strain rate increases from 0.1 s^{-1} to 1000 s^{-1}. For example, at 6% effective plastic strain, the increase in flow stress is approximately 17 MPa from 0.001 to 0.1 s^{-1} for all three sheet orientations, compared to approximately 100 MPa increase in stress as the strain rate increased from 0.1 to 1000 s^{-1}.

The temperature rise, ΔT due to adiabatic heating for tests conducted at high strain rate was calculated using Eq. (2.12). The maximum temperature rise at 0.13 effective plastic strain was calculated to be only 22 °C; thus, can be considered negligible.

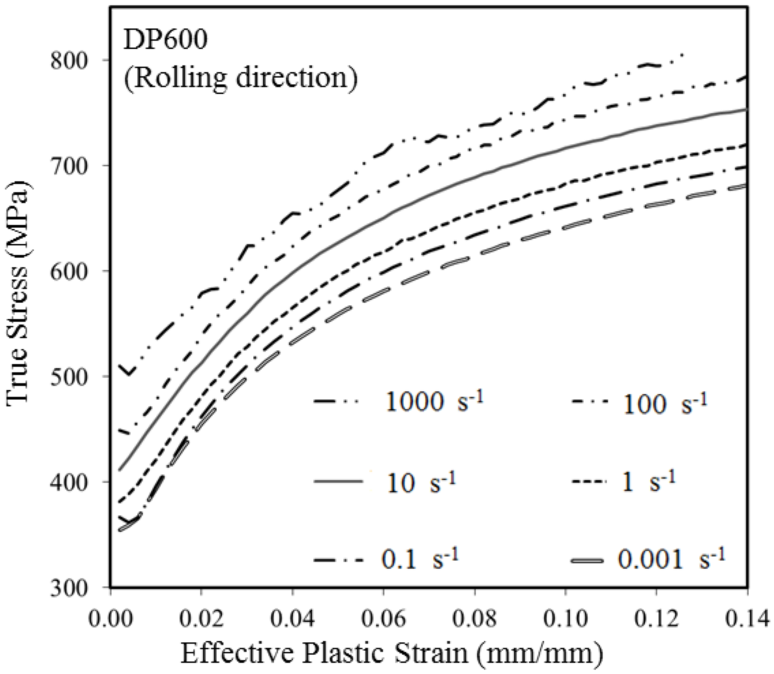

Figure 3.1: Averaged flow stress curves for DP600 sheet specimens at room temperature and strain rates from 0.001 s^{-1} to 1000 s^{-1} along rolling direction.

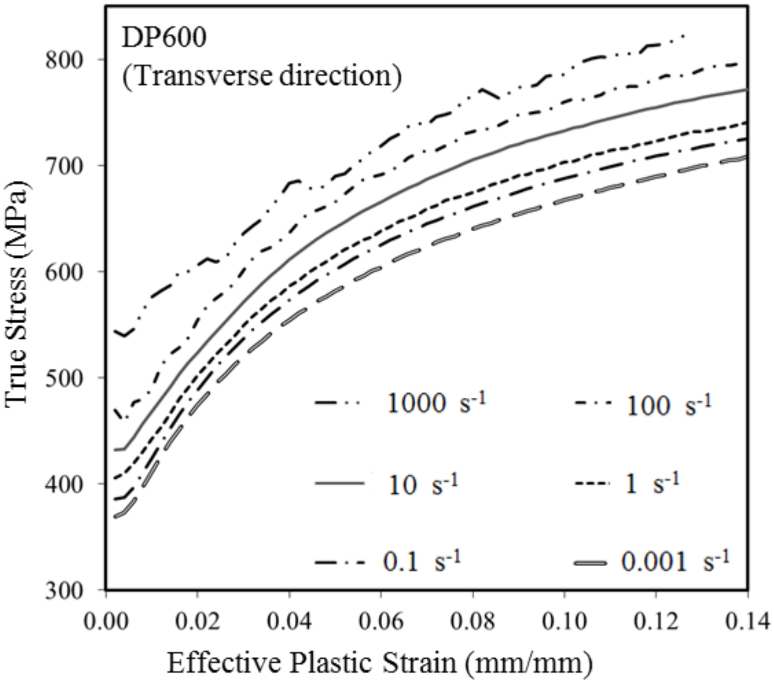

Figure 3.2: Averaged flow stress curves for DP600 sheet specimens at room temperature and strain rates from 0.001 s^{-1} to 1000 s^{-1} along transverse direction.

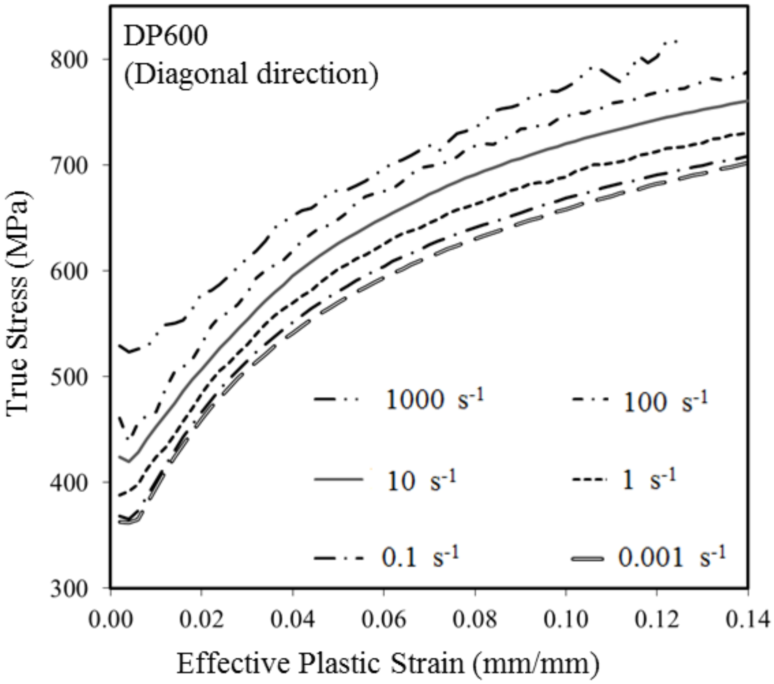

Figure 3.3: Averaged flow stress curves for DP600 sheet specimens at room temperature and strain rates from 0.001 s^{-1} to 1000 s^{-1} along transverse direction.

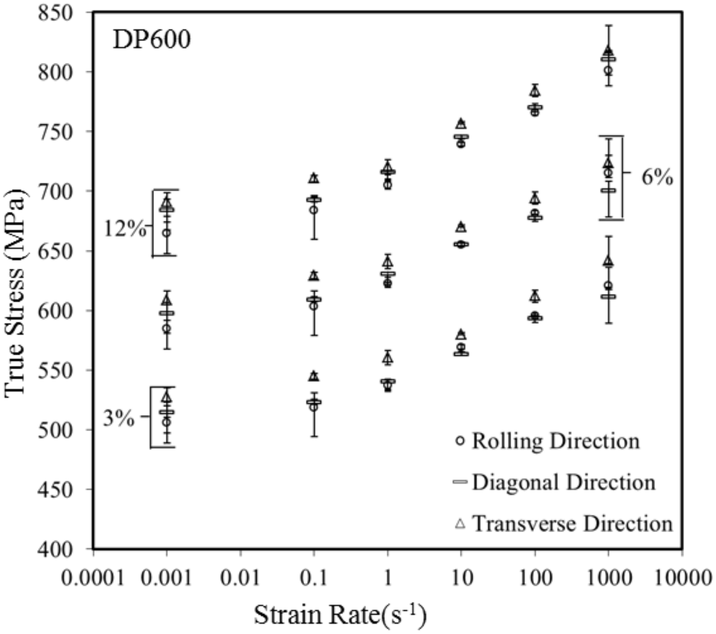

Figure 3.4: True stress vs. effective plastic strain for DP600 at 3%, 6%, and 12% effective plastic strains. The error bars indicate the maximum and minimum measured values from the population of repeat tests.

3.1.2 TRIP780

The strain rate dependent flow stress curves for TRIP780 are shown for all three orientations in Figure 3.5-Figure 3.7. Similar to the DP600 material, the yield strength of the TRIP780 scales vertically for increasing strain rates and the hardening behavior is nearly the same as the strain rate increases from 0.001 to 100 s^{-1}. At a strain rate of 1000 s^{-1}, the initial hardening behavior was quite different, as seen by a drop in stress to below that at 100 s^{-1} over a strain range of 0.03 to 0.08, indicating a lower initial strain hardening rate. Beyond a strain of 0.08, the hardening rate recovers and the stress increases to above that at 100 s^{-1}. The average flow stress at 4%, 8%, and 12% effective plastic strain is plotted against the strain rate in Figure 3.8. A negative rate sensitivity trend is observed in the flow stress data at strains of 4 and 8% at a strain rate of 1000 s^{-1}, while the expected positive rate sensitivity trend was observed at higher strains as reflected in the data at 12% strain. Figure 3.8 also indicates that the highest strength is observed along the TD while the DD strength was the lowest observed at all strain rates. For an increase in strain rate from 0.001 to 100 s^{-1}, the corresponding increase in average true stress (at 0.12 effective plastic strain) was found to be approximately 120, 92, and 119 MPa for the rolling, diagonal, and transverse direction, respectively.

At 4% effective plastic strain, the drop in average flow stress from 100 to 1,000 s^{-1} is found to be 15, 10, and 11 MPa for rolling, diagonal, and transverse direction, respectively. As a result, at 4% effective plastic strain, the flow stress of TRIP780 at 10 s^{-1} and 1000 s^{-1} was approximately the same.

The observed change in hardening behavior for the strain rate of 1000 s^{-1} tests was most likely due to the unique phase transformation behavior of TRIP780. The transformation of retained austenite to martensite may have been affected by the adiabatic heat rise generated at the higher strain rate, resulting in a decrease in volume fraction of martensite being transformed as discussed by prior researchers [36,54]. The adiabatic heat rise within the specimen up to 0.14 effective plastic strain was calculated using Eq. (2.12), and found to be approximately 30° C for the 1000 s^{-1} tests. Although this increase in temperature within the specimen due to adiabatic heating from plastic work is considerably low, but the time for heat dissipation is minimal at 1000 s^{-1} strain rate experiments as compared to the intermediate strain rate testing. Further studies involving microstructure analysis and experiments at different temperature conditions are required to understand the transformation mechanism of the matertensite with respect to the strain rates, and are beyond the scope of this present work.

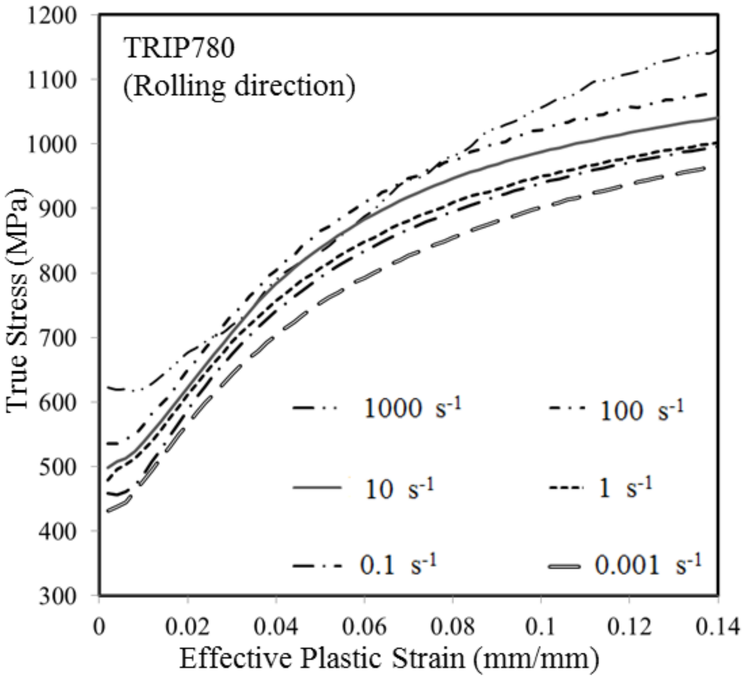

Figure 3.5: Averaged flow stress curves for TRIP780 sheet specimens at room temperature and strain rates from 0.001 s^{-1} to 1000 s^{-1} along rolling direction.

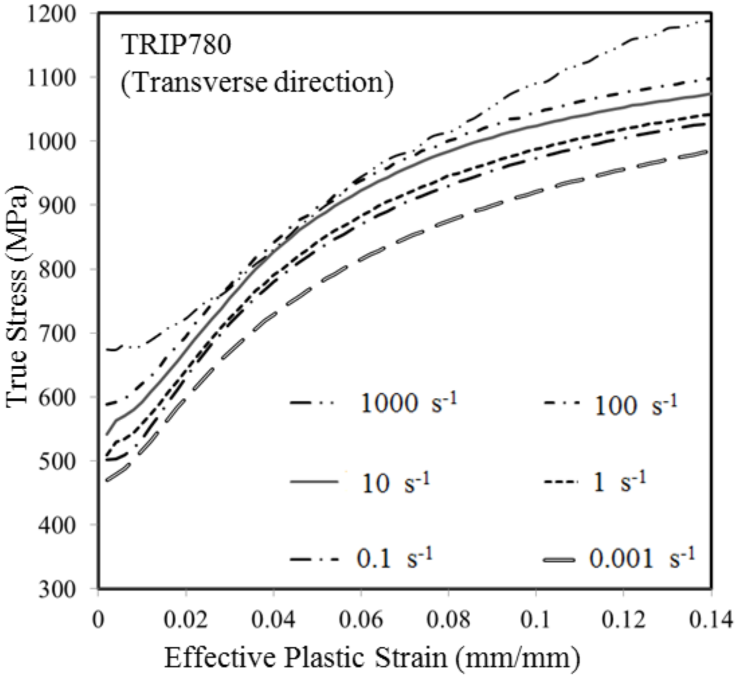

Figure 3.6: Averaged flow stress curves for TRIP780 sheet specimens at room temperature and strain rates from 0.001 s^{-1} to 1000 s^{-1} along transverse direction.

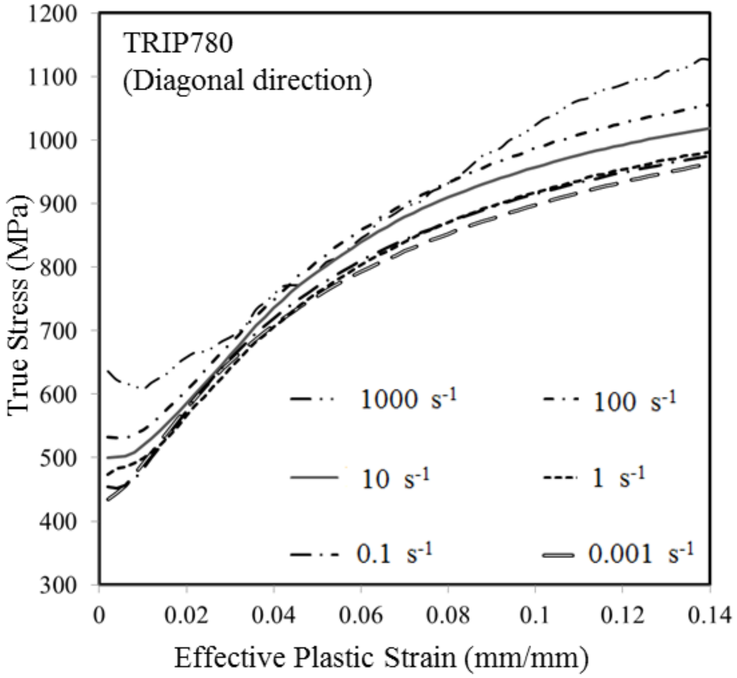

Figure 3.7: Averaged flow stress curves for TRIP780 sheet specimens at room temperature and strain rates from 0.001 s^{-1} to 1000 s^{-1} along diagonal direction.

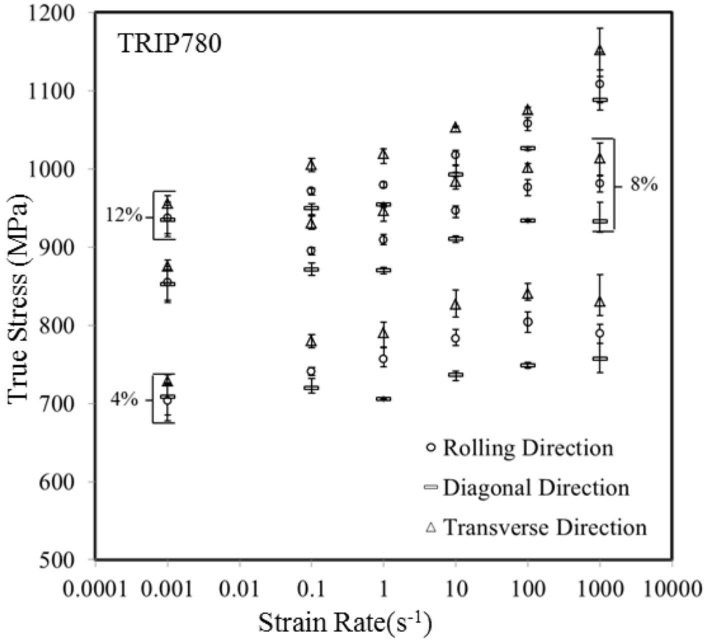

Figure 3.8: True stress vs. effective plastic strain for TRIP780 at 4%, 8%, and 12% effective plastic strains. The error bars indicate the maximum and minimum measured values from the population of repeat tests.

3.1.3 AA5182-O

Figure 3.9-Figure 3.11 shows the strain rate dependent flow stress behavior for the AA5182-O sheet metal along the three different sheet orientations. AA5182-O appears to be mildly rate sensitive in the range of strain rates considered. Figure 3.12 shows the true stress vs. true strain rate at 2%, 7%, and 13% logarithmic strain. The yield strength is largely rate-insensitive. At higher strains (7 and 13%), AA5182-O exhibits a mild negative rate sensitivity over the strain rate range from 0.001–1 s^{-1}, while at higher rates a mild positive strain rate sensitivity is observed. As shown in Figure 3.12, similar hardening behavior and rate sensitivity is observed for all three sheet orientations.

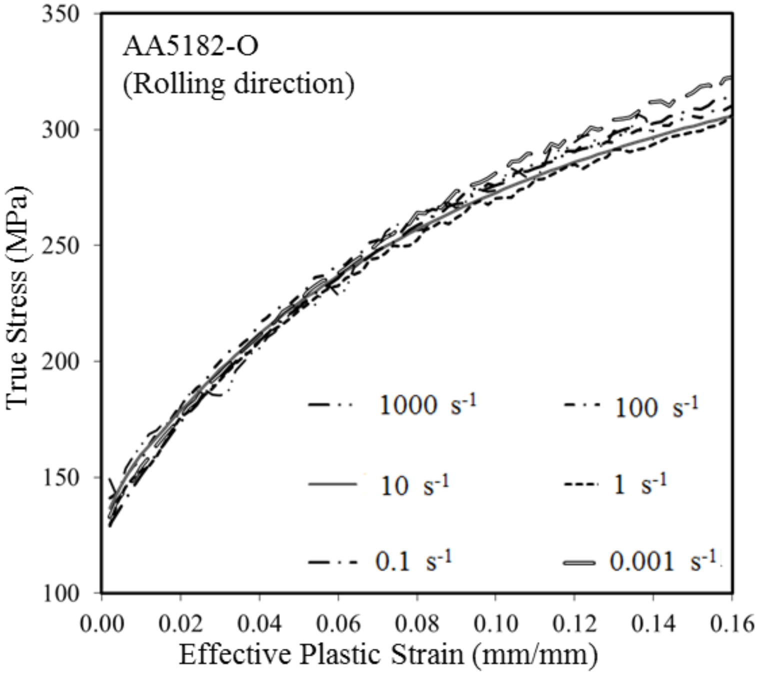

Figure 3.9: Averaged flow stress curves for AA5182-O sheet specimens at room temperature and strain rates from 0.001 s^{-1} to 1000 s^{-1} along rolling direction.

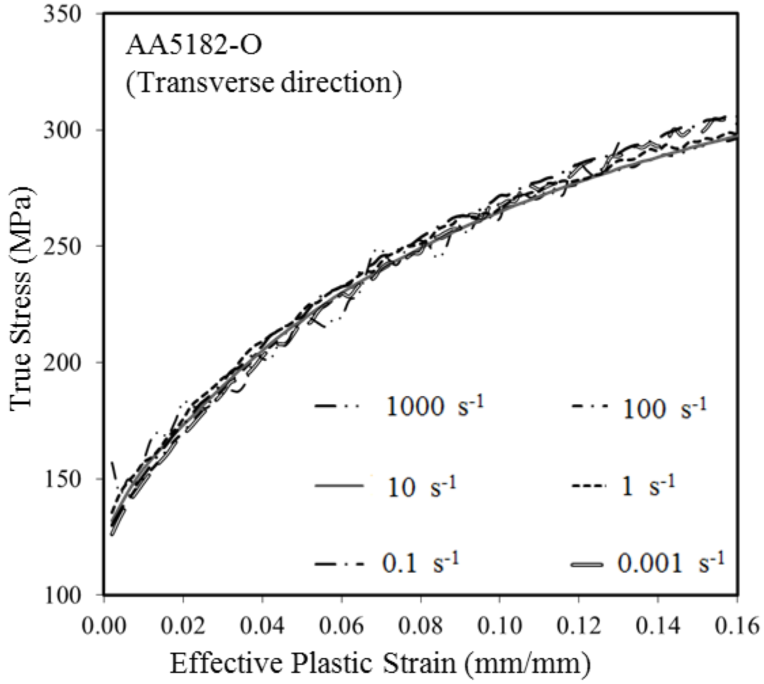

Figure 3.10: Averaged flow stress curves for AA5182-O sheet specimens at room temperature and strain rates from 0.001 s^{-1} to 1000 s^{-1} along transverse direction.

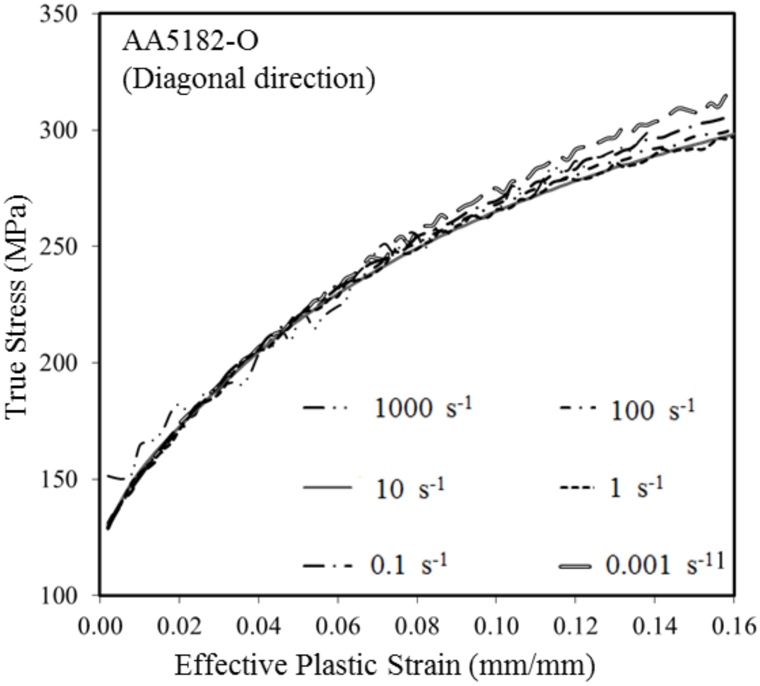

Figure 3.11: Averaged flow stress curves for AA5182-O sheet specimens at room temperature and strain rates from 0.001 s^{-1} to 1000 s^{-1} along diagonal direction.

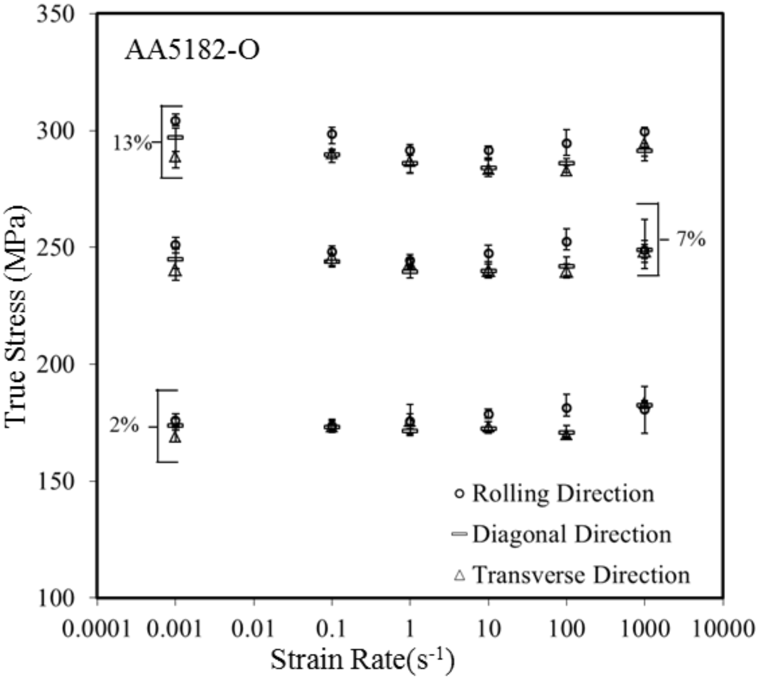

Figure 3.12: True stress vs. effective plastic strain for AA5182-O at 2%, 7%, and 13% effective plastic. The error bars indicate the maximum and minimum measured values from the population of repeat tests.

The drop in flow stress between 0.001 to 1 s^{-1} is found to be approximately 5-7 MPa and 10-12 MPa at 7% and 13% logarithmic strain, respectively, while a similar level of strength was recovered as the strain rate increased from 1 to 1000 s^{-1}. In order to confirm the observed mild negative rate sensitivity behavior, the measured data was compared with the data available in literature. The measured data was compared with the experimental data presented by Smerd [19], who performed room temperature tensile testing on 1.6 mm AA5182 sheet material along the rolling direction at quasi-static, 600, 1100, and 1500 s^{-1} strain rates. The data measured in this work closely agrees with the experimental data presented by Smerd [19] at quasi-static and high strain rates, as shown in Figure 3.13 which serves to validate the current data; however, Smerd et al. did not perform experiments at the intermediate strain rates considered in the current research.

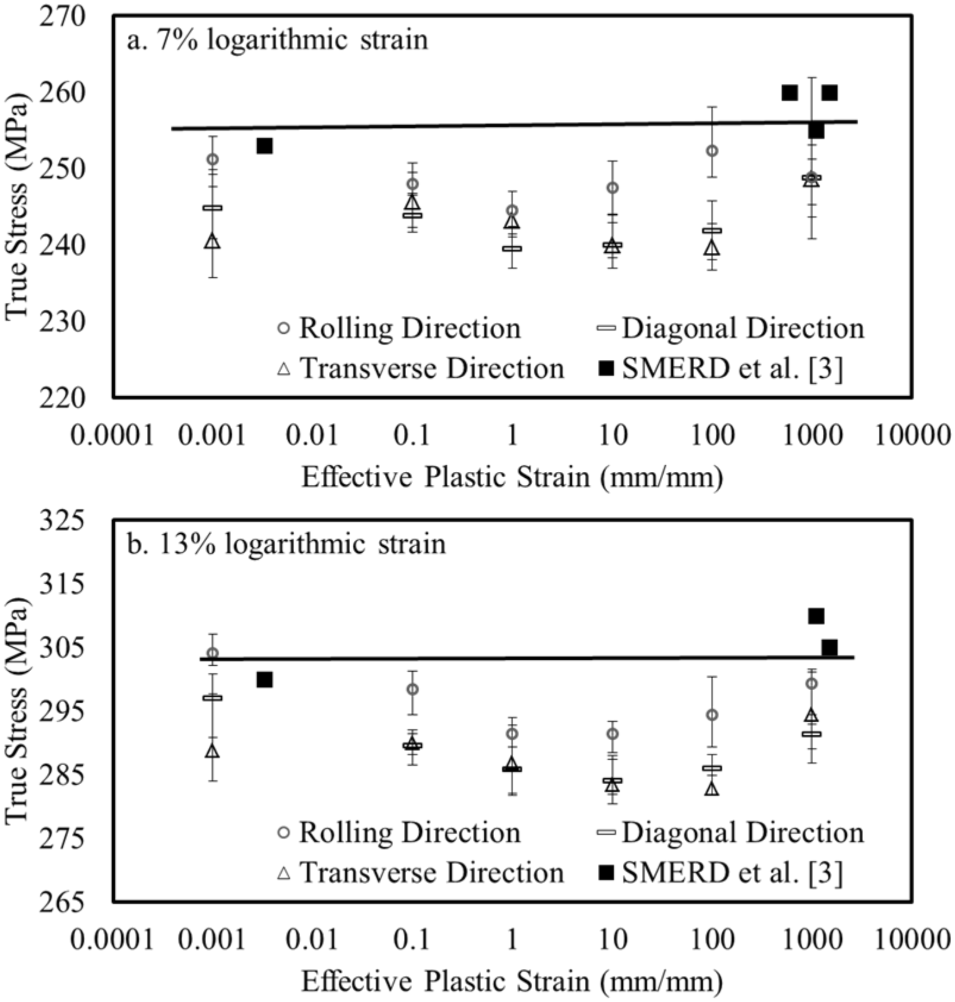

Figure 3.13: Comparison of true stress with the data measured by Smerd el al. [19] at (a) 7% and (b) 13% logarithmic strain.

The observed negative strain rate sensitivity in the AA5182-O samples was attributed to the PLC effect, as discussed by Abbadi et al.[58], Picu et al. [59], McCormick [60], Van den Beukel [61], Higashi et al. [55], Chihab et al. [62], and Kalk and Schwink [63,64]. In order to detect the presence of PLC bands, the engineering stress-strain curves from each individual test and testing condition were examined. In Figure 3.14, the raw stress-strain curves (not averaged) from single experiments at 0.001, 0.1, 1 and 10 s^{-1} are plotted. As can be seen in Figure 3.14(a-c), serrated stress-strain response and different types of PLC serrations were observed over the measured strain rate range from 0.001-1 s^{-1}, while no serrations were observed at the 10 s^{-1} strain rate (Figure 3.14d). A detailed explanation of the various PLC band types is covered in [62-64]; however, the data in Figure 3.14a exhibits serrations of the Type A-B, while Figure 3.14b and c exhibit Type A serrations.

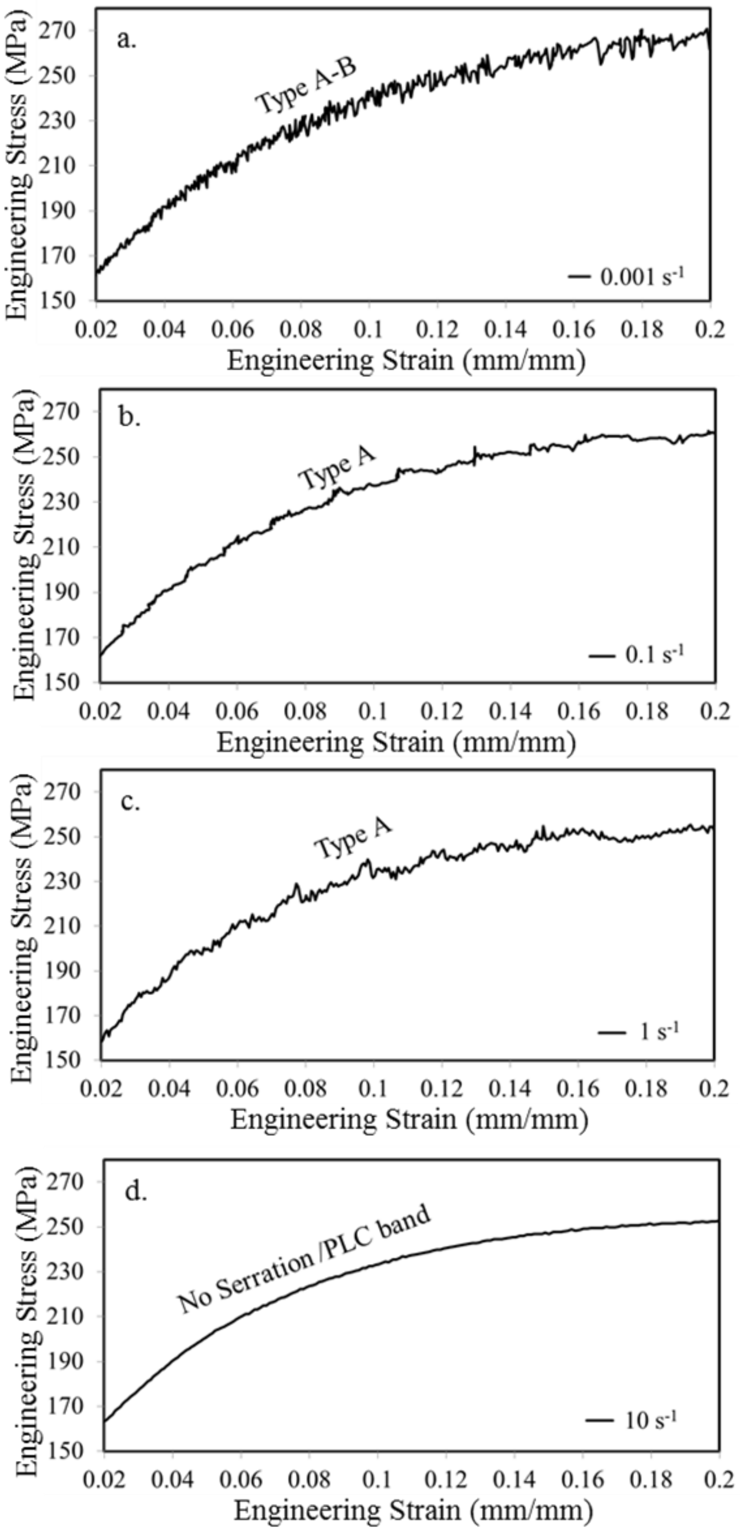

Figure 3.14: Presence of PLC band in the engineering stress vs strain curves of AA5182-O from a single test at a) 0.001 s^{-1} b) 0.1 s^{-1} c) 1 s^{-1} and d) 10 s^{-1} strain rate.

High speed DIC full-field strain measurements were used to investigate the propagation of plastic deformation bands during tensile testing. During post processing of the DIC images, 150 points were selected on a line along the gauge length of the specimen in order to track the PLC strain band propagation. The axial strain distributions at strain rates of 0.001, 0.1, and 1 s^{-1} are presented in Figure 3.15, Figure 3.16, and Figure 3.17, respectively, for various times in the deformation histories. PLC strain band nucleation and band propagation were observed up to a strain rate of 1 s^{-1}. The strain band nucleation is very apparent for all the lower strain rate cases where the strain bands continuously travel along the gauge length of the specimen over the entire duration of the plastic deformation up to necking. For the 0.001 s^{-1} test, type A-B serrations shown in Figure 3.14a correspond to strain distribution plots with multiple undulations and a pronounced strain band front at times greater than 36 s (Figure 3.15b). For the 0.1 s^{-1} and 1 s^{-1} tests, smoother strain distributions (no local undulations) with a pronounced strain band front were observed, as can be seen in Figure 3.16b and Figure 3.17b, respectively. The PLC effect was not observed for the 10 s^{-1} tests and the corresponding strain distribution along the gauge length during deformation remains uniform prior to necking as shown by the strain contours at different times in Figure 3.18a. In Figure 3.18b, the measured strain distribution plotted for different times during the test is also uniform (or flat) until a time of 0.026 s which corresponds to a uniform elongation of approximately 0.25. Beyond this time, the start of localization can be observed at a distance of approximately 1 mm below the centerline of the sample at a time of 0.029 s and a pronounced neck is observed at time 0.034 s.

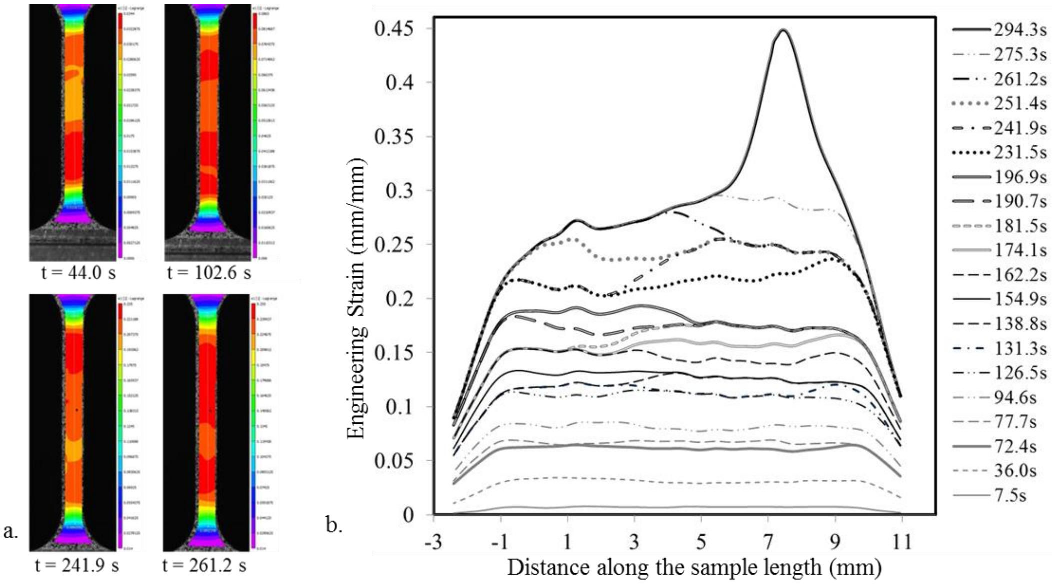

Figure 3.15: a) Engineering major strain contours (AA5182-O) along TD at 0.001 s^{-1} strain rate at different times during plastic deformation, b) corresponding strain distributions along specimen axis showing strain band nucleation and location of the strain band at different times (the negative position corresponds to the bottom end of the specimen shown in the DIC image in Figure 3.15a).

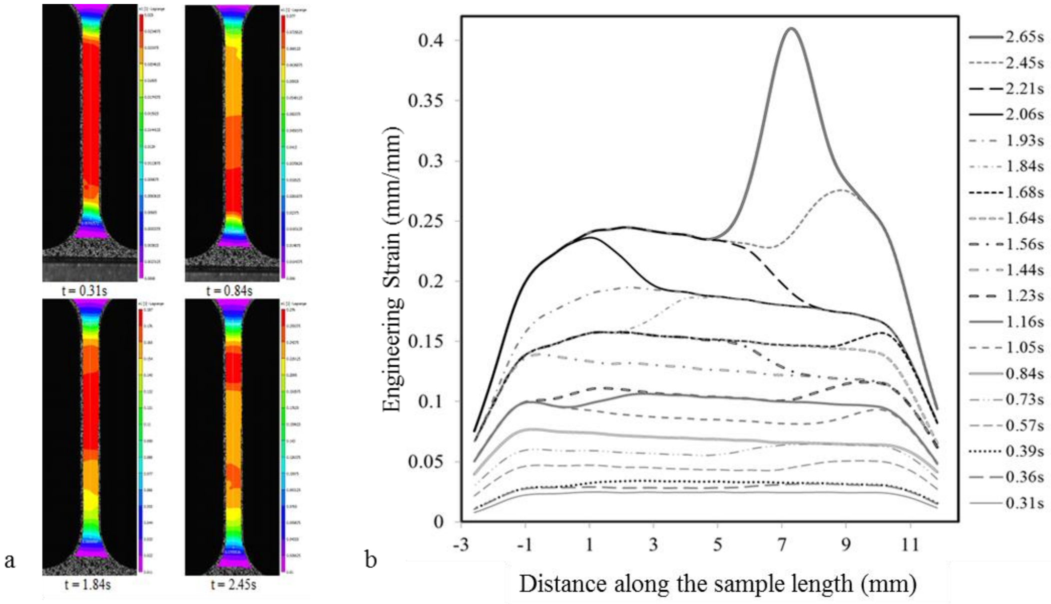

Figure 3.16: a) Engineering major strain contours (AA5182-O) along RD at 0.1 s^{-1} at different times during plastic deformation, b) corresponding strain distributions along specimen axis showing strain band nucleation and location of the strain band at different times during the test (the negative position corresponds to the bottom end of the specimen shown in the DIC image in Figure 3.16a).

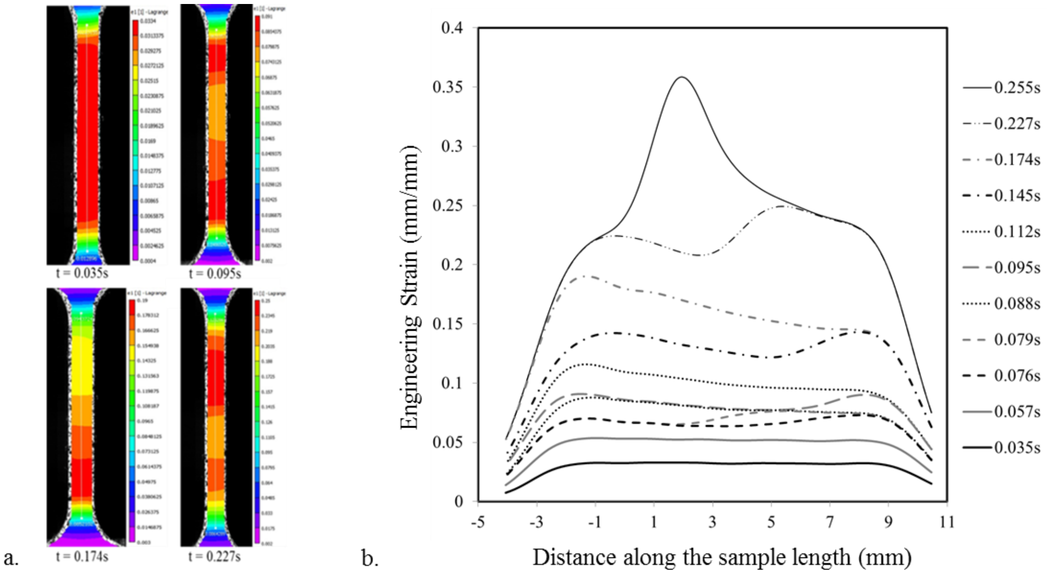

Figure 3.17: a) Engineering major strain contours (AA5182-O) along DD at 1 s^{-1} at different times during plastic deformation, b) corresponding strain distributions along specimen axis showing strain band nucleation and location of the strain band at different times during the test (the negative position corresponds to the bottom end of the specimen shown in the DIC image in Figure 3.17a).

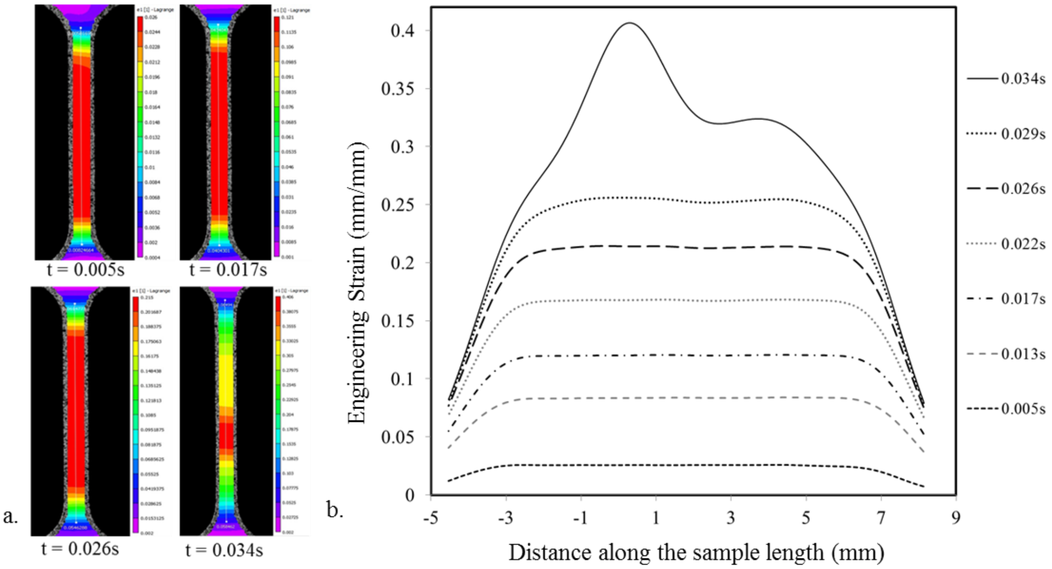

Figure 3.18: a) Engineering major strain contours (AA5182-O) along TD at 10 s^{-1} at different times during plastic deformation, b) corresponding strain distributions along specimen axis showing strain band nucleation and location of the strain band at different times during the test (the negative position corresponds to the bottom end of the specimen shown in the DIC image in Figure 3.18a).

The band propagation velocity was calculated by determining the distance travelled by the peak strain of the band and dividing it by the time lapsed to travel the distance. The band velocities at different strain rates were plotted against the strains in Figure 3.19. The band speed showed a slight decrease with strain while the band velocity increased with an increase in strain rate. The PLC band propagation was continuous for 0.1 and 1 s^{-1} strain rates, while occasional jumping was observed at a strain rate of 0.001 s^{-1}. This behavior agrees with the flow stress curves for 0.001 s^{-1} that showed a mixture of type A and B PLC bands [62].

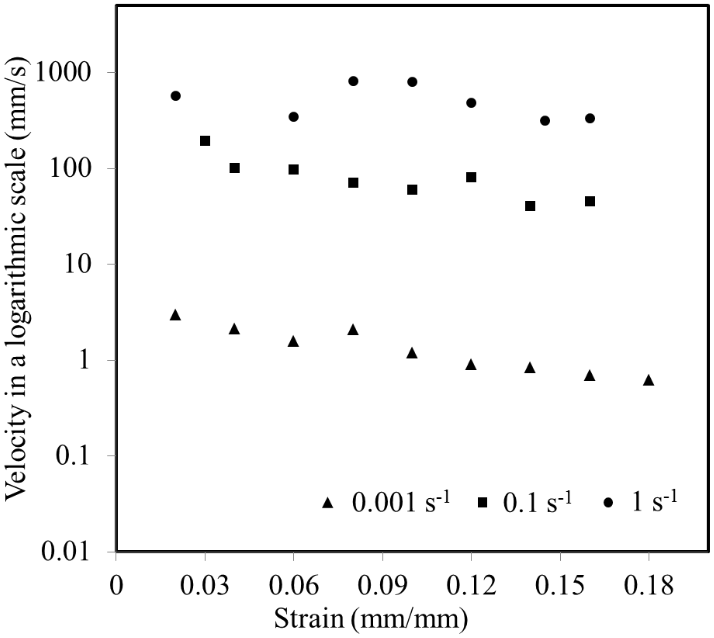

Figure 3.19: The measured PLC band velocity vs. strain at different strain rates.

3.2 STRAIN RATE EFFECT ON ANISOTROPIC BEHAVIOR

Figure 3.20 serves to illustrate the in-plane anisotropy in the measured flow stress for each alloy as a function of strain rate. Plotted is the flow stress under uniaxial tension in each material direction normalized by the flow stress in the RD. The data corresponds to that shown in Figure 3.1–Figure 3.12. The DP600 and TRIP780 flow stress data was taken at a strain of 0.12, while the AA5182-O flow stress data was taken at a strain of 0.13. The flow stress ratios plotted in Figure 3.20 do not indicate any definite trends with respect to strain rate, which indicates that the effect of strain rate on anisotropy (planar) appears to be negligible.

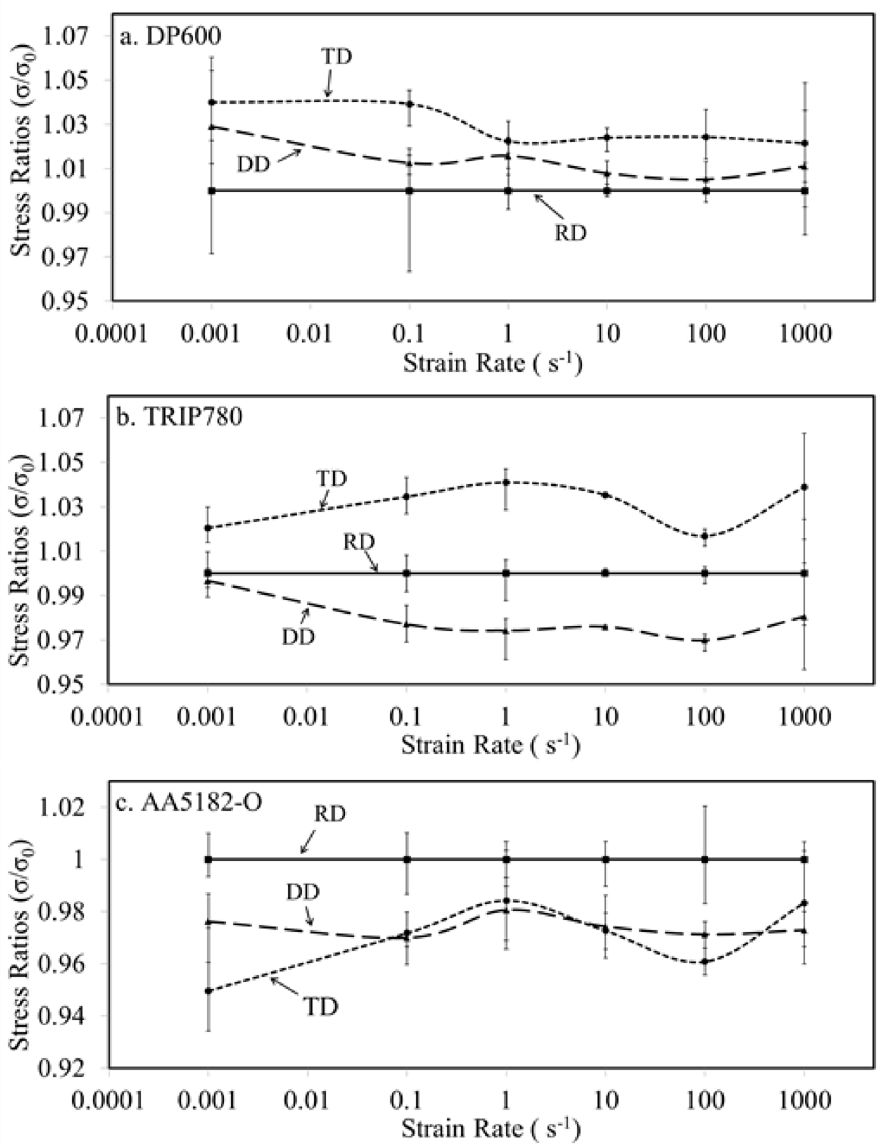

Figure 3.20: Flow stress ratio vs. strain rate for (a) DP600, (b) TRIP780, and (c) AA5182-O sheet metal alloys along rolling (RD), diagonal (DD), and transverse direction (TD). The flow stress was taken at a strain of 0.12 for DP600 and TRIP780 and at a strain of 0.13 for AA5182-O.

Resistance to thinning is characterized by a high width to thickness strain ratio under uniaxial tensile loading, referred to as the r–value (Lankford coefficient). For all of the individual tests conducted in this work, the r–value was calculated in the manner shown in Figure 3.21 for three repeat tests. Due to some variations in the r–value at the start and end of each test, the average r–value in the range 5 to 15 % strain was calculated for each individual test and then an average value for the group of repeat tests was calculated. Table 3.1 – Table 3.3 and Figure 3.22 summarizes the measured average r–values for each alloy at various strain rates and sheet metal orientations. Logarithmic trend lines were fit to the data points (not shown); however, rather low R-squared values were obtained suggesting either high scatter or low dependence of r–value upon strain rate for all three materials.

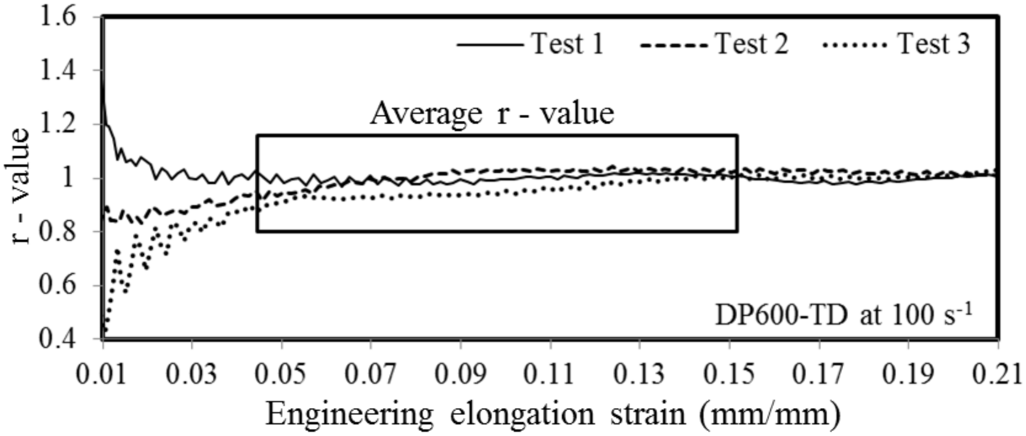

Figure 3.21: Lankford coefficient or r–value versus axial strain for 3 repeat tests of DP600-TD at 100 s^{-1} strain rate.

Table 3.1: r–values of DP600 sheet metal alloy at strain rate ranging from 0.001 to 1,000 s^{-1}.

Strain Rate (s^{-1})	**r–value (DP600)**								
	Rolling direction			***Diagonal direction***			***Transverse direction***		
	Max	***Avg.***	***Min***	***Max***	***Avg.***	***Min***	***Max***	***Avg.***	***Min***
0.001	0.69	**0.67**	0.65	0.95	**0.85**	0.79	0.83	**0.80**	0.77
0.1	0.89	**0.83**	0.71	0.93	**0.90**	0.87	1.06	**0.99**	0.90
1	0.82	**0.77**	0.72	1.00	**0.89**	0.80	1.02	**1.01**	0.99
10	0.83	**0.82**	0.81	0.92	**0.89**	0.85	1.07	**1.03**	0.99
100	0.77	**0.77**	0.77	0.90	**0.87**	0.81	1.01	**0.99**	0.96
1000	0.87	**0.85**	0.83	1.03	**0.98**	0.94	1.12	**1.07**	1.02
Avg.	0.81	**0.79**	0.75	0.95	**0.90**	0.84	1.02	**0.98**	0.94

Table 3.2: r–values of TRIP780 sheet metal alloy at strain rate ranging from 0.001 to 1,000 s^{-1}.

Strain Rate (s^{-1})	**r–value (TRIP780)**								
	Rolling direction			***Diagonal direction***			***Transverse direction***		
	Max	***Avg.***	***Min***	***Max***	***Avg.***	***Min***	***Max***	***Avg.***	***Min***
0.001	0.48	**0.47**	0.46	0.96	**0.86**	0.71	0.57	**0.55**	0.53
0.1	0.51	**0.50**	0.47	0.83	**0.80**	0.77	0.68	**0.61**	0.55
1	0.55	**0.53**	0.49	0.87	**0.80**	0.75	0.72	**0.69**	0.66
10	0.56	**0.52**	0.48	0.84	**0.80**	0.78	0.69	**0.66**	0.59
100	0.56	**0.53**	0.52	0.80	**0.75**	0.69	0.64	**0.62**	0.61
1000	0.59	**0.59**	0.57	0.89	**0.86**	0.83	0.72	**0.69**	0.67
Avg.	0.54	**0.52**	0.50	0.86	**0.81**	0.76	0.67	**0.64**	0.60

Table 3.3: r–values of AA5182-O sheet metal alloy at strain rate ranging from 0.001 to 1,000 s^{-1}.

Strain Rate (s^{-1})	**r–value (AA5182-O)**								
	Rolling direction			***Diagonal direction***			***Transverse direction***		
	Max	***Avg.***	***Min***	***Max***	***Avg.***	***Min***	***Max***	***Avg.***	***Min***
0.001	0.66	**0.62**	0.60	0.64	**0.63**	0.62	0.60	**0.60**	0.59
0.1	0.88	**0.83**	0.78	0.90	**0.79**	0.66	0.78	**0.72**	0.64
1	0.71	**0.69**	0.66	0.77	**0.75**	0.72	0.76	**0.69**	0.61
10	0.65	**0.64**	0.62	0.80	**0.74**	0.72	0.67	**0.66**	0.65
100	0.70	**0.69**	0.69	0.76	**0.74**	0.72	0.71	**0.67**	0.62
1000	0.71	**0.69**	0.67	0.82	**0.78**	0.75	0.73	**0.70**	0.69
Avg.	0.72	**0.69**	0.67	0.78	**0.74**	0.70	0.71	**0.67**	0.63

The plastic anisotropy or r–value is greatest for the DD and TD orientations for the DP600 and TRIP780 respectively, with the lowest r–value being measured for the RD orientation for both steels. The effect of strain rate on plastic anisotropy appears to be minimal across the entire range of strain rates tested for both steels since no systematic trends were observed beyond the measured scatter of the data. The average (across all strain rates) DP600 r–value for the RD, DD and TD orientations are 0.79, 0.90 and 0.98 respectively, while the average TRIP780 r–value for the RD, DD and TD orientations are 0.52, 0.81 and 0.64 respectively.

AA5182-O shows a minimal variation in r–values with respect to sheet orientation with a slightly higher r–value measured for the DD orientation for most strain rates. Since the r–value did not vary much with respect to orientation or strain rate, the average of all the r–values measured, 0.7, can be used to describe the material anisotropy for all the conditions studied.

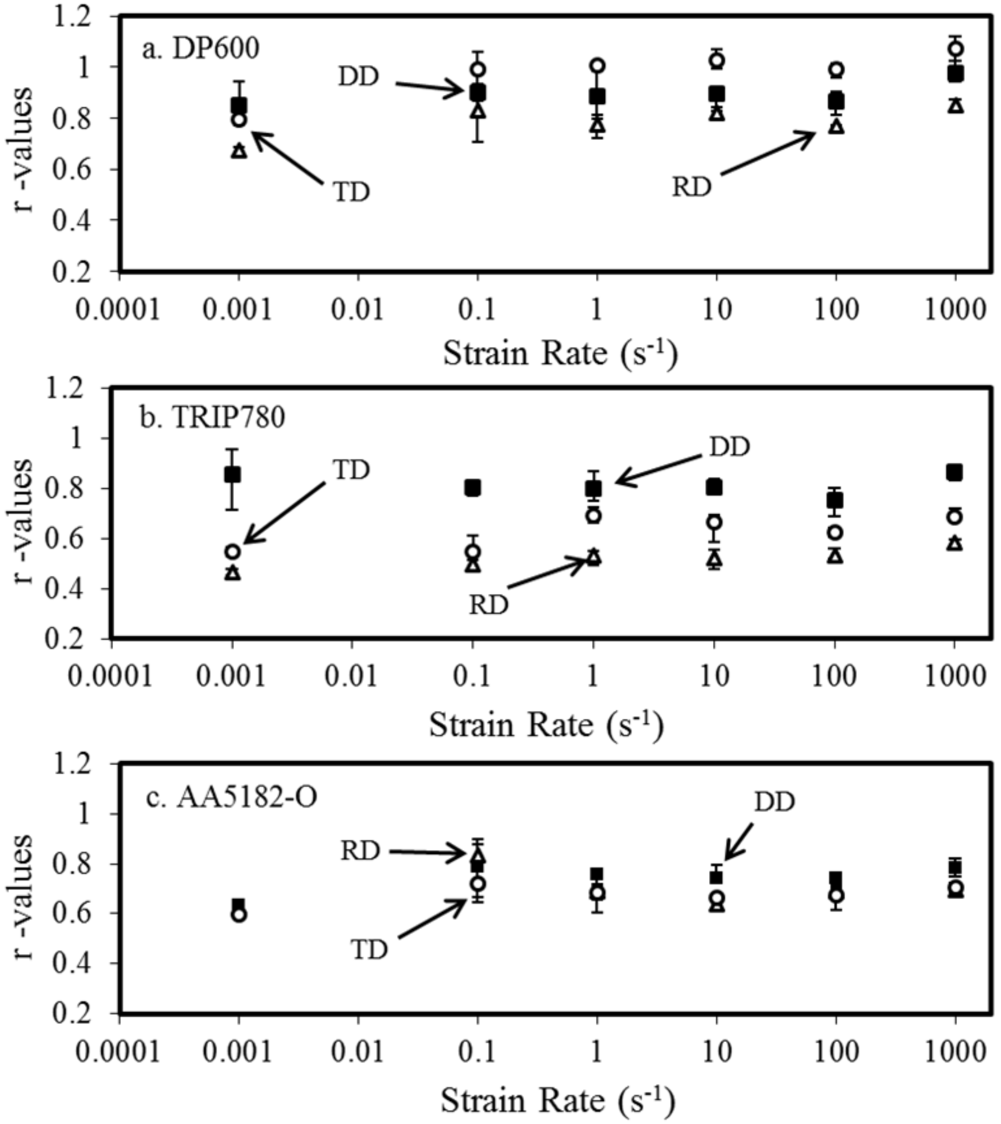

Figure 3.22: Lankford coefficient or r–value for (a) DP600, (b) TRIP780, and (c) AA5182-O at various strain rates.

3.3 SUMMARY

Figure 3.23 shows the change in strength (at 0.10 engineering strain) with strain rate for each alloy. DP600 and TRIP780 exhibit orientation dependent strength, however, this does not appear to change significantly with strain rate. Unlike the steel alloys, AA5182-O shows little to no variation in strength with respect to the three orientations tested in this work as shown in Figure 3.23. Both steel alloys (DP600 and TRIP780) showed positive rate sensitivity, while slight negative rate sensitivity was observed for AA5182-O and attributed to the PLC effect associated with the dynamic strain aging phenomena [57,61,63,64].

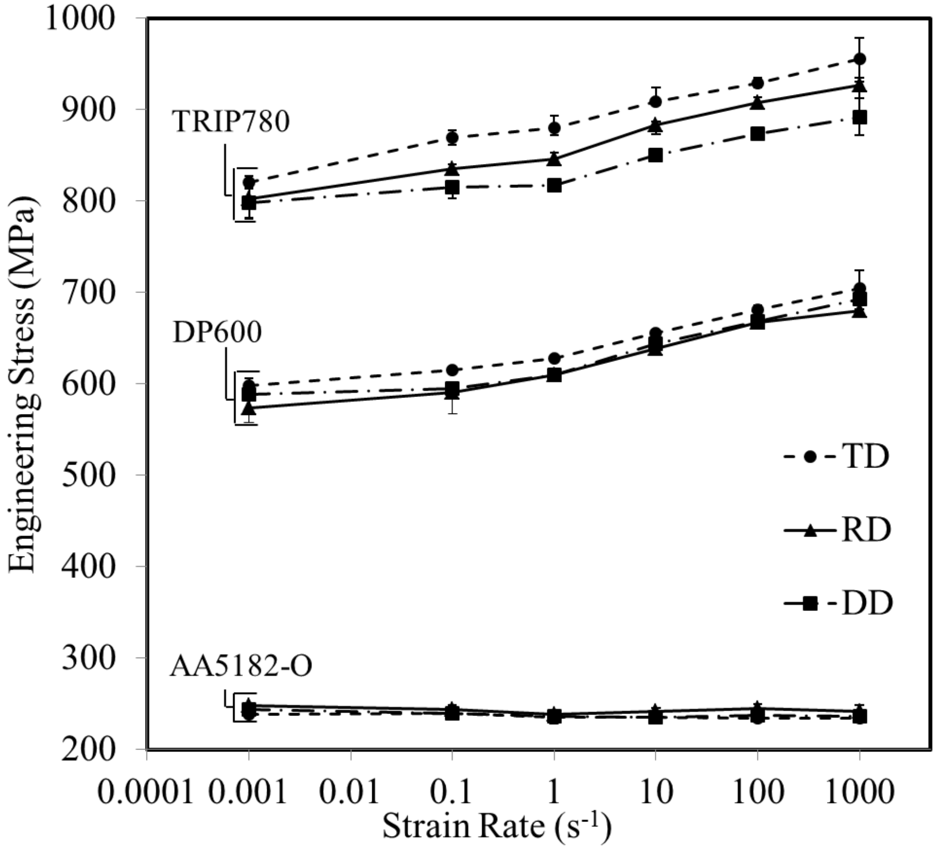

Figure 3.23: Engineering stress (at 0.10 engineering strain) vs. strain rate for DP600, TRIP780, and AA5182-O sheet metal alloys along rolling (RD), diagonal (DD), and transverse directions (TD).

The average r–values from all the strain rates are compared for DP600, TRIP780, and AA5182-O sheet metal alloys along all three sheet orientations, as shown in Figure 3.24. DP600 exhibits the highest r–value among all three materials tested. The higher r–value of the DP600 steel makes it more attractive from a forming perspective due to better thinning resistance for all orientations. As compared to DP600 and TRIP780 steels, AA5182-O has the lowest r–value along diagonal direction, while AA5182-O exhibits similar r–value along all three sheet orientations. The lower r–value for TRIP780 along the rolling direction suggests the least resistance to thinning of the sheet metal along the rolling direction as compared to the other sheet orientations.

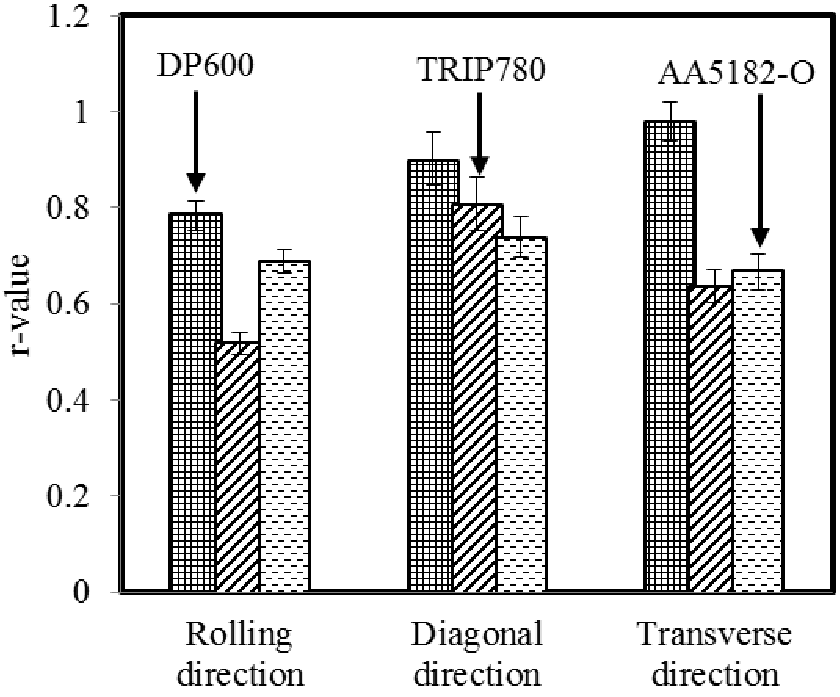

Figure 3.24: Comparison of r–values between DP600, TRIP780, and AA5182-O sheet metal alloys along rolling, diagonal, and transverse direction.

CHAPTER 4

CONSTITUTIVE MODELING

In order to enable future use of the measured stress-strain data within finite element (FE) simulations, strain rate-sensitive constitutive models were fit to the data using non-linear regression analysis. The statistical analysis software MYSTAT 12 was used to perform the non-linear regression analysis. The strain and strain rate values used in the model fitting were taken directly from the experimental data. The average stress-strain curves from three to five repeat tests for each test condition were used for the curve fitting.

Since the temperature rise due to adiabatic heating was small for the strain levels considered, thermal softening was not accounted for in the models presented in this work. This simplifying assumption is often adopted within the automotive industry for reduced computational cost when simulating vehicle crash events.

In this chapter, the constitutive parameters required by the Johnson-Cook [9] constitutive model, Zerilli-Armstrong [10] for BCC and FCC constitutive model, and Voce [11] hardening law with different strain rate functions are fit to the experimental results. The fits are presented for all three alloys along all three sheet orientations.

4.1 Johnson-Cook Constitutive Model Fits

The Johnson-Cook [9] constitutive model is described by Eq. (1.22), and re-stated here:

$$\sigma = (A + B\varepsilon^{n})(1 + C\ln(\dot{\varepsilon}^{*}))(1 - T^{*m}) \qquad \text{Eq. (1.22)}$$

where, σ is the true stress, ε is the equivalent plastic strain, $\dot{\varepsilon}^{*}$ is the dimensionless plastic strain rate, and T^{*} is the homologous temperature (given as shown in Eq. (1.23)). A, B, n, C, and m are the material constants fit to data collected for a particular material. Further detailed descriptions of these parameters are described in Section 1.7.1.

In current work, the temperature term and material constants associated with the temperature term ($T^{*} and\ m$) shown in Eq. (1.22) were not accounted in the curve fitting due to the room temperature testing condition and negligible adiabatic heat rise assumption. The resulting parameters for the Johnson-Cook constitutive models are tabulated in Table 4.1-Table 4.3 for all three materials along all three sheet orientations, as well as the R-squared value for the curve fittings and their upper and lower bounds for a 95% confidence interval. The Johnson-Cook constitutive fits for DP600, TRIP80, and AA5182-O sheet materials along rolling direction are shown in Figure 4.1, Figure 4.2, and Figure 4.3, respectively. Figure 4.1-Figure 4.3 includes the Johnson-Cook constitutive model fitting for the strain rates ranging from 0.001 to 1000 s^{-1}.

Table 4.1: Constitutive parameters for the DP600 averaged curves fit with the Johnson-Cook model.

		A	B	n	C	R^2
DP600 (Rolling direction)	Estimate	194	839	0.23	0.015	0.934
	95% Lower	158	814	0.21	0.014	
	95% Upper	231	864	0.25	0.016	
DP600 (Diagonal direction)	Estimate	200	900	0.23	0.014	0.962
	95% Lower	36	803	0.14	0.012	
	95% Upper	360	997	0.32	0.015	
DP600 (Transverse direction)	Estimate	216	900	0.24	0.014	0.968
	95% Lower	105	938	0.17	0.013	
	95% Upper	328	962	0.31	0.015	

Table 4.2: Constitutive parameters for the TRIP780 averaged curves fit with the Johnson-Cook model.

		A	B	n	C	R^2
TRIP780 (Rolling direction)	Estimate	202	1635	0.33	0.011	0.982
	95% Lower	155	1609	0.31	0.01	
	95% Upper	249	1661	0.36	0.012	
TRIP780 (Diagonal direction)	Estimate	200	1600	0.33	0.011	0.971
	95% Lower	128	1562	0.28	0.01	
	95% Upper	272	1638	0.37	0.012	
TRIP780 (Transverse direction)	Estimate	249	1592	0.33	0.011	0.983
	95% Lower	211	1572	0.31	0.01	
	95% Upper	288	1612	0.36	0.012	

Table 4.3: Constitutive parameters for the AA5182-O averaged curves fit with the Johnson-Cook model.

		A	B	n	C	R^2
AA5182-O (Rolling direction)	Estimate	88	475	0.42	-0.0021	0.991
	95% Lower	82	469	0.41	-0.0024	
	95% Upper	93	481	0.44	-0.0017	
AA5182-O (Diagonal direction)	Estimate	115	483	0.5	-0.0022	0.986
	95% Lower	111	474	0.49	-0.0027	
	95% Upper	118	492	0.52	-0.0018	
AA5182-O (Transverse direction)	Estimate	116	469	0.5	-0.0016	0.985
	95% Lower	112	461	0.48	-0.0021	
	95% Upper	119	479	0.52	-0.0012	

As seen in Figure 4.1 and Figure 4.2, the strain hardening behavior of the DP600 and TRIP780 material conditions tested could not be captured accurately by the power-law strain hardening function and logarithmic rate sensitivity inherent within the Johnson-Cook model. The flow stress prediction of the model for DP600 material was close to the experimental value for the strain rates ranging from 0.1–100 s^{-1} but only above 6% effectively plastic strain, while the experimental data was not captured at all in the case of 0.001 s^{-1} strain rate. The model predictions follow the experimental data closely for the TRIP80 material at all strain rates considered, but are unable to capture the strain hardening behavior precisely. The R^2 value of the non-linear regression fits is slightly higher for TRIP780 material than DP600 material. However, the upper and lower bound values of the model parameters are found to be quite high (i.e. on an average over 20%, 5%, and 18% for parameter A, B and n, respectively) indicating low reliability of the model for both AHSS materials.

.

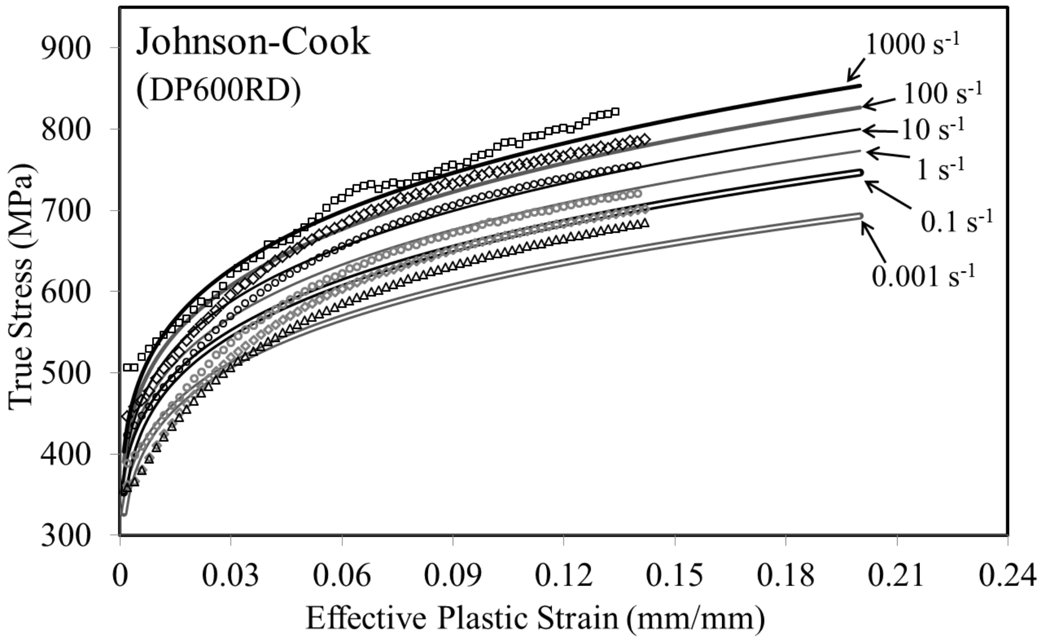

Figure 4.1: Johnson-Cook constitutive model fits (lines) to the experimental flow stress data (data points) for DP600 sheet material along rolling direction.

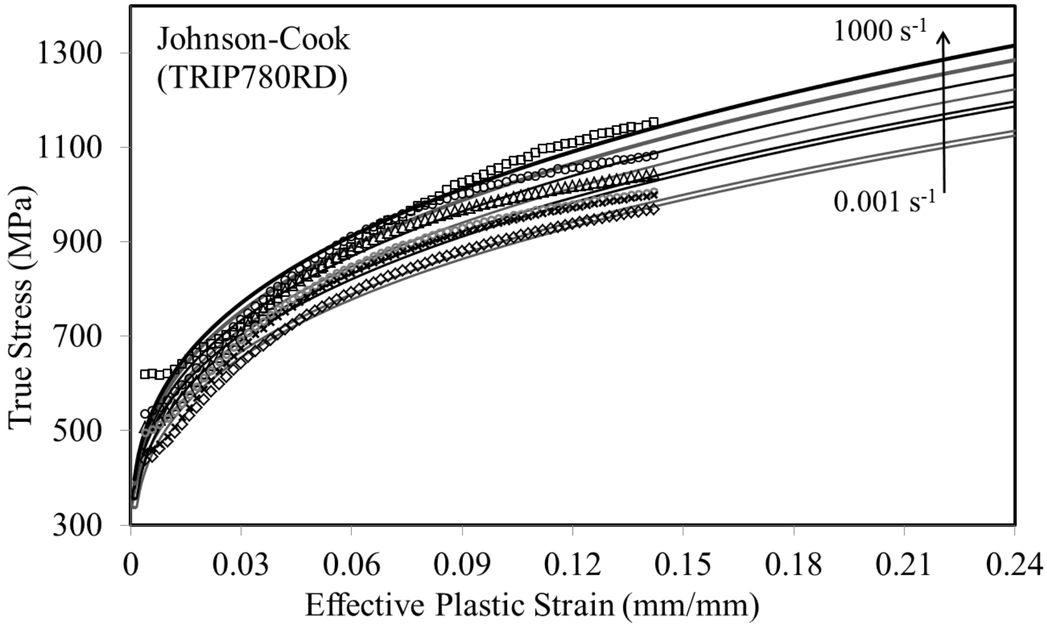

Figure 4.2: Johnson-Cook constitutive model fits (lines) to the experimental flow stress data (data points) for TRIP780 sheet material along rolling direction.

In the case of AA5182-O, the model predictions follow the experimental data adequately in terms of strain hardening, as shown in Figure 4.3(a-b). However, the concern here is whether the model can capture the strain rate dependent behavior of the material. As seen in Table 4.3, the values for the strain rate parameter C are negative, resulting in the model predicting negative strain rate sensitivity over the entire range of strain rates tested herein. The stresses at 2%, 7%, and 13% effective plastic strain are plotted against the strain rates in Figure 4.3(c). The figure shows that the model captures the drop in flow stress between 0.001 to 1 s^{-1} strain rates, but is unable to capture the stress recovery as the strain rate is increased over the range 1 to 1,000 s^{-1}. This was expected because the strain rate function used in the Johnson-Cook model is only a logarithmic term, which cannot account for this transition from negative to positive rate sensitivity with an increase in strain rate. The R^2 value of the data fits are found to be over 0.98 for the AA5182-O material along all three directions, as shown in Figure 4.3. The upper and lower bound values are found to be within 5% on an average for all the parameters of the model.

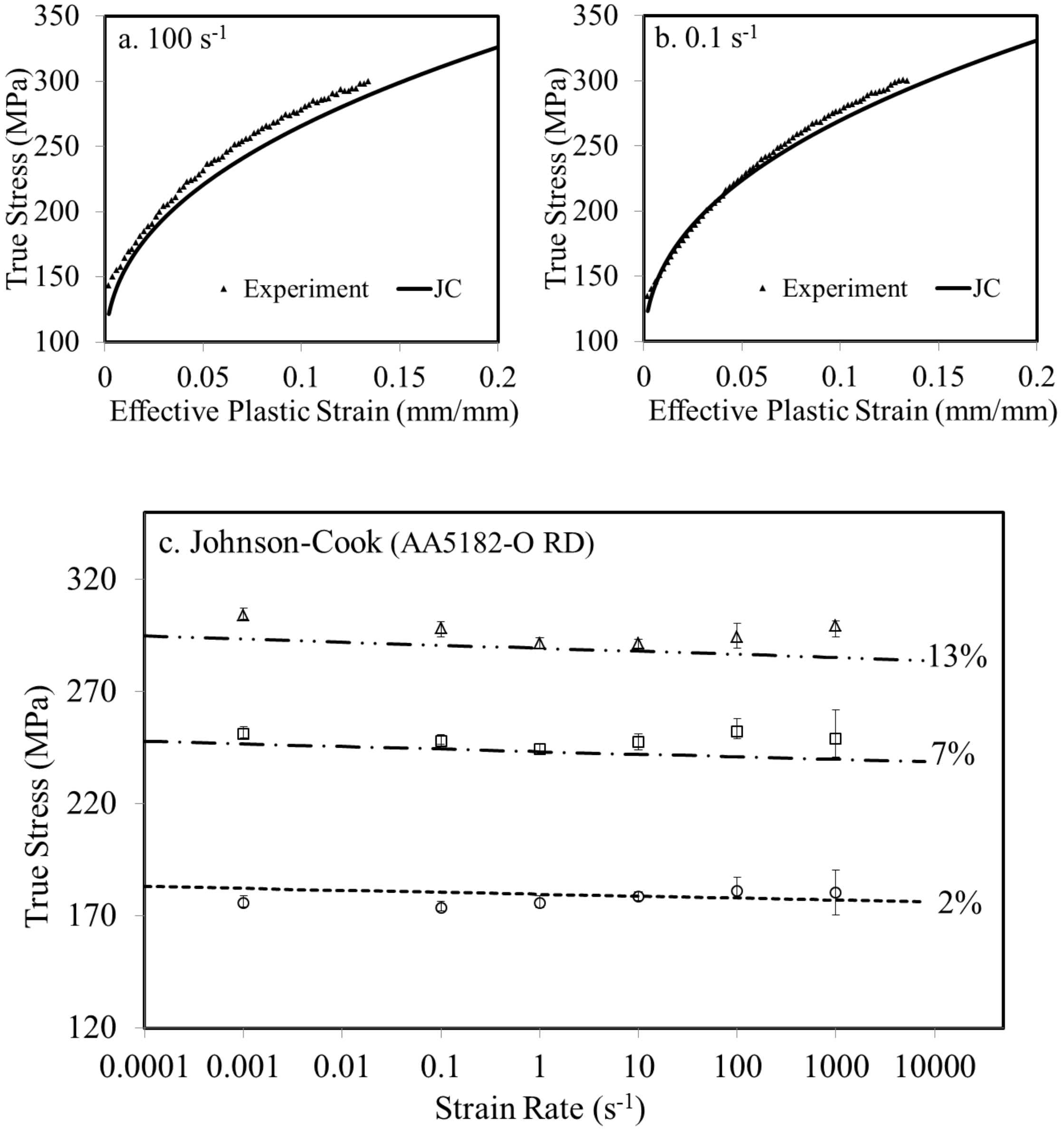

Figure 4.3: Johnson-Cook constitutive model fits (lines) to the experimental flow stress data (data points) for AA5182-O sheet material along rolling direction at (a) 100 and (b) 0.01 s-1 strain rate, and (c) comparison between the tensile strength predicted at different strain rates using the Johnson-Cook model and measured data at 2%, 7%, and 13% strains.

4.2 Zerilli-Armstrong Constitutive Model Fits

The Zerilli-Armstrong [10] constitutive models for BCC and FCC materials are given in Eq. (1.28) and Eq. (1.31), respectively, and re-stated here:

$$\sigma = \Delta\sigma_G + C_1 exp(-C_3 T + C_4 \cdot T \cdot \ln\dot{\varepsilon}) + C_5 \varepsilon^n + kl^{-1/2} \qquad \text{Eq. (1.28)}$$

$$\sigma = \Delta\sigma_G + C_2 \varepsilon^{1/2} exp(-C_3 T + C_4 \cdot T \cdot \ln\dot{\varepsilon}) + kl^{-1/2} \qquad \text{Eq. (1.31)}$$

where, $\Delta\sigma_G$ represents the athermal components of stress, $\dot{\varepsilon}$ is the plastic strain rate, T is the absolute temperature, C_1, C_2, C_3, C_3, C_4, C_5 and n are the material constants, and $kl^{-1/2}$ represents the effect of grain size (Hall-Petch effect) on the flow stress of the material. Since the parameters related to grain size are unknown for these alloys investigated at the time of this work, $kl^{-1/2}$ term was set to zero, reducing the number of required parameter. Further detailed descriptions of the model parameters are described in Chapter 1.3.2.

The resulting parameters for the Zerilli-Armstrong constitutive models are tabulated in Table 4.4-Table 4.6 for all three materials along all three sheet orientations, as well as the R-squared values for the curve fits and their upper and lower bounds for a 95% confidence interval. The Zerilli-Armstrong constitutive fits for DP600, TRIP80, and AA5182-O sheet materials along transverse sheet orientation is shown in Figure 4.4, Figure 4.5, and Figure 4.6, respectively. Figure 4.4-Figure 4.6 includes the Zerilli-Armstrong constitutive model fitting for the strain rates ranging from 0.001 to 1,000 s^{-1}.

Table 4.4: Constitutive parameters for the DP600 averaged curves fit with the Zerilli-Armstrong model for BCC materials.

		$\Delta\sigma_G$	C_1	C_3	C_4	n	C_5	R^2
DP600 (Rolling direction)	Estimate	140	4400	0.013	0.00028	0.3	900	0.965
	95% Lower	103	2990	0.013	0.0002	0.28	882	
	95% Upper	176	5809	0.013	0.00036	0.32	918	
DP600 (Diagonal direction)	Estimate	165	3000	0.011	0.0003	0.36	993	0.987
	95% Lower	140	2471	0.011	0.00025	0.34	978	
	95% Upper	190	3529	0.011	0.00035	0.39	1008	
DP600 (Transverse direction)	Estimate	150	4450	0.013	0.00028	0.289	910	0.951
	95% Lower	113	2817	0.013	0.0002	0.272	888	
	95% Upper	187	6087	0.013	0.00036	0.306	932	

Table 4.5: Constitutive parameters for the TRIP780 averaged curves fit with the Zerilli-Armstrong model for BCC materials.

		$\Delta\sigma_G$	C_1	C_3	C_4	n	C_5	R^2
TRIP780 (Rolling direction)	Estimate	220	3000	0.012	0.00049	0.4	1660	0.976
	95% Lower	152	1889	0.012	0.00033	0.35	1589	
	95% Upper	288	4111	0.012	0.00066	0.45	1732	
TRIP780 (Diagonal direction)	Estimate	243	3084	0.016	0.00083	0.41	1675	0.982
	95% Lower	210	1927	0.016	0.00061	0.38	1633	
	95% Upper	276	4242	0.016	0.00106	0.44	1717	
TRIP780 (Transverse direction)	Estimate	200	2975	0.01	0.00025	0.4	1600	0.982
	95% Lower	142	1908	0.01	0.00016	0.37	1566	
	95% Upper	257	4042	0.01	0.00035	0.43	1633	

Table 4.6: Constitutive parameters for the AA5182-O averaged curves fit with the Zerilli-Armstrong model for FCC materials.

		$\Delta\sigma_G$	C_2	C_3	C_4	R^2
AA5182-O (Rolling direction)	Estimate	112	729	0.0013	-0.00001	0.989
	95% Lower	110	721	0.0013	-0.00001	
	95% Upper	114	737	0.0013	-0.00001	
AA5182-O (Diagonal direction)	Estimate	114	706	0.0013	-0.00001	0.987
	95% Lower	112	705	0.0013	-0.00001	
	95% Upper	115	707	0.0013	-0.00001	
AA5182-O (Transverse direction)	Estimate	115	685	0.0013	-0.00001	0.985
	95% Lower	114	678	0.0013	-0.00001	
	95% Upper	117	692	0.0013	-0.00001	

The hardening behavior of DP600 at intermediate (10 and 100 s^{-1}) and high (1000 s^{-1}) strain rate was successfully captured by the Zerilli-Armstrong constitutive model for BCC materials, as shown in Figure 4.4. However, the performance of the model is found to be truncated in case of capturing the material behavior at low (0.001–1 s^{-1}) strain rates beyond 9% effective plastic strain. This is due to the strain rate effect on the flow stress of the material, which was not captured by the model precisely. Although the R^2 value of the non-linear regression fits are found to be adequately large (over 95%) for all the sheet orientations, the upper and lower bound values for a 95% confidence interval of some of the model parameters are found to be quite large (i.e. on an average over 20% for parameter $\Delta\sigma_G$ and C_1), indicating low reliability of the model for DP600 sheet metal alloy. Figure 4.5 shows the Zerilli-Armstrong constitutive model fits to the experimental flow stress data for TRIP780 sheet material along transverse direction. Unfortunately, the model was not able to capture the hardening behavior of TRIP780 sheet materials for the given strain rates. The model matched the experimental data accurately only between 4%– 9% effective plastic strain for the strain rates ranging from 0.001–100 s^{-1}, while the 1000 s^{-1} response was adequately captured only above 9% effectively plastic strain.

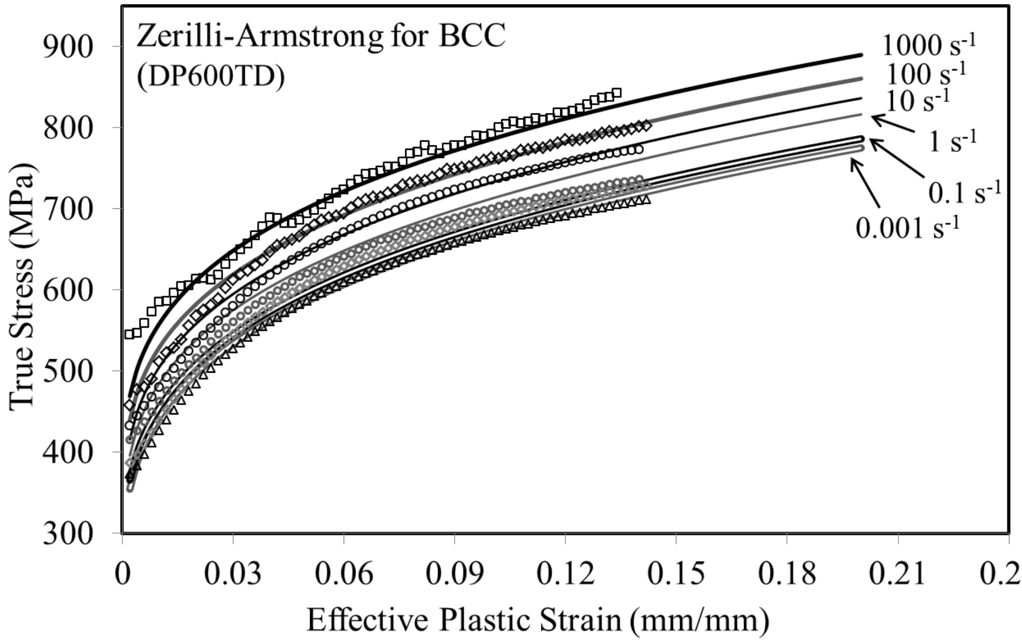

Figure 4.4: Zerilli-Armstrong for BCC constitutive model fits (lines) to the experimental flow stress data (data points) for DP600 sheet material along transverse direction.

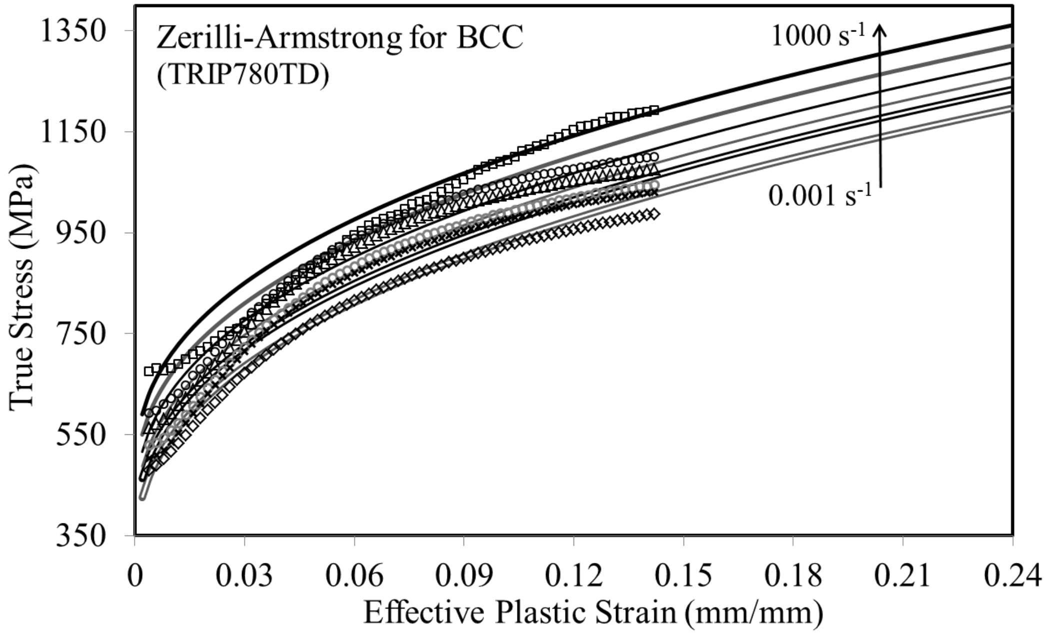

Figure 4.5: Zerilli-Armstrong for BCC constitutive model fits (lines) to the experimental flow stress data (data points) for TRIP780 sheet material along transverse direction.

The hardening behavior (for a given strain rate) of AA5182-O was successfully captured by the Zerilli-Armstrong constitutive model for FCC materials. Figure 4.6(a-b) shows the Zerilli-Armstrong for FCC constitutive model fits to the experimental flow stress data for AA5182-O sheet material along transverse direction at 100 and 0.1 s^{-1} strain rate. The R^2 value of the data fits are found to be over 0.98 for the AA5182-O material along all three directions, as shown in Table 4.6, while the upper and lower bound values are found to be within 2% on an average for all the parameters of the model. Unfortunately, similar to the Johnson-Cook constitutive model, this model was also unable to capture the observed transition between negative strain rate sensitivity at low rates and positive strain rate sensitivity at rates above 1 s^{-1} (as shown in Figure 4.6c).

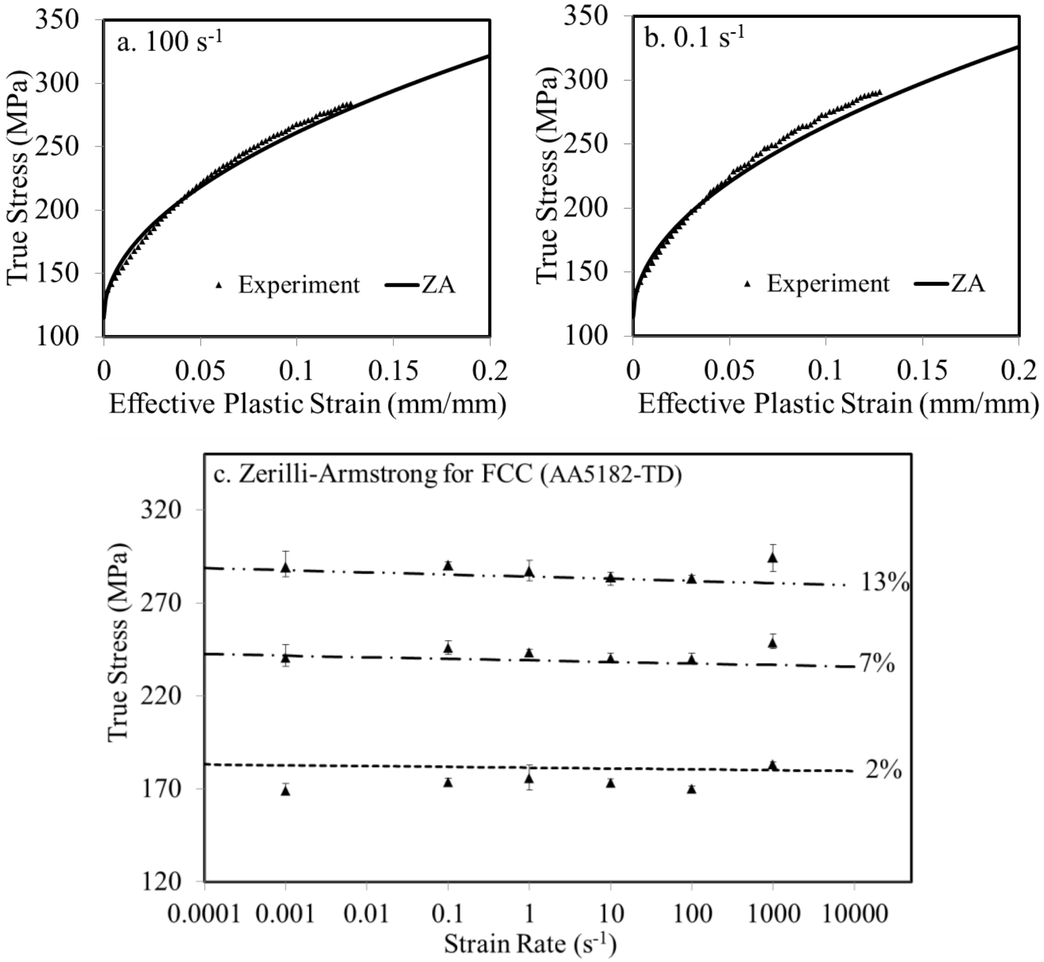

Figure 4.6: Zerilli-Armstrong for FCC constitutive model fits (lines) to the experimental flow stress data (data points) for AA5182-O sheet material along transverse direction at (a) 100 s^{-1} and (b) 0.01 s^{-1} strain rate, and (c) comparison between the tensile strength predicted at different strain rates using the Johnson-Cook model and measured data at 2%, 7%, and 13% strains.

4.3 Voce Constitutive Model Fits

The Voce [11] model (Eq. 4.1) alone is not strain rate sensitive,

$$\sigma_V(\varepsilon_P) = \left[\sigma_{sat} + (\sigma_y - \sigma_{sat})e^{\left(-\frac{\varepsilon_p}{\varepsilon_r}\right)}\right] \qquad \text{Eq. (4.1)}$$

in which σ_{sat} is the saturation stress, σ_y is the initial yield stress, and ε_r is the relaxation strain. Integration of a strain rate dependent term within the Voce hardening law was required to capture the changes in flow stress with respect to strain rate. Since the measured yield stress scales with the strain rate and the strain hardening behavior remains relatively unchanged (Figure 3.1-Figure 3.3), a multiplicative strain rate term was added to the Voce hardening model,

$$\sigma_{Voce\ with\ strain\ rate}(\varepsilon_p, \dot{\varepsilon}) = \sigma_V(\varepsilon_p) \cdot x_{strain\ rate}(\dot{\varepsilon}) \qquad \text{Eq. (4.2)}$$

First, a Johnson-Cook logarithmic type strain rate term (shown in Eq. 4.3) was fit (with Voce) but was only suitable to fit the low (0.001-1 s^{-1}) strain rate data, as shown in Figure 4.7 for DP600 along the transverse sheet orientation. The quality of the fit was similar for the RD and TD tests.

$$x_{Log}(\dot{\varepsilon}) = A\ln(\dot{\varepsilon}) \qquad \text{Eq. (4.3)}$$

in which A is the strain rate parameter.

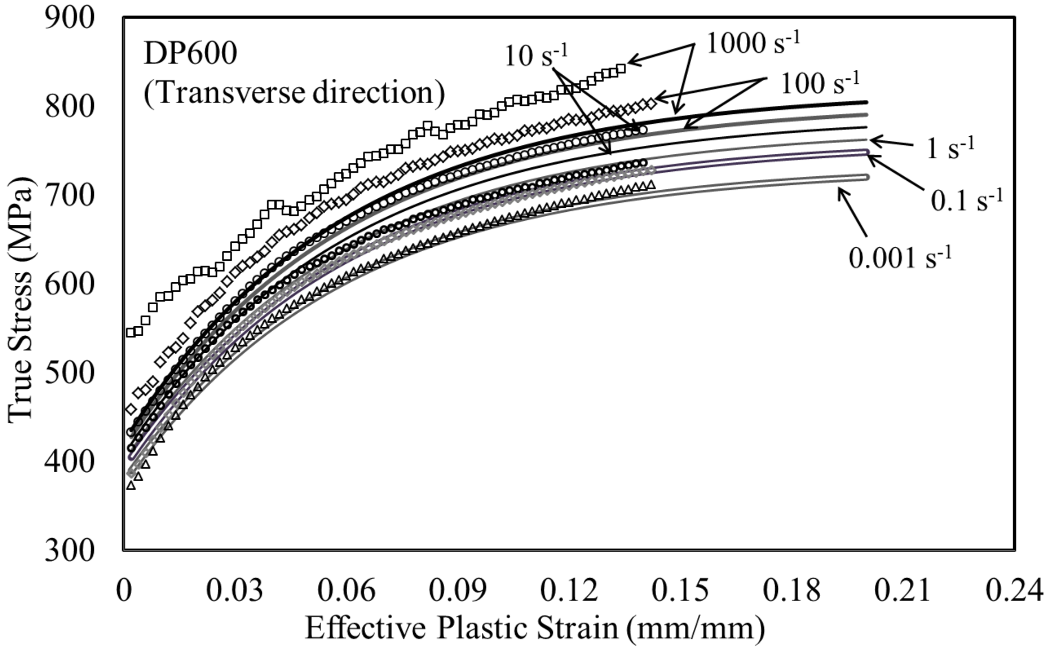

Figure 4.7: Constitutive model fits (lines) to the measured flow stress data along transverse direction (data points) for Voce with a logarithmic-type strain rate function.

The second strain rate term considered was the exponential type (shown in Eq. 4.4) as proposed by Camacho and Ortiz [127], as implemented within a Johnson-Cook model for high strength steel by Børvik et al. [128]. This strain rate term did not capture the measured low (0.001 s^{-1}) strain rate response (shown in Figure 4.8 for DP600 along transverse direction). The quality of the fit was similar for the RD and DD tests.

$$x_{Exponential}(\dot{\varepsilon}) = (1+\dot{\varepsilon})^{B} \qquad \text{Eq. (4.4)}$$

in which B is the strain rate parameter.

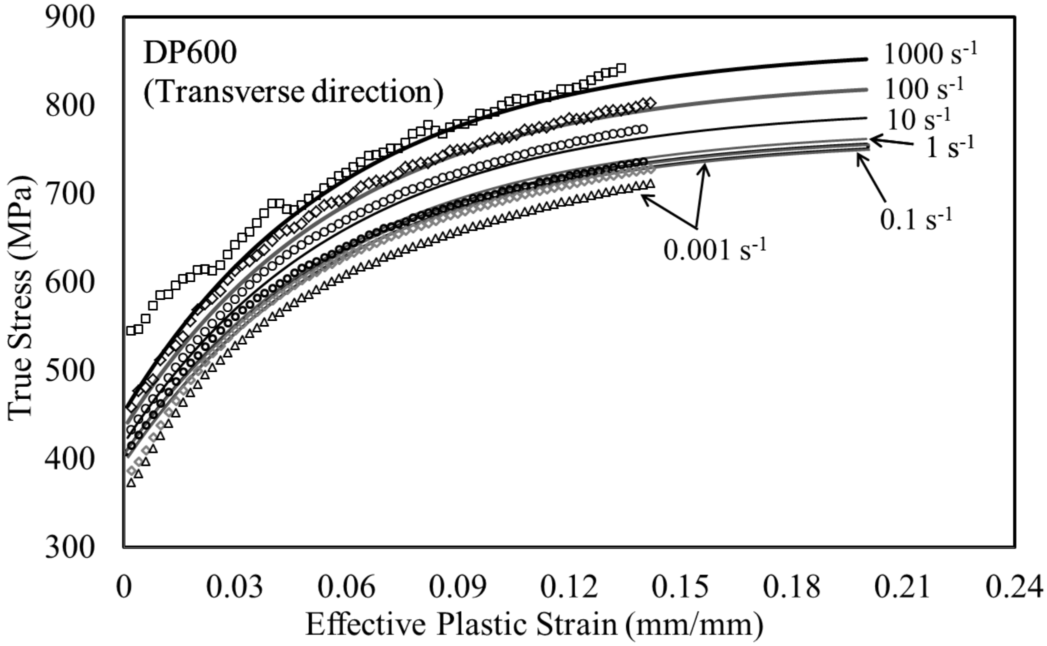

Figure 4.8: Constitutive model fits (lines) to the experimental flow stress data (data points) for Voce with exponential-type strain rate function along transverse direction.

As part of the current research, a combined logarithmic and exponential strain rate term is proposed (Eq. 4.5) and was fit to the data as shown in Figure 4.9-Figure 4.12 for DP600 sheet material along all three orientations. The final rate sensitive Voce model with a combined logarithmic and exponential type strain rate term is shown in Eq. (4.6) and is referred to herein as the Voce-modified (VM) model.

$$x_{Modified}(\dot{\varepsilon}) = [A\ln(\dot{\varepsilon}) + (1+\dot{\varepsilon})^B] \qquad \text{Eq. (4.5)}$$

$$\begin{aligned}\sigma_{VM}(\varepsilon_p, \dot{\varepsilon}) &= \sigma_V(\varepsilon_p)\cdot x_{Modified}(\dot{\varepsilon}) \\ &= \left[\sigma_{sat} + (\sigma_y - \sigma_{sat})e^{-\frac{\varepsilon_p}{\varepsilon_r}}\right][A\ln(\dot{\varepsilon}) + (1+\dot{\varepsilon})^B]\end{aligned} \qquad \text{Eq. (4.6)}$$

where A and B are the strain rate parameters.

The fitted parameters for the VM model can be found in Table 4.7-Table 4.9 for all three sheet materials.

The measured and predicted flow stress curves using the VM model (Figure 4.9-Figure 4.11) exhibit very good agreement. The measured and predicted true stress at three different levels of effective plastic strain are also plotted in Figure 4.12, again showing very good agreement for the range of strain rate considered in the experiments.

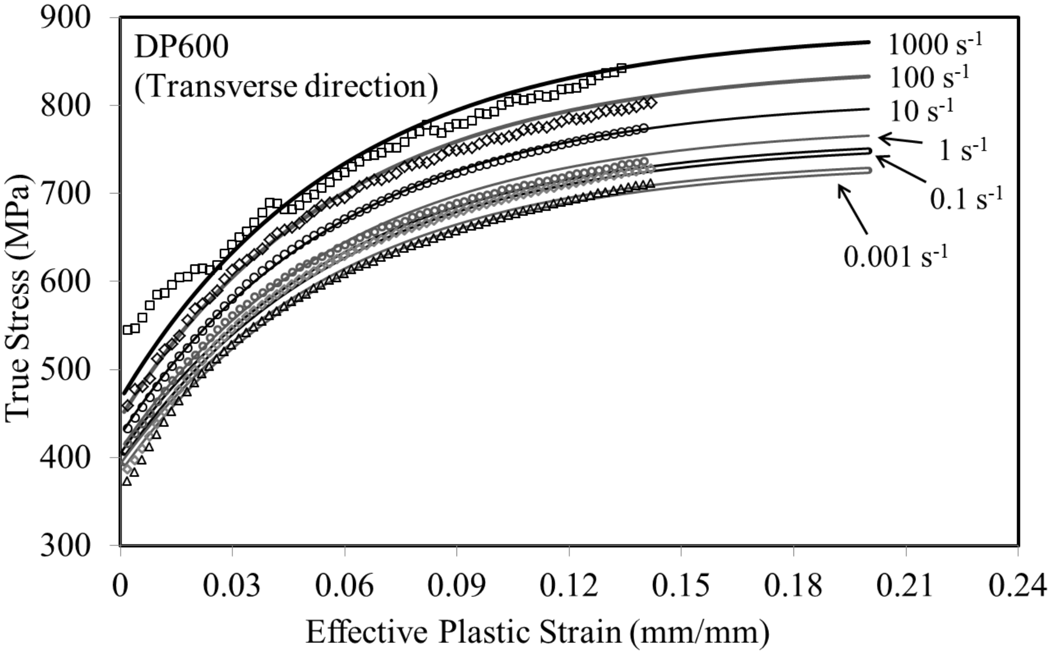

Figure 4.9: Constitutive model fits (lines) to the experimental flow stress data (data points) for Voce-modified function along transverse direction.

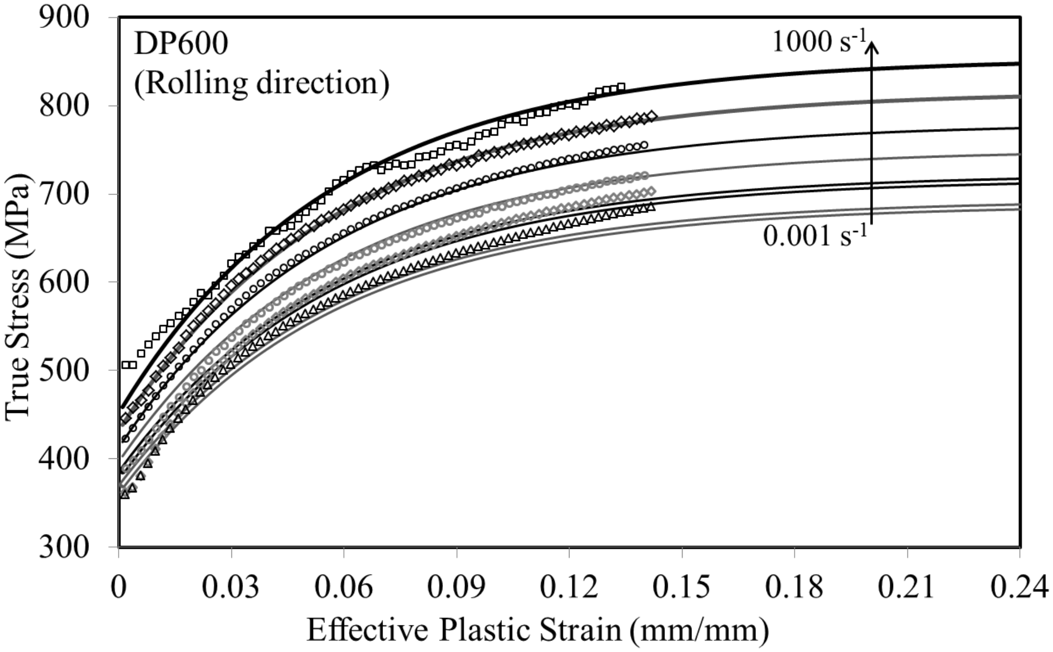

Figure 4.10: Constitutive model fits (lines) to the experimental flow stress data (data points) for Voce-modified function along rolling direction.

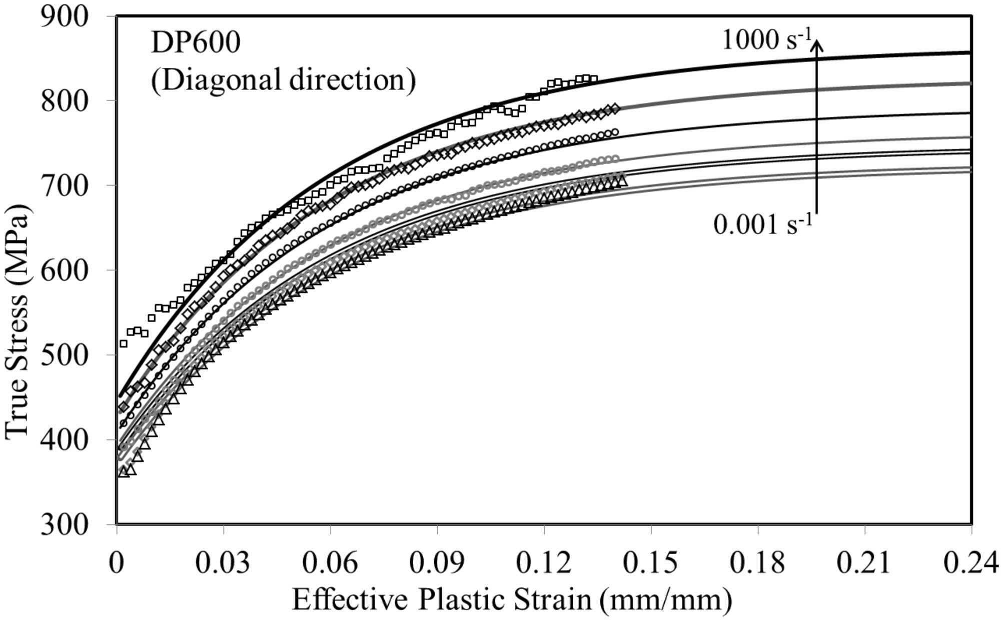

Figure 4.11: Constitutive model fits (lines) to the experimental flow stress data (data points) for Voce-modified function along diagonal direction.

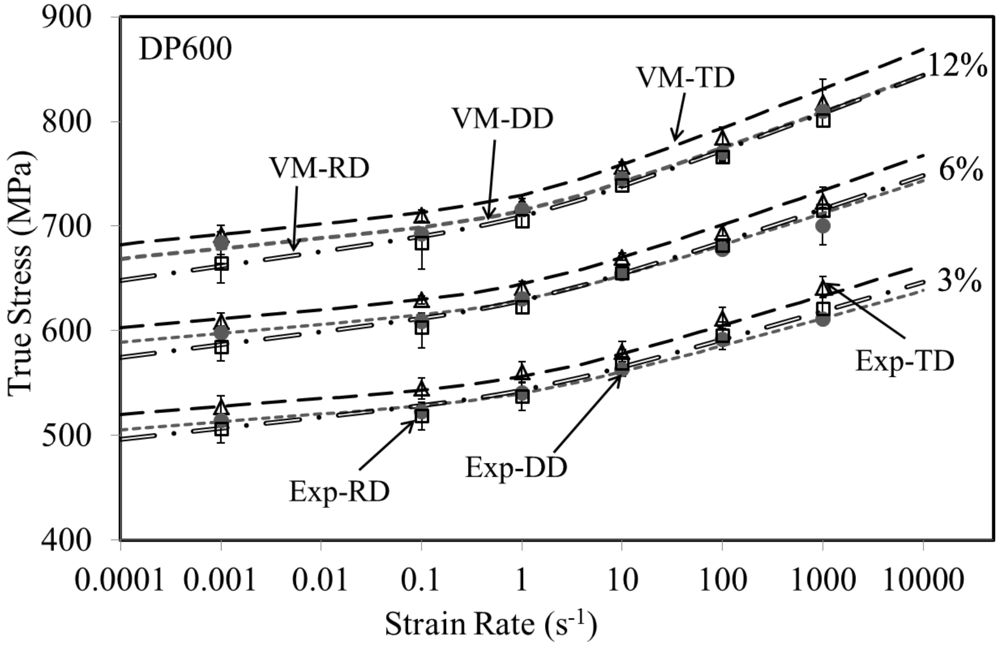

Figure 4.12: Comparison between the tensile strength predicted along different sheet orientations at different strain rates using Voce-modified function and measured data at 3%, 6%, and 12% strains.

The Voce-modified (VM) model was fit (see Table 4.8) to the TRIP780 data with relative success across all strain rates except for the 1,000 s^{-1} tests, which displayed a variation in hardening behavior throughout deformation due to possible changes in the rate of transformation from retained austenite to martensite (as discussed in Section 1.3 and 3.1.2). Figure 4.13-Figure 4.15 shows good agreement for the measured and predicted flow stress curves for all three orientations at strain rate ranging from 0.001 to 100 s^{-1}. The measured and predicted true stress at three different levels of effective plastic strain are also plotted in Figure 4.16, showing very good agreement for the range of strain rate from 0.001 to 100 s^{-1}.

The values for strain rate parameters, A and B, are found to be very close to each other for both DP600 and TRIP780 materials as both materials exhibit moderate strain rate sensitivity. As shown in Table 4.7 and Table 4.8, R^2 value for the non-linear regression fits are found to be approximately 99% for both AHSS materials along all the sheet orientations (again, neglecting the TRIP780 1,000 s^{-1} condition). The upper and lower bound values for a 95% confidence interval are found to be within 2% for the hardening parameters (σ_{sat},σ_y, ε_r), and the values are within 8% for the strain rate parameters (A and B).

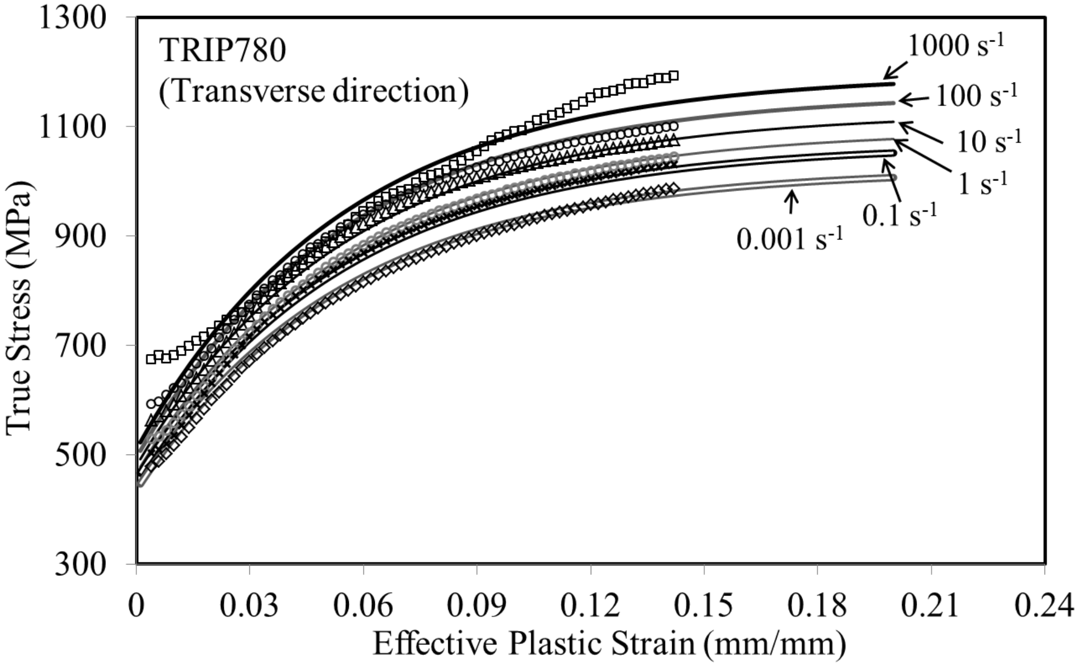

Figure 4.13: Constitutive model fits (lines) to the experimental flow stress data (data points) for Voce-modified function along transverse direction.

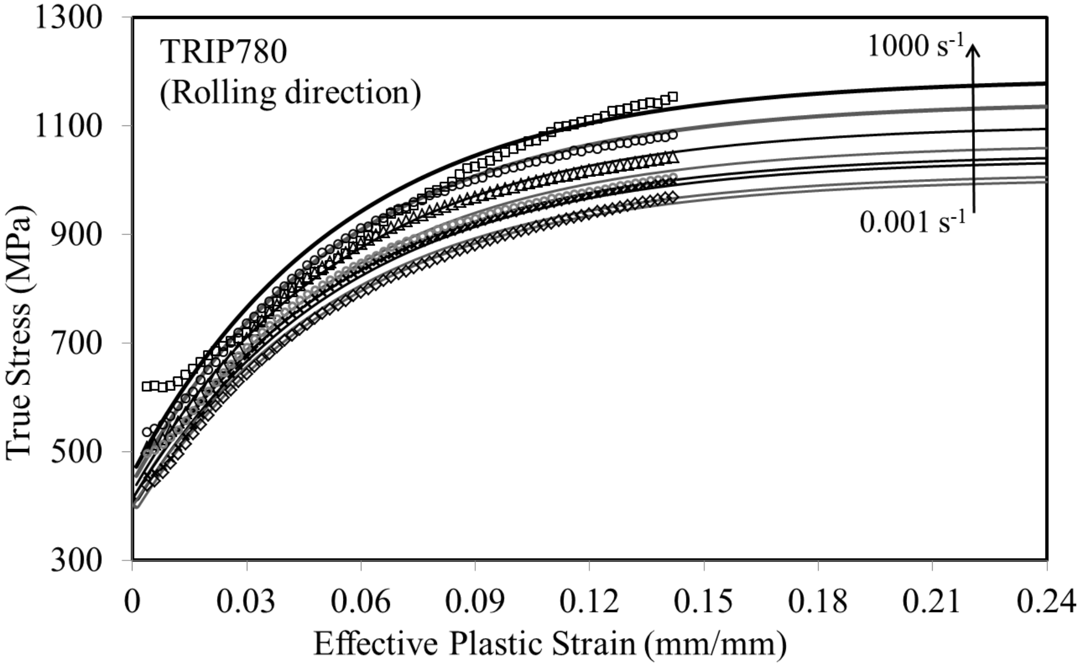

Figure 4.14: Constitutive model fits (lines) to the experimental flow stress data (data points) for Voce-modified function along rolling direction.

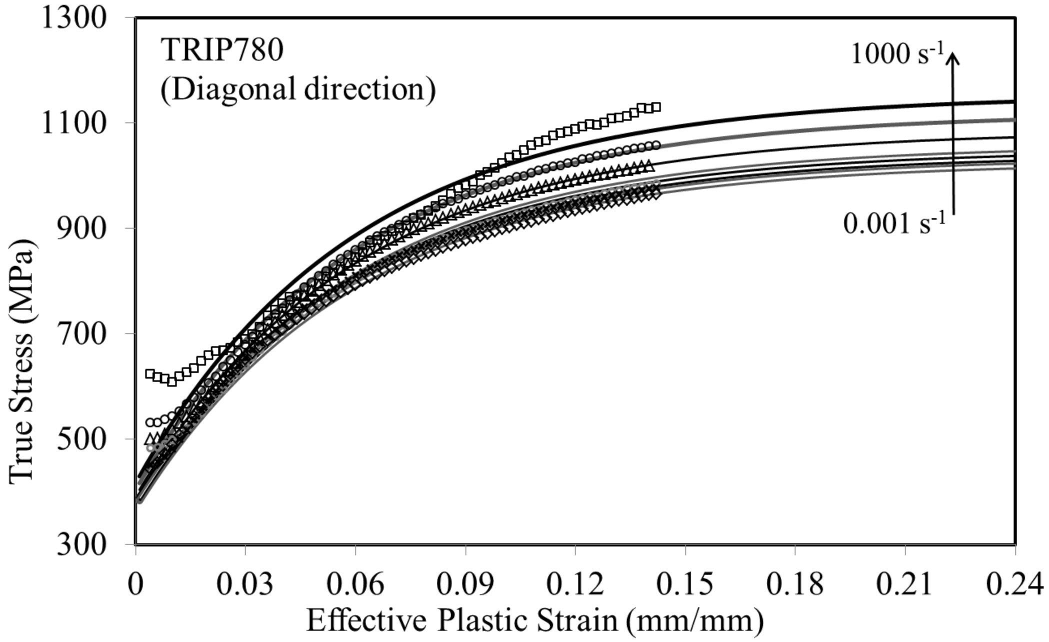

Figure 4.15: Constitutive model fits (lines) to the experimental flow stress data (data points) for Voce-modified function along diagonal direction.

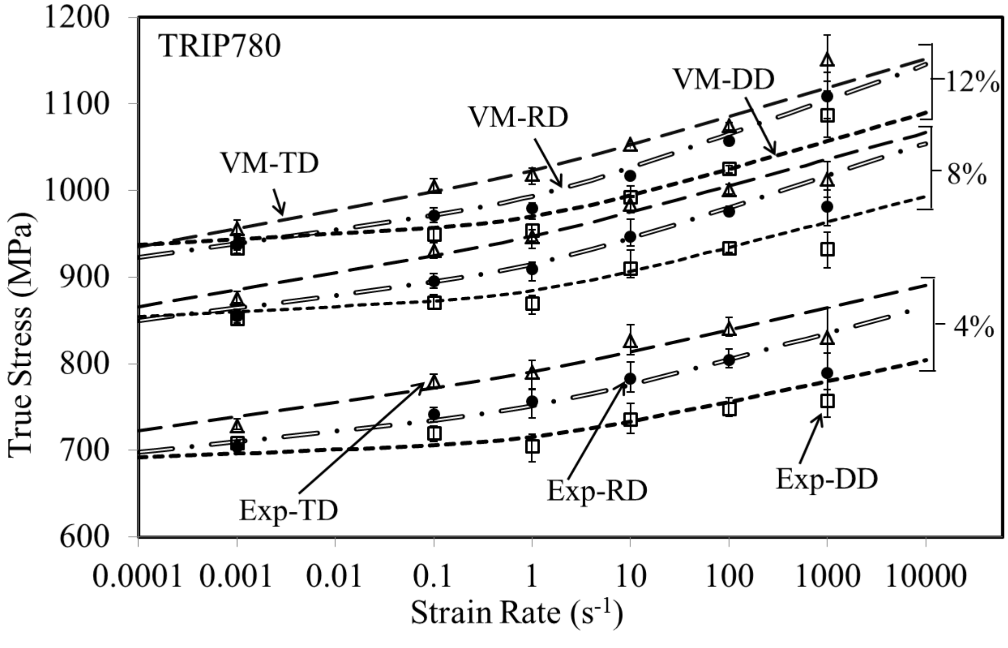

Figure 4.16: Comparison between the tensile strength predicted along different sheet orientations at different strain rates using Voce-modified function and measured data at 4%, 8%, and 12% strains.

The Voce-modified (VM) model was also fit to the AA5182-O data (see Table 4.9) and proved able to capture the negative rate sensitivity of the material at lower strain rates and the transition to positive rate sensitivity above 1 s^{-1}. The results of the measured and predicted AA5182-O data are shown in Figure 4.17(a-f) for the RD tests. The quality of the fit was similar for the DD and TD tests. The transition between negative and positive strain rate sensitivity at three different effective plastic strain levels can be seen in Figure 4.18, which demonstrates good agreement between the measured and predicted data.

The strain rate parameter, A is found to be a negative value for AA5182-O sheet materials, while the strain rate parameter, B is found to be positive. This demonstrates the strain rate effect on flow stress curves is dominated by parameter A at the low (0.001–1 s^{-1}) strain rates, indicating a logarithmic trend in the decrease of stress with respect to the strain rate. The stress recovery for above 1 s^{-1} strain rate was further captured with the exponential type strain rate parameter, B. The R^2 values of the non-linear regression fits are found to be approximately 99% for AA5182-O material along all the sheet orientations.

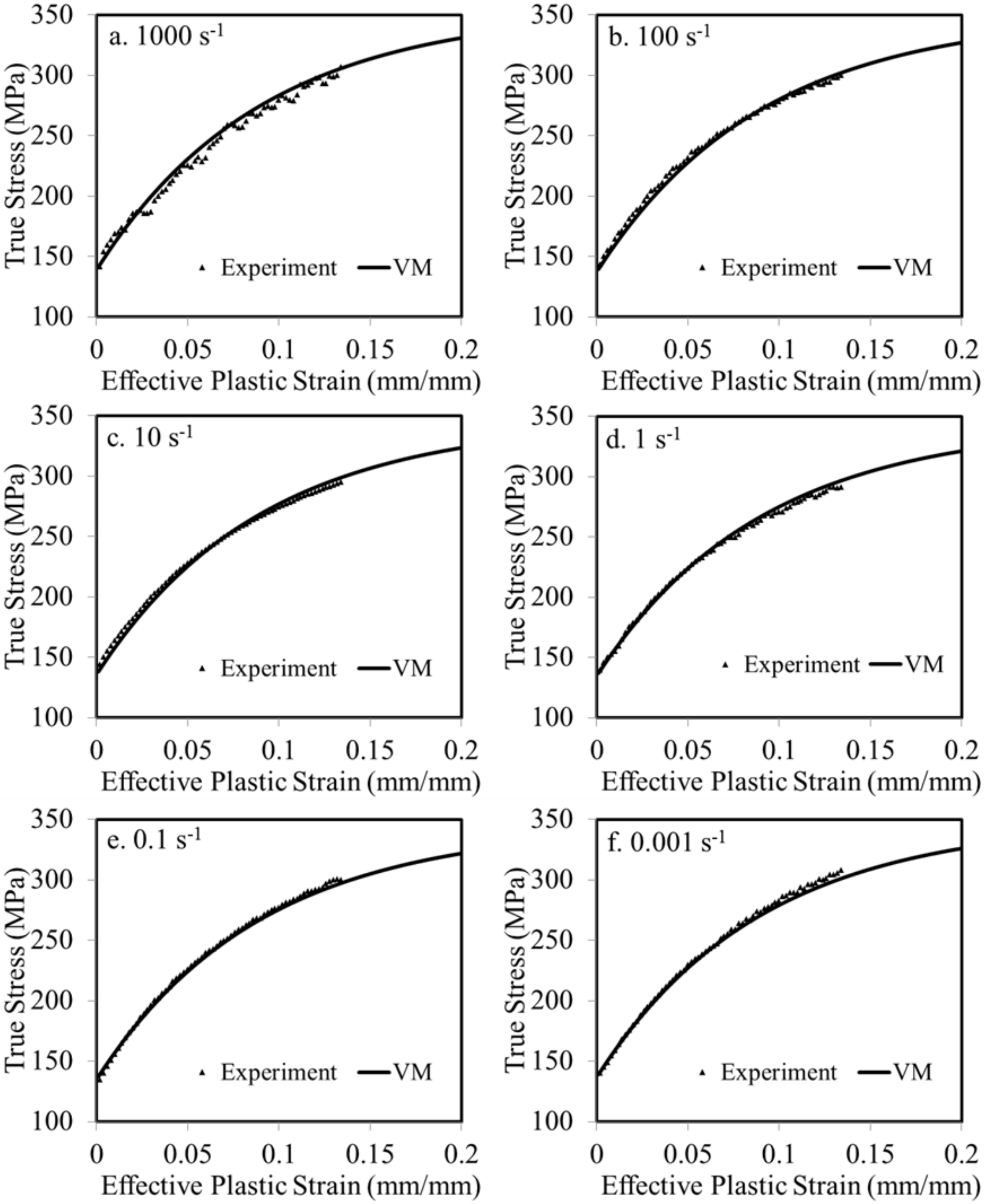

Figure 4.17: Voce – modified model fits (lines) to the experimental flow stress data (data points) for AA5182-O sheet metal along rolling direction at (a) 1000, (b) 100, (c) 10, (d) 1, (e) 0.1, and (f) 0.001 s^{-1} strain rate.

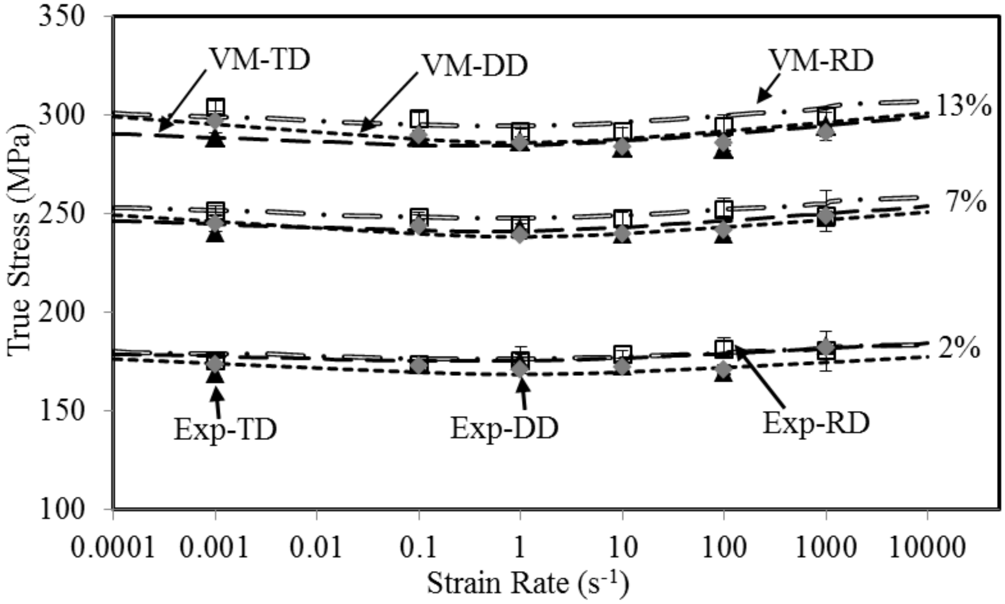

Figure 4.18: Comparison between the tensile strength predicted along different sheet orientations at different strain rates using the Voce-modified function and measured data at 2%, 7%, and 13% strains.

Table 4.7: Constitutive parameters for the DP600 averaged curves fit with the Voce-Modified model.

		σ_{sat}	σ_y	ε_r	A	B	R^2
DP600 (Rolling direction)	Estimate	746	395	0.057	0.0085	0.012	0.993
	95% Lower	741	391	0.055	0.0078	0.011	
	95% Upper	751	398	0.059	0.0092	0.014	
DP600 (Diagonal direction)	Estimate	756	389	0.059	0.006	0.014	0.989
	95% Lower	750	385	0.057	0.0052	0.013	
	95% Upper	762	393	0.061	0.0068	0.015	
DP600 (Transverse direction)	Estimate	770	405	0.059	0.006	0.015	0.989
	95% Lower	764	401	0.057	0.0052	0.014	
	95% Upper	776	409	0.061	0.0068	0.016	

Table 4.8: Constitutive parameters for the TRIP780 averaged curves fit with the Voce-Modified model.

		σ_{sat}	σ_y	ε_r	A	B	R^2
TRIP780 (Rolling direction)	Estimate	1060	410	0.055	0.007	0.01	0.997
	95% Lower	1054	406	0.054	0.0064	0.009	
	95% Upper	1066	414	0.056	0.0076	0.011	
TRIP780 (Diagonal direction)	Estimate	1050	390	0.059	0.005	0.006	0.993
	95% Lower	1041	384	0.056	0.0041	0.004	
	95% Upper	1059	396	0.051	0.0059	0.008	
TRIP780 (Transverse direction)	Estimate	1090	465	0.055	0.009	0.005	0.996
	95% Lower	1085	461	0.054	0.0085	0.004	
	95% Upper	1095	469	0.056	0.0095	0.006	

Table 4.9: Constitutive parameters for the AA5182-O averaged curves fit with the Voce-Modified model.

		σ_{sat}	σ_y	ε_r	A	B	R^2
AA5182-O (Rolling direction)	Estimate	342	134	0.09	-0.003	0.008	0.991
	95% Lower	336	131	0.084	-0.0045	0.005	
	95% Upper	348	137	0.096	-0.0015	0.011	
AA5182-O (Diagonal direction)	Estimate	339	128	0.097	-0.006	0.012	0.993
	95% Lower	336	126	0.094	-0.007	0.011	
	95% Upper	342	129	0.1	-0.005	0.013	
AA5182-O (Transverse direction)	Estimate	335	125	0.09	-0.003	0.01	0.984
	95% Lower	330	123	0.085	-0.004	0.008	
	95% Upper	339	127	0.094	-0.002	0.012	

4.4 Summary

For the materials tested herein, the Johnson-Cook [9] and Zerilli-Armstrong [10] constitutive models were initially fit to the measured flow stress data but were not able to accurately capture the experimental data at the given strain rates. The Zerilli-Armstrong constitutive model was more accurate than Johnson-Cook constitutive model in case of predicting the behavior of DP600 material, while the hardening behavior of TRIP780 material was captured poorly by the Zerilli-Armstrong model. In the case of AA5182-O, both Johnson-Cook and Zerilli-Armstrong models were unable to capture the observed transition between negative strain rate sensitivity at low rates and positive strain rate sensitivity at rates above 1 s^{-1}.

The Voce [11] hardening function was found to more accurately capture the flow stresses along all the metal sheet orientations. A modified strain rate function was added to the Voce hardening law, where the final version of Voce model is referred to as Voce-Modified (VM) model (Eq. (4.6)) was able to predict the experimental data for all three materials at the given strain rate conditions. The one exception to this outcome was the TRIP780 experiments conducted at a strain rate of 1,000 s^{-1}. The 1,000 s^{-1} curve was not captured by the model, but the implementation of a temperature or strain rate dependent phase transformation term could explicitly be added to this strain rate function for improved predictive capability. Development of such a function requires further experimental analysis; therefore, was left for future research. In comparison with Johnson-Cook and Zerilli-Armstrong constitutive models, the VM constitutive model has higher capability in predicting the material behavior presented herein. The higher R^2 values of the non-linear regression of VM model fits for all three materials are also an indication of better accuracy of the curve fits.

CHAPTER 5

NUMERICAL MODELING

A primary objective of this work was to develop rate-dependent constitutive models suitable for metal forming and vehicle crash analysis. As such, it is important to validate the proposed constitutive models in a finite element simulation of the tensile test where the local strains will be higher than the strains used to calibrate the constitutive models. Since large strains will develop within the necked region, the performance of the constitutive model can be assessed by comparison with the predicted and experimental engineering stress-strain responses. In keeping with common practice used in forming and crash simulations, an isotropic, rate-dependent material model is used in the FE simulations using the implicit finite-element code, LS-DYNA [136]. This approach was adopted since brick elements were used to better capture necking onset (as opposed to shell elements) [80] and additional material parameters beyond those measured herein would be required should a three-dimensional anisotropic yield criterion suitable for brick elements be adopted. It is recognized that material anisotropy will not be accounted for in such analyses; however, the goal in these simulations is in validating the predicted rate sensitivity as well as refining the predicted material response beyond necking using the developed constitutive model and fits. It is important to note that damage or fracture models were not considered in the simulations to account for material softening. Detailed damage/fracture characterization of these alloys is left to future work.

5.1 Mesh Analysis

The tensile test geometry was modelled using a half-symmetry assumption and meshed using 8-node, constant stress brick elements. A mesh sensitivity analysis was performed by changing the mesh size within the gauge region from 0.06 to 0.22 mm (Figure 5.1). Since the miniature tensile specimen is only 1.75 mm wide and 1.5 mm thick, small element sizes are required to generate an appropriate mesh. Mesh sensitivity was low for element sizes between 0.06 to 0.22 mm. As shown in Figure 5.2, for DP600 loaded along the RD at a strain rate of 1 s^{-1}, a reasonably fine mesh size of 0.1 mm was found to provide a good balance between computational efficiency and accuracy in the engineering stress-strain response.

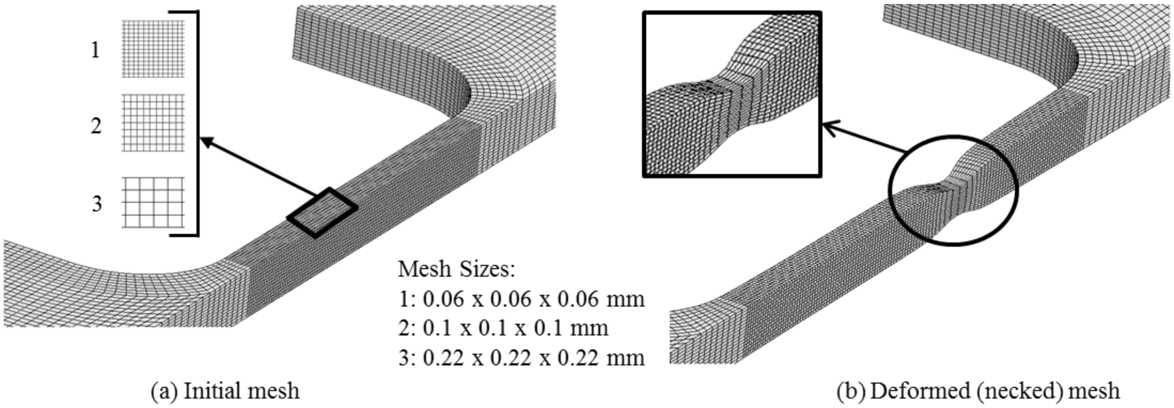

Figure 5.1: Half symmetry (miniature dog-bone) specimen meshing for FEA (a) initial mesh (b) deformed (necked) mesh.

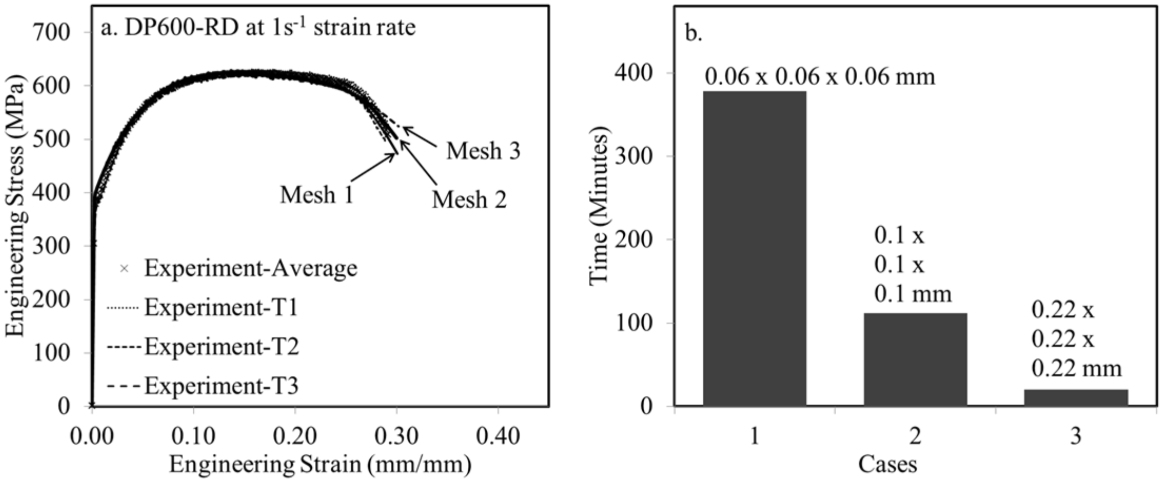

Figure 5.2: (a) Predicted engineering stress-strain curve for DP600 along RD at 1 s^{-1} strain rate with different mesh sizes, (b) CPU time to complete the simulations for different mesh sizes.

5.2 Material Model

The stress-strain curves for different constant nominal strain rates were calculated using the equations for the Voce-modified (VM) models and input as a table in the piecewise linear plasticity material model in LS-DYNA [136]. This method was chosen for simplicity, but it is recognized that the implementation of the VM models within a user defined material model (UMAT) may be more accurate when simulating a wide range of strain rates.

5.3 Results and Validations

Figure 5.3(a-c) compares the engineering stress-strain curves from the simulations to the experimental data for DP600 along the RD at a strain rate of 0.001, 1, and 100 s^{-1}, respectively. As shown in Figure 5.3(a-c), the VM curves provide an accurate prediction of the stress-strain response until the ultimate tensile strength (UTS) is reached, which corresponds to the onset of necking in the experiments. This corresponds to the range of the calibration of the VM constitutive parameters (Section 4.3). However, beyond the UTS, the drop in stress after the onset of necking occurs too rapidly in the model. This accelerated necking response was predicted because of the stress saturation behavior of the VM model which does not accurately capture the post uniform hardening behavior of materials that are capable of achieving high total elongations. It is evident that these materials continue to work harden in the post-uniform regime, delaying the localization process.

The overly soft response of the extrapolated VM model indicates that the DP600 retains some measure of work hardening in the post-uniform regime. Although the VM model will exhibit some rate-hardening due to the strain rate increasing in the neck, the stress saturation term in the model leads to an excessively soft response after necking. It is important to note that the predicted response was too soft even though no damage model was used to account for material softening. Consequently, coupling the current VM extrapolation with a damage model for fracture would result in an even worse agreement with the experiment. Thus, a method is required to refine or better extrapolate the VM model to account for work hardening at higher strains.

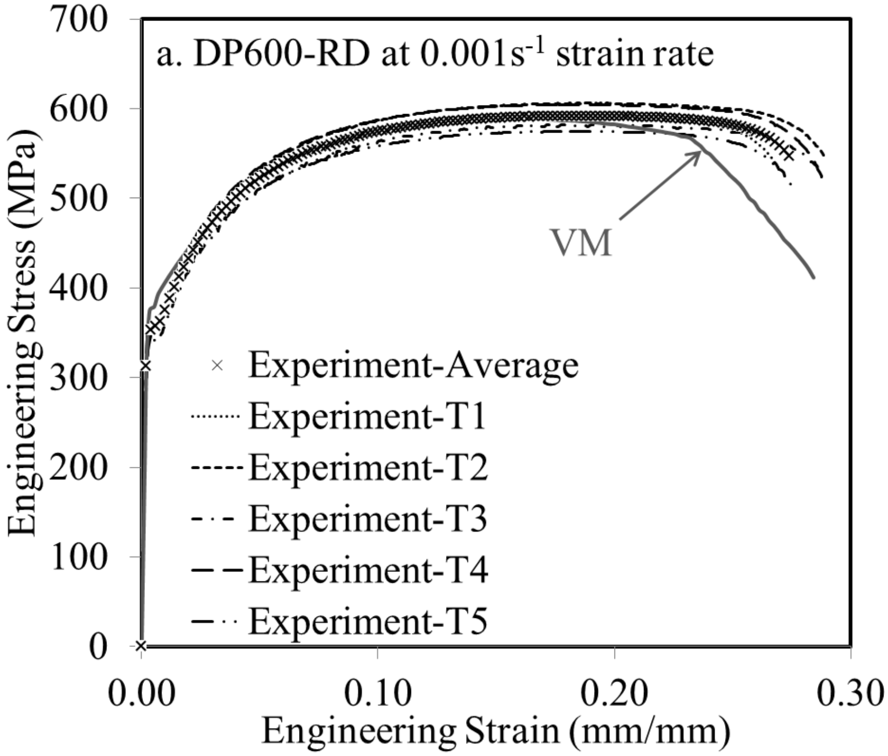
a. DP600-RD at 0.001s-1 strain rate
Engineering Stress (MPa)
Engineering Strain (mm/mm)
700
600
500
400
300
200
100
0
0.00
0.10
0.20
0.30
VM
Experiment-Average
Experiment-T1
Experiment-T2
Experiment-T3
Experiment-T4
Experiment-T5

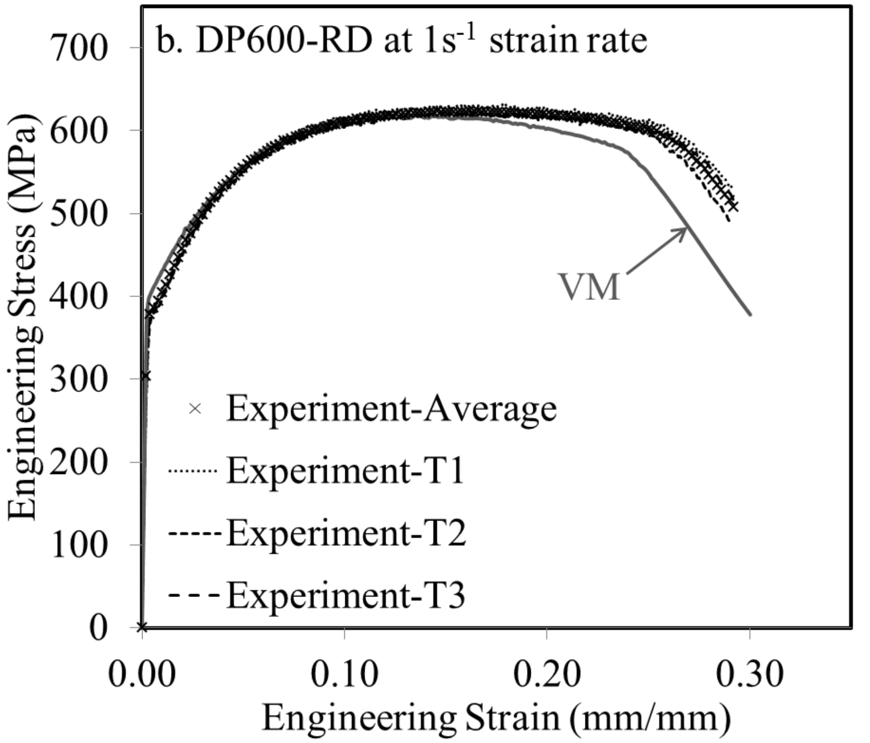
b. DP600-RD at 1s-1 strain rate
Engineering Stress (MPa)
Engineering Strain (mm/mm)
700
600
500
400
300
200
100
0
0.00
0.10
0.20
0.30
VM
Experiment-Average
Experiment-T1
Experiment-T2
Experiment-T3

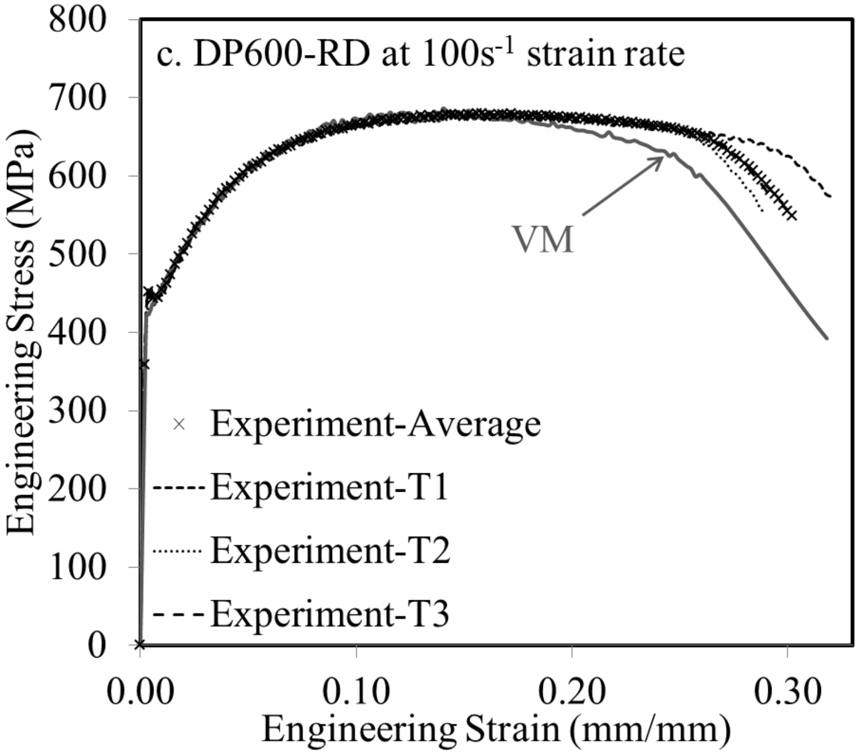

Figure 5.3: Measured and predicted (solid lines) engineering stress vs. strain curves using VM model for DP600-RD at (a) 0.001, (b) 1, and (c) 100 s^{-1} strain rate.

5.3.1 Refinement of VM model

In order to avoid the limitation regarding the saturation-type behavior of Voce hardening law, the Bridgman correction method [137] is often used to determine the flow stress data beyond uniform elongation, which is then manually added to the constitutive model. However, the Bridgman correction method has many limitations as described in [138] including that it is not suited for flat specimens.

Ling [138] proposed a hybrid experimental-numerical method to determine the flow stress curve at large strains for sheet metal specimens by using an extrapolation of the stress-strain curve at the UTS (shown in Eq. (5.1)). The extrapolation function contains a single parameter, w (value between 0 to 1), that was determined iteratively by comparing (matching) the numerical and experimental engineering stress strain curve. This method was used along with the VM model in the present work but it was found that the post uniform hardening behavior using Ling's extrapolation function was overly stiff and overestimated the engineering stress–strain curve, as shown in Figure 5.4 for DP600 in the RD at 1 s^{-1} strain rate.

$$\sigma = \sigma_u \left[w\left(1 + \varepsilon_p - \varepsilon_u\right) + (1 - w)\left(\frac{\varepsilon_p^{\varepsilon_u}}{\varepsilon_u^{\varepsilon_u}}\right)\right] \qquad \text{Eq. (5.1)}$$

where, σ is the true stress, σ_u is the true stress at ultimate tensile strength, ε_p is the effective plastic strain, ε_u is the effective plastic strain at ultimate tensile strength, and w is the weighted function.

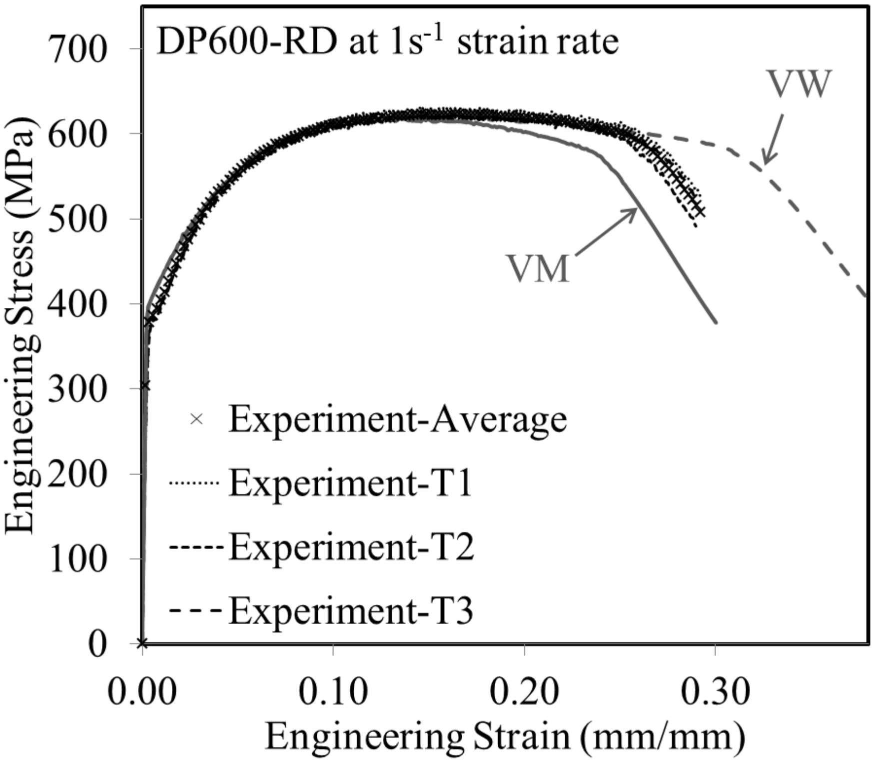

Figure 5.4: Measured and predicted engineering stress vs. strain curves using VM model and VM with Ling's weighted function (referred to as VW) for DP600-RD at 1s^{-1} strain rate.

In order to account for the issue of premature saturation in the Voce model in the post-uniform regime, a linear hardening term, $L(\varepsilon_p)$, can be added to the Voce curve as done by Dunand and Mohr [80]. This method can be incorporated into the VM model of Eq. (4.6) by introducing a general function for the post-uniform hardening, $\beta(\varepsilon_p)$, to yield the modified Voce-Modified-Extrapolated (VME) model as:

$$\sigma_{VM}\left(\varepsilon_p, \dot{\varepsilon}\right) = \sigma_V\left(\varepsilon_p\right) \cdot x_{Modified}(\dot{\varepsilon}) \qquad \text{Eq. (4.6)}$$

$$\sigma_{VME}\left(\varepsilon_p, \dot{\varepsilon}\right) = \left[\sigma_V\left(\varepsilon_p\right) + \beta\left(\varepsilon_p\right)\right] \cdot x_{Modified}(\dot{\varepsilon}) \qquad \text{Eq. (5.2)}$$

where, the linear hardening function $\beta(\varepsilon_p)$ is a function of plastic strain, and was determined from finite element simulations using a manual optimization procedure. In order to avoid numerical issues and discontinuities in the hardening rate when the linear hardening term is introduced, it is proposed that the post-uniform hardening function be composed of a linear hardening function, $L(\varepsilon_p)$, governed by a non-dimensional step function (varies from 0-1), $S(\varepsilon_p)$ with the form:

$$\beta\left(\varepsilon_p\right) = S\left(\varepsilon_p\right) L\left(\varepsilon_p\right) = \left[\frac{1}{1 + e^{\left(C + D\varepsilon_p\right)}}\right]\left(E\varepsilon_p + F\right) \qquad \text{Eq. (5.3)}$$

The complete form of VME model is given as follows:

$$\begin{aligned}\sigma_{VME}\left(\varepsilon_p, \dot{\varepsilon}\right) = \Bigg[&\sigma_{sat} + \left(\sigma_y - \sigma_{sat}\right) e^{-\frac{\varepsilon_p}{\varepsilon_r}} \\ &+ \left[\frac{1}{1 + e^{\left(C + D\varepsilon_p\right)}}\right]\left(E\varepsilon_p + F\right)\Bigg]\left[A \ln(\dot{\varepsilon}) + (1 + \dot{\varepsilon})^B\right]\end{aligned} \qquad \text{Eq. (5.4)}$$

The novelty of this approach is that the parameters determined in the VM model using the experimental data remain unchanged while the post-uniform hardening parameters (shown in Table 5.1) can be fit from the finite-element (FE) simulations of the experiments to create a hybrid experimental-numerical function for the flow stress curve.

Table 5.1:
The VM and VME constitutive model parameters for each material and each orientation.

	σ_{sat}	σ_y	ε_r	C	D	E	F	A	B	R-square
DP600-RD	746	395	0.057	2.5	-15	190	-20	0.009	0.013	0.992
DP600-DD	756	389	0.059	2.5	-15	190	-20	0.006	0.014	0.989
DP600-TD	770	405	0.059	2.5	-15	190	-20	0.006	0.015	0.989
TRIP780-RD	1060	410	0.055	1.93	-9	0.5	3	0.007	0.010	0.996
TRIP780-DD	1050	380	0.059	1.93	-9	0.5	3	0.003	0.011	0.993
TRIP780-TD	1090	465	0.055	1.93	-9	0.5	3	0.009	0.005	0.996
AA5182-RD	342	134	0.09	3	-10	40	3	-0.003	0.008	0.992
AA5182-DD	339	128	0.097	3	-10	40	3	-0.006	0.012	0.994
AA5182-TD	328	136	0.090	3	-10	40	3	-0.003	0.009	0.985

The linear, step, and combined step–linear functions are plotted as function of strain in Figure 5.5a for DP600 (RD) at a strain rate of 1s^{-1}. The post uniform hardening behavior predicted by the VME model is continuous and free of any discontinuities at the transition point where uniform deformation ends and post uniform deformation begins, see Figure 5.5b. The continuity of VME model was further evaluated by plotting the derivative of the flow stress curve (hardening rate) against the plastic strain. The hardening rate is found to be continuous with no inflection points or oscillations (as shown in Figure 5.5c for DP600RD at 1 s^{-1}).

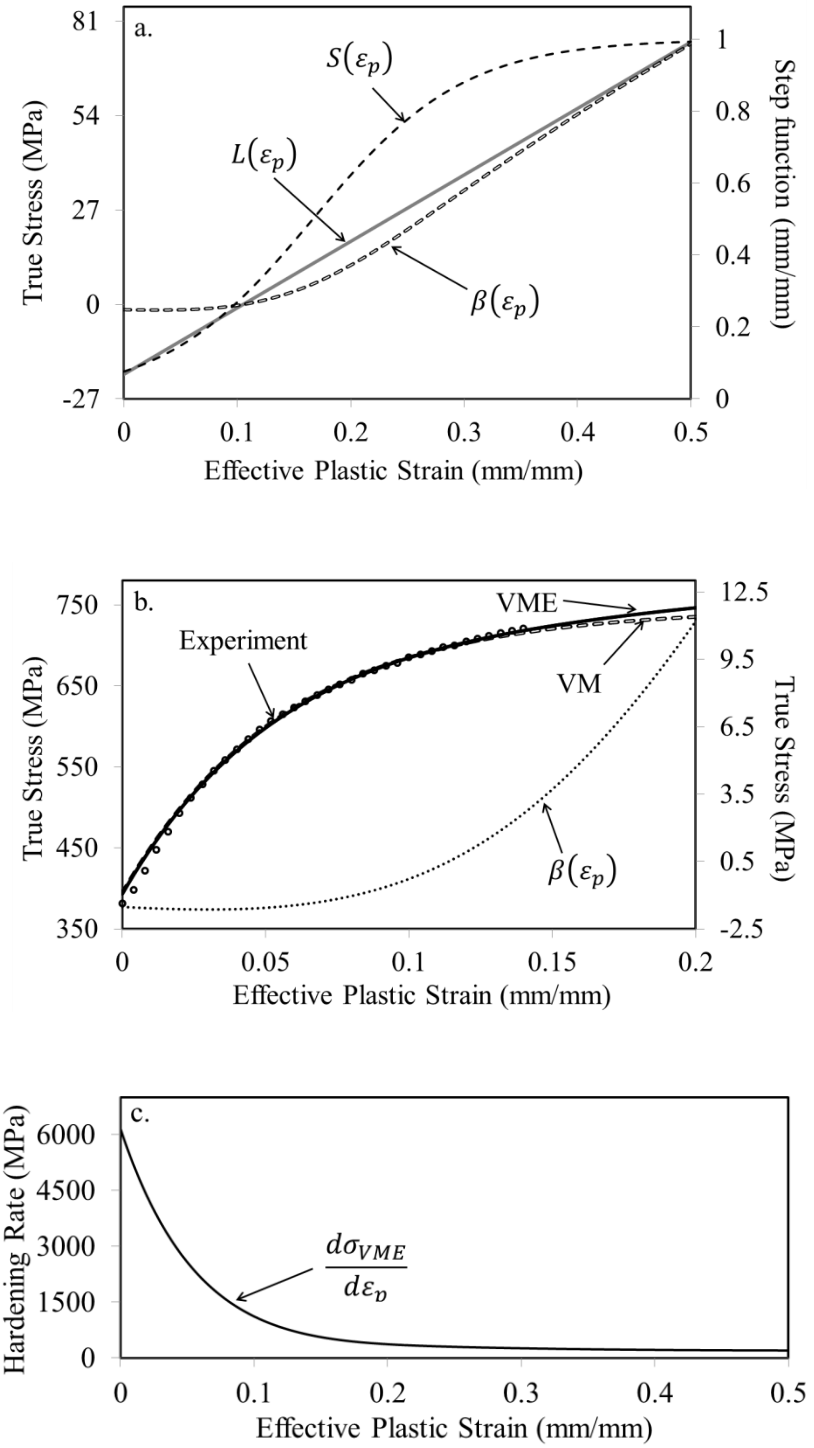

Figure 5.5: (a) Step, linear, and combined step-linear function plotted individually against the effective plastic strain, (b) Comparison between the data predicted through VM and VME and (c) Hardening rate of VME model against the effective plastic strain for DP600RD at 1s^{-1} strain rate.

For larger strain, the post uniform hardening behavior predicted using the VM and VME models is shown in Figure 5.6d, Figure 5.7d, and Figure 5.8d for DP600 along RD, TRIP780 along TD, and AA5182-O along DD, respectively. For the TRIP780 material, both the VM and VME models predict saturation in flow stress after uniform elongation completes, while the VME model predicts a noticeably more positive hardening behavior than the VM model for the DP600 and AA5182-O materials. The VME constitutive model (Eq. (5.4)) was implemented within the FE framework and used to simulate the tensile tests for all of the materials and conditions tested in this work. The predicted engineering stress vs. strain curves for DP600 (RD) are shown at three different strain rates in Figure 5.6(a-c). The stress-strain curves predicted using the VME model show good agreement at all three strain rates. Although not shown, the model performs equally well for the DD and TD directions.

Similar FE simulations were performed for the TRIP780 and AA5182-O alloys. VM and VME models generated nearly identical flow stress curves for the TRIP780 material as shown in Figure 5.7d. As a result, when both models were implemented to model the tensile tests and reproduce the engineering stress vs. strain, there was no noticeable difference as shown in Figure 5.7(a-c).

Consequently, predicted stress-strain curves from VM model for AA5182-O alloys was found close to the experimental data point for strain rates ranging from 0.1 to 10 s^{-1}; however, the VME stress-strain curves are found to be more accurate for all strain rates due to the additional calibration parameters. Figure 5.8(a-c) shows the measured and predicted engineering stress vs. strain curves for AA5182-O along the DD at various strain rates.

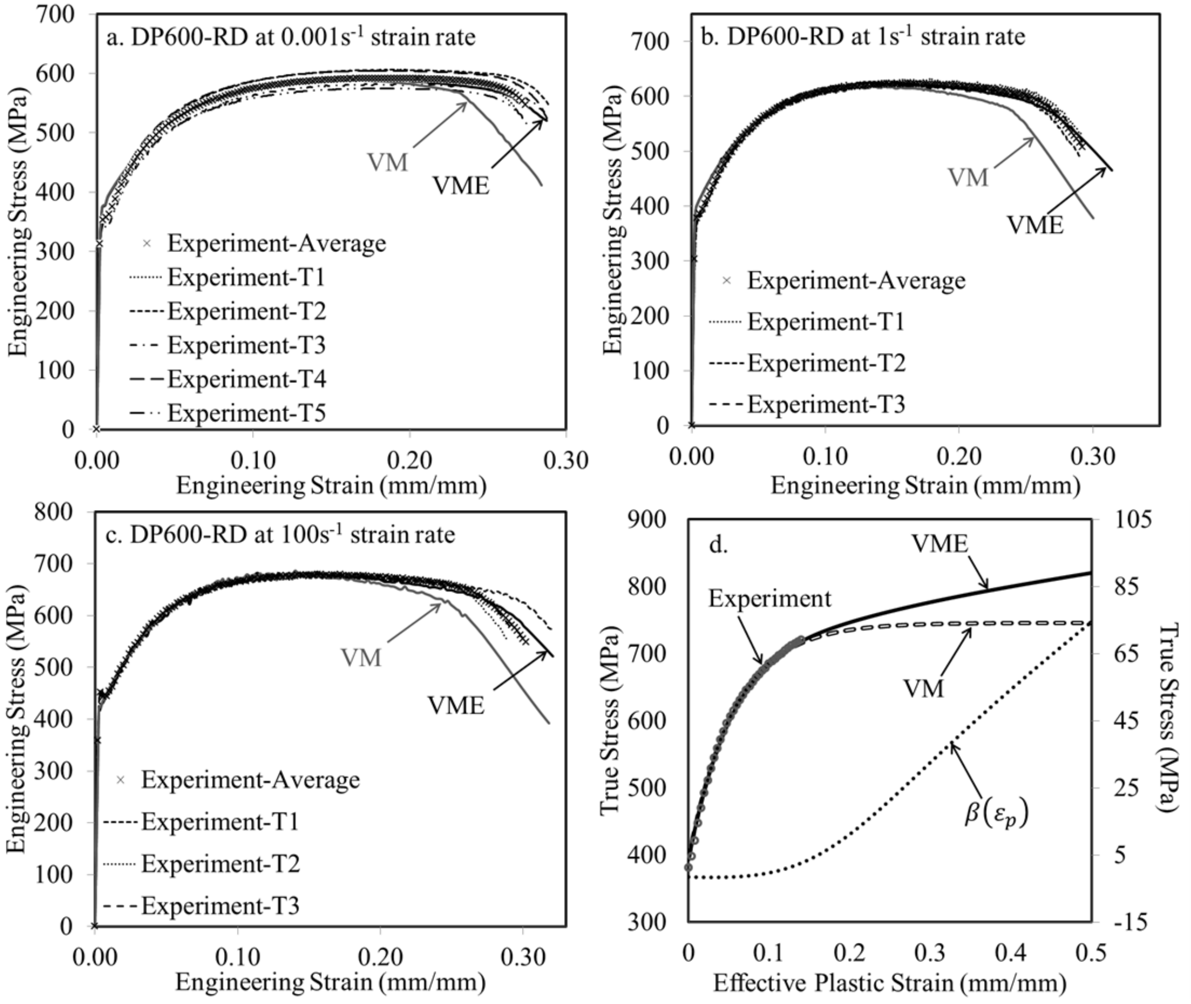

Figure 5.6: Measured and predicted (solid lines) engineering stress vs. strain curves for DP600-RD at (a) 0.001, (b) 1, and (c) 100 s^{-1} strain rate, and (d) flow stress curves including post uniform elongation at 1 s^{-1} strain , and stresses calculated using $\beta(\varepsilon_p)$ – combined step-linear function (plotted on secondary axis) against the effective plastic strain. VM denotes the Voce – Modified model and VME denotes the Voce – Modified – Extrapolated model.

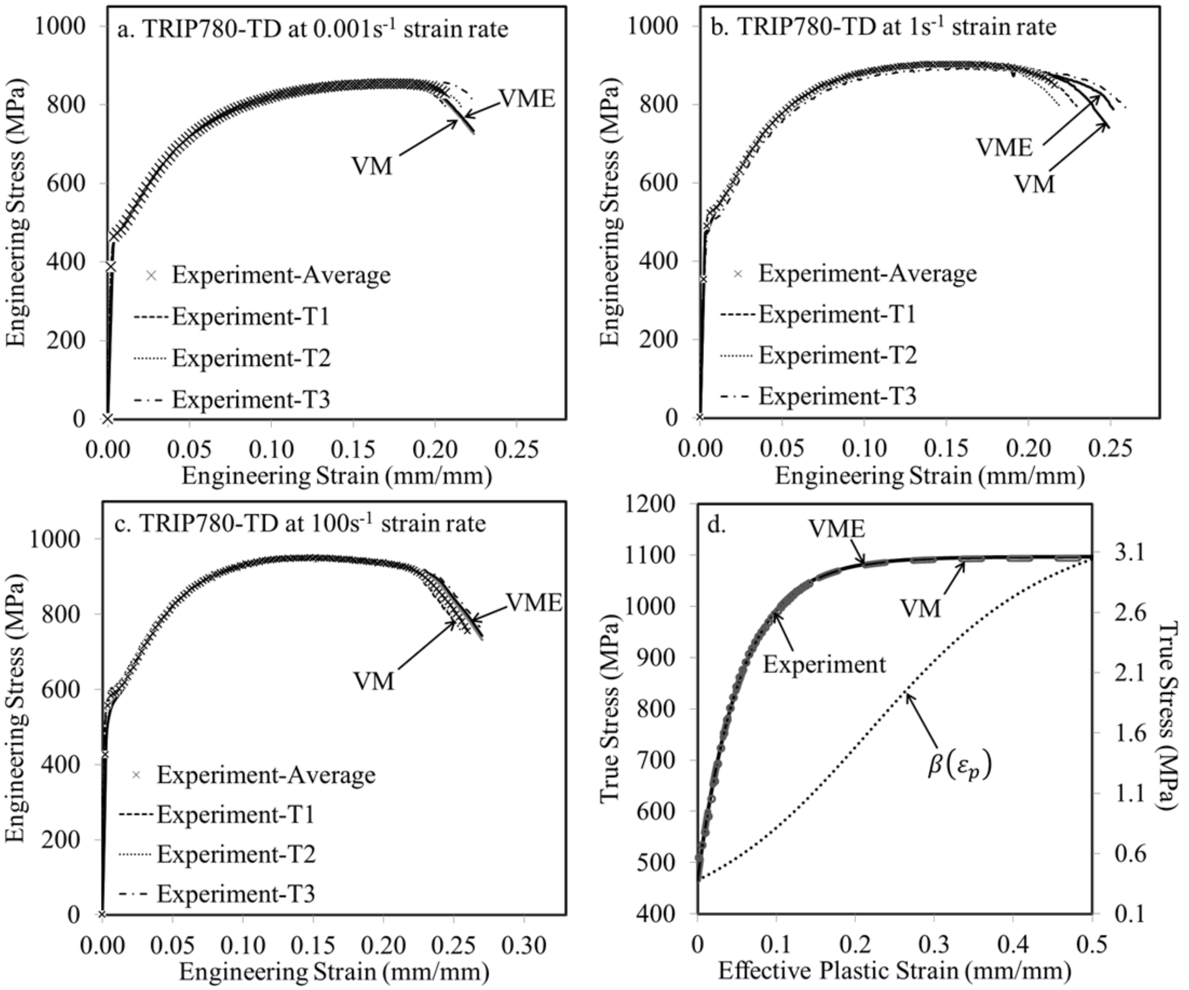

Figure 5.7: Measured and predicted (solid lines) engineering stress vs. strain curves for TRIP780-TD at (a) 0.001, (b) 1, and (c) 100 s^{-1} strain rate, and (d) flow stress curves including post uniform elongation for TRIP780-TD at 1 s^{-1} strain rate, and stresses calculated using $\beta(\varepsilon_p)$ – combined step-linear function (plotted on secondary axis) against the effective plastic strain. VM denotes the Voce – Modified model and VME denotes the Voce – Modified – Extrapolated model.

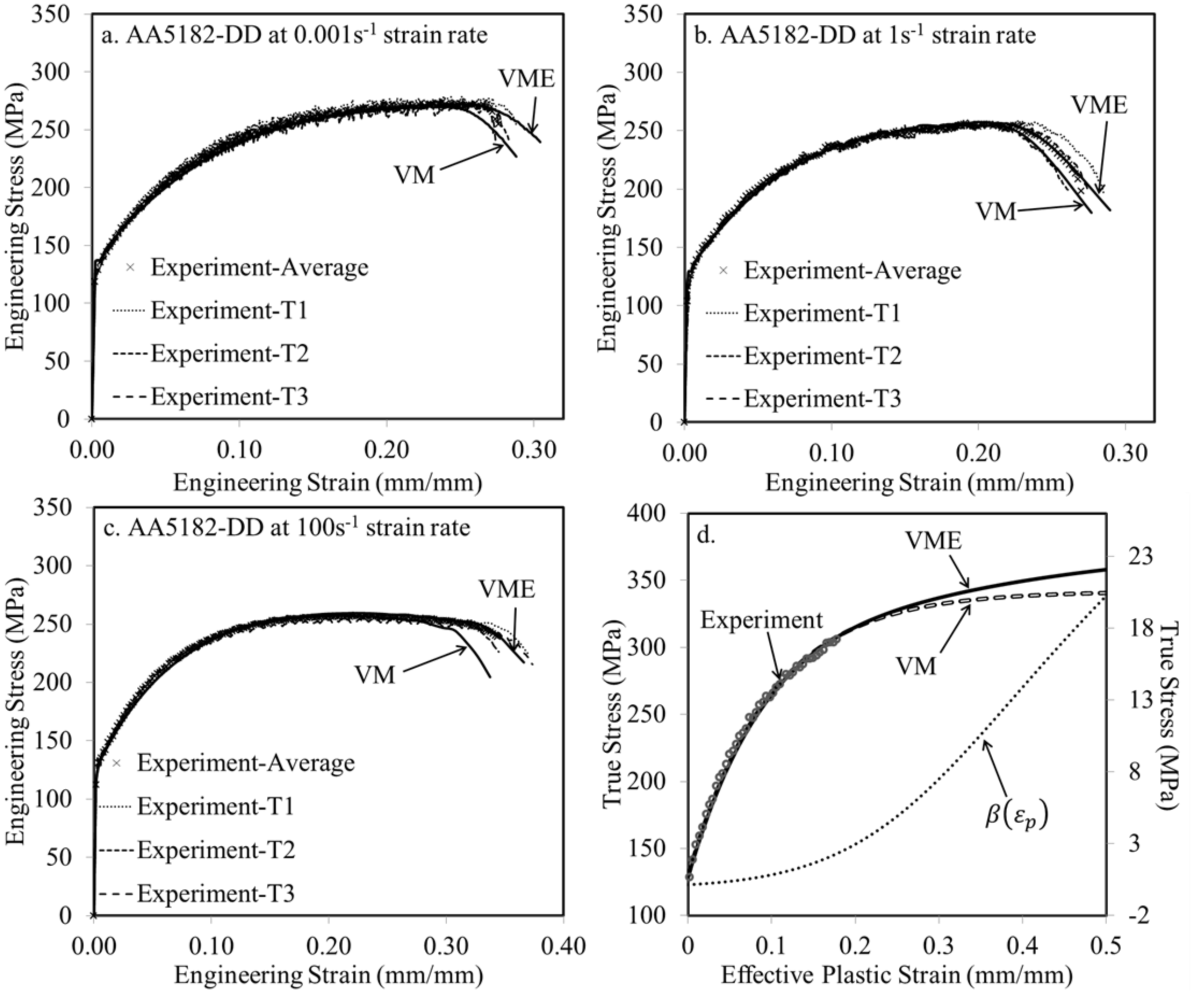

Figure 5.8: Measured and predicted (solid lines) engineering stress vs. strain curves for AA5182-0-DD at (a) 0.001, (b) 1, and (c) 100 s^{-1} strain rate, and (d) flow stress curves including post uniform elongation for AA5182-DD at 1 s^{-1} strain rate, and stresses calculated using $\beta(\varepsilon_p)$ – combined step-linear function (plotted on secondary axis) against the effective plastic strain. VM denotes the Voce – Modified model and VME denotes the Voce–Modified –Extrapolated model.

A secondary validation of the VM and VME models is conducted since the performance of the models was only evaluated using a global metric, the engineering stress-strain curve. In particular, the VME model was optimized using this global response and thus a secondary, local measurement should be considered to validate the model. Since deformation becomes concentrated within the necked region, the geometry of the neck at fracture was selected as a secondary validation of the constitutive models. For each material, the area at the minimum cross section of the tensile sample was measured using an optical microscope and compared with the value from the FE model at the displacement-to-failure. The area measurement is used instead of the thickness or width because the material is assumed to be isotropic and these measurements will change with the r–value but the area at fracture should be similar. The experimental values for the area reduction at fracture for each material are compared with the numerical values from the constitutive models for DP600-RD, TRIP780-TD, and AA5182-O-DD at 0.29, 0.24, and 0.27 engineering strain, respectively for 1 s^{-1} strain rate condition (shown in Figure 5.9). Note that the model does not account for material damage; hence, the predictions of reduction in area simply correspond to the deformation state at the measured elongation corresponding to fracture in the experiments (rather than a prediction of ductility, for example).

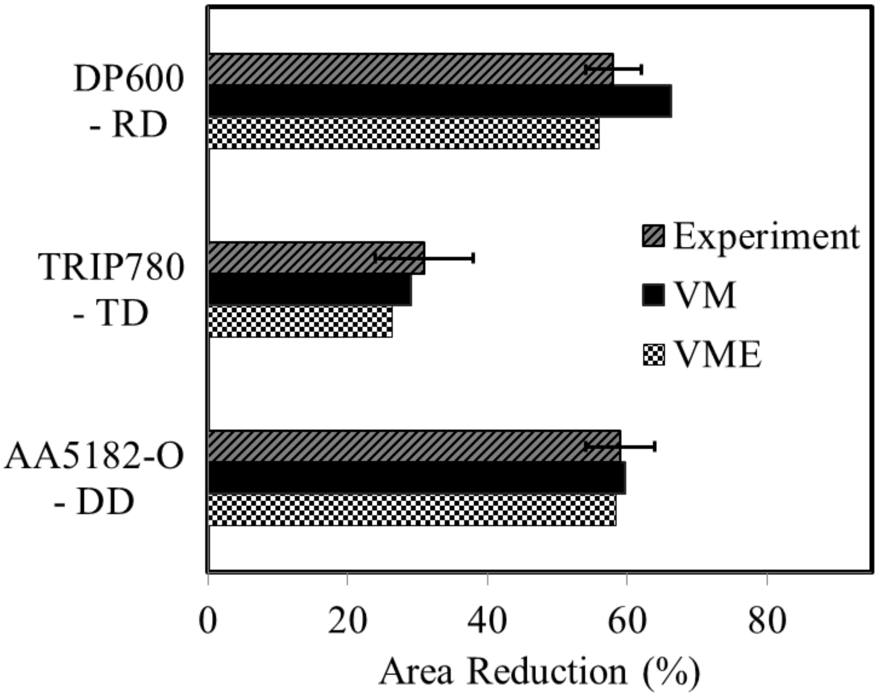

Figure 5.9: Comparison between the experimental values for the area reduction (%) at fracture and the numerical values from constitutive models for all three materials at 29%, 24%, and 27% elongation strain for DP600-RD, TRIP780-TD, and AA5182-O-DD, respectively at 1 s^{-1} strain rate. The error bars indicate the standard deviations calculated using the measured values from the population of repeat tests.

The VM model, which provided an overly soft global response for DP600 (shown in Figure 5.3 and Figure 5.6), overestimates deformation within the neck. The VME model is in good agreement with the measured engineering stress-strain data (Figure 5.6) but slightly underestimates the area reduction. A finite element analysis including a damage treatment could result in better prediction of material softening with improvement in the performance of the VME model for DP600. However, in typical metal forming or crashworthiness simulations which rely upon forming limit or fracture limit curves, material softening is generally not considered and the VME model should provide an accurate estimation of the hardening behavior for DP600 sheet material. Although, both the VM and VME models are in very good agreement with the global response for the TRIP780 material (Figure 5.7), both models are found to slightly under predict the area reduction values, although both predictions fall within the experimental error. In the case of AA5182-O, both the VM and VME models agree well with the measured data.

CHAPTER 6

6.1 Discussion

For DP600, an increase in strength with increasing strain rate was observed for all three sheet orientations. The yield stress scaled upwards with increasing strain rate and the shape of the flow stress curve (or the hardening behavior) remained consistent for all of the strain rates. The highest strength is observed along the transverse direction, while the stress along diagonal and rolling directions is found to be similar.

TRIP780 exhibits an increase in strength with strain rate over the range 0.001 to 100 s^{-1}. At 1000 s^{-1}, the initial hardening behavior was quite different, as seen by a drop in stress to below that at 100 s^{-1} over a strain range of 0.03 to 0.08, indicating a lower initial strain hardening rate. Beyond a strain of 0.08, the hardening rate recovers and the stress increases to above that at 100 s^{-1}. Wei et al. [54] reported similar behavior for Si-Mn TRIP-aided steel in the range from 950 to 1300 s^{-1}. Wei et al. [54] and Slycken et al. [36] have attributed such behavior of TRIP steels to the decrease in the volume fraction of martensite transformed from retained austenite due to the adiabatic heat rise generated at the higher (>1000 s^{-1}) strain rate. The highest strength is observed along the transverse sheet orientation while the strength along the diagonal direction of the sheet metal was observed to be the lowest at all rates of strain.

AA5182-O appears to be mildly rate sensitive in the range of strain rates considered. The yield strength is found to be largely rate-insensitive. At higher strains (7 and 13%), AA5182-O exhibited a mild negative rate sensitivity over the strain rate range from 0.001–1 s^{-1}, while at higher rates a mild positive strain rate sensitivity was observed. Similar hardening behavior and rate sensitivity was observed for all three sheet orientations. The drop in flow stress between 0.001 to 1 s^{-1} is found to be approximately 5-7 MPa and 10-12 MPa at 7% and 13% logarithmic strain, respectively, while a similar level of stress was recovered as the strain rate increased from 1 to 1000 s^{-1}. The data measured in this work closely agreed with the experimental data presented by Smerd [19] at quasi-static and high strain rates. Similar to the current work, negative strain rate sensitivity has also been observed for room temperature tensile testing of AA5182 at quasi-static strain rates ranging from 10^{-6}-1 s^{-1} by Lademo et al. [57], and for strain rates ranging from 7.05×10^{-6}–0.1 s^{-1} by Abbadi et al. [58], and Picu et al. [59]. Higashi et al. [55] also reported similar negative strain rate sensitivity of annealed AA5182 materials at room temperature for strain rates below 10^{2} s^{-1}. The observed negative strain rate sensitivity in the AA5182-O samples was attributed to the PLC effect [58-64]. Serrated flow and different types of PLC serrations were observed over the measured strain rates ranging from 0.001-1 s^{-1}, while no serrations were observed at 10 s^{-1}. PLC band nucleation and propagation were observed up to a strain rate of 1 s^{-1}, whereas the strain distribution along the gauge length remained uniform prior to necking at 10 s^{-1}, confirming the absence of a PLC effect beyond 1 s^{-1}. The band speed showed a slight decrease during strain while the band velocity increased with an increase in strain rate.

None of the materials tested exhibited definitive trends with respect to dependency of anisotropy, measured in terms of flow stress and r–value variation with material direction, on strain rate. The measured r-values were greatest for the diagonal and transverse sheet orientations for the DP600 and TRIP780, respectively, with the lowest r–value being measured for the RD for both steels. Filho et al. [76], Panda et al. [78], and Nasser et al. [79] also reported the lowest r–value for DP600 and TRIP780 alloys along the RD. The average r–values (across all strain rates) for DP600 along the RD, DD and TD orientations are 0.79, 0.90 and 0.98, respectively, while the average r–values for TRIP780 along the RD, DD and TD orientations are 0.52, 0.81 and 0.64, respectively. These values agreed well with quasi-static data presented by Panda et al. [78] and Nasser et al. [79] for DP600 and TRIP780, respectively. AA5182-O exhibited a minimal variation in r–value with respect to sheet orientation with an average r–value equal to 0.7. Similar r–values are reported by Butuc et al. [81] for AA5182 at quasi-static rates.

The Johnson-Cook [9] and Zerilli-Armstrong [10] constitutive models were fit to the measured flow stress data but were not able to accurately capture the experimental data over the range of strain rates tested. However, the Zerilli-Armstrong BCC constitutive model was more accurate than the Johnson-Cook model in the case of predicting the behavior of DP600. In case of AA5182-O, both the Johnson-Cook and Zerilli-Armstrong models were unable to capture the observed transition between negative strain rate sensitivity at low rates and positive strain rate sensitivity at rates above 1 s^{-1}. The Voce [11] hardening function was found to more accurately capture the flow stresses along all the metal sheet orientations. A modified (combined logarithmic and exponential) strain rate function was added to the Voce hardening law, referred to herein as the Voce-Modified (VM) model. The VM model was able to predict the experimental data for all three materials along all the three sheet orientations at the given strain rate conditions. The one exception to this outcome was the TRIP780 experiments conducted at a strain rate of 1,000 s^{-1}. The 1,000 s^{-1} curve was not captured by the model, but the implementation of a temperature or strain rate dependent phase transformation term may account for the observed behavior.

Numerical simulations were performed to validate the developed model. The VM model provided an overly soft global response for DP600; thus, overestimated deformation within the neck due to the saturation-type behavior of Voce hardening law. In order to account for the issue of premature saturation in the Voce model in the post-uniform regime, the VM model was further refined by adding a hardening term that is activated after UTS. The modified VM model was referred to as Voce-Modified-Extrapolated (VME) model. The VME model was found to be in good agreement with the measured engineering stress-strain data but slightly underestimated the area reduction. A finite element analysis including a damage treatment could result in better prediction of material softening with improvement in the performance of the VME model.

The experimental and numerical investigations carried out in this work have provided insight into the behavior of DP600, TRIP780 and AA5182 sheet metal alloys for strain rates ranging from 0.001 to 1000 s^{-1}. A similar approach could be employed in conjunction with dynamic experiments at different temperatures to capture thermal softening effects.

6.2 Conclusions

i. The DP600 sheet tested in this work exhibits positive strain rate sensitivity over the entire range of strain rates along all three sheet orientations. An increase in strain rate from 0.001 to 100 s^{-1} led to an average increase of 85 MPa in engineering stress (at 0.10 engineering strain) for all three sheet orientations.

ii. For an increase in strain rate from 0.001 to 100 s^{-1}, the TRIP780 sheet exhibited a corresponding increase in engineering stress (at 0.10 engineering strain) of approximately 110 MPa for all three sheet orientations. At 1,000 s^{-1}, the TRIP780 exhibited a delay in hardening until approximately 0.08 effective plastic strain, after which the hardening rate recovers. This behavior is thought to be due to a delay in the TRIP reaction associated with adiabatic heating at the higher strain rate [36,52,54].

iii. AA5182-O exhibits slightly negative strain rate sensitivity at room temperature over the range of strain rate 0.001–1 s^{-1}, whereas mildly positive rate sensitivity was observed for strain rates above 1 s^{-1}. This transition corresponds to the strain rate above which PLC band activity is suppressed.

iv. None of the alloys tested exhibited a systematic dependence of anisotropy, characterized in terms of the variation in material strength and r–value with respect to material direction, on strain rate.

v. The Voce–Modified (VM) model, which introduces both logarithmic and exponential strain rate sensitivity terms, was able to capture the strain rate dependence of all three materials (along all three material directions) up to the end of uniform elongation. The one exception to this outcome was the TRIP780 experiments conducted at a strain rate of 1000 s^{-1}, as discussed in conclusion ii.

vi. The Voce-Modified-Extrapolated (VME) model was calibrated to capture the measured post uniform engineering stress-strain behavior for all three materials, with reasonable predictions of area reduction at the measured elongation at fracture.

6.3 Future Work

The work presented in the thesis has provided important insight into the behavior of DP600, TRIP780 and AA5182 at strain rates similar to those experienced in forming and automotive crash scenarios. In order to build upon the results presented here and gain a better understanding of the mechanical behavior of these sheet metal alloys at high strain rates, the following work should be pursued in the future:

i. Uniaxial tensile tests should be performed at elevated temperatures and strain rates to characterize the thermal softening of these materials.

ii. The effect of strain rate on the TRIP mechanism should be characterized for the TRIP780 sheet material since this may account for the anomalous response measured at 1000 s^{-1}

iii. Integration of thermal softening into the proposed constitutive models should be undertaken.

iv. Metallographic examination of the damage and fracture mechanisms of these specimens should be performed as a first step in development of models to predict fracture.

v. Expanding ring or in-plane shear experiments should be conducted at strain rates exceeding those in the current study (on the order of 10^4 s^{-1}) in order to gain an understanding of the behavior of these materials within the ultra-high strain rate regime.

REFERENCES

[1] C.M. Tamarelli, *AHSS 101: The evolving use of Advanced High-Strength Steels for Automotive Applications*, In Advanced High-Strength Steel (AHSS) Research, Steel Market Development Institute, May 2012. Retrieved June 18, 2014, from: http://www.autosteel.org/~/media/Files/Autosteel/Research/AHSS/AHSS%20101%20-%20The%20Evolving%20Use%20of%20Advanced%20High-Strength%20Steels%20for%20Automotive%20Applications%20-%20lr.pdf.

[2] W.S. Miller, L. Zhuang, J. Bottema, A.J. Witterbrood, P. De Smet, A. Haszler, and A. Vieregge, *Recent development in aluminum alloys for the automotive industry*, Material Science and Engineering A., Vol. 2080, Issue 1, pp. 37 – 49, March 2000.

[3] C. Salisbury, M. Worswick, and R. Mayer, *High rate constitutive modeling of aluminum alloy tube*, Journal de Physique (France) IV, Vol. 134, Issue 1, pp. 43-48, July 2006.

[4] J. Kim, D. Kim, H.N. Han, F. Barlat, and M.G. Lee, *Strain rate dependent tensile behavior of advanced high strength steels: Experiment and constitutive modeling,* Material Science and Engineering: A, Vol. 559, pp. 222-231, January 2013.

[5] R. Smerd, S. Winkler, C. Salisbury, M.J. Worswick, D. Lloyd, and M. Finn, *High strain rate tensile testing of automotive aluminum alloy sheet, International Journal of Impact Engineering*, Vol. 32, Issues 1-4, pp. 541-560, December 2005.

[6] A.C. Thompson, *High Strain Rate Characterization of Advanced High Strength Steels, Master's thesis*, University of Waterloo, Waterloo, Canada, 2006. http://hdl.handle.net/10012/2831.

[7] H. Yu, Y. Guo, and X. Lai, *Rate-dependent behavior and constitutive model of DP600 steel at strain rate from* 10^{-4} *to* 10^{3} s^{-1}, Materials and Design, Vol. 30, Issue 7, pp. 2501-2505, August 2009.

[8] G.C. Ramos, M. Stout, R.E. Bolmaro, J.W. Signorelli, and P. Turner, *Study of a drawing-quality sheet steel. I: Stress/strain behaviors and Lankford coefficients by experiments and micromechanical simulations*, International Journal of Solids and Structures, Vol. 47, Issue 17, pp. 2285-2293, August 2010.

[9] G.R. Johnson and W.H. Cook, *A constitutive model and data for metals subjected to large strains, high strain-rates and high temperatures*, Proceeding of 7th International Symposium on Ballistics, pp. 541-547, 1983.

[10] F.J. Zerilli and R.W. Armstrong, *Dislocation-mechanics-based constitutive relations for material dynamics calculations*, Journal of Applied Physics, Vol. 61, Issue 5, pp. 1816-25,

1987.

[11] E. Voce, *The relationship between stress and strain for homogeneous deformation,* J I Met, Vol. 74, Issue 11, pp. 537-62, 1948.

[12] Z. He, J. Ma, H. Wang, G.E.B. Tan, D. Shu, J. Zheng, *Dynamic fracture behavior of layered alumina ceramics characterized by a split Hopkinson bar*, Material Letters, Vol. 59, Issue 8-9, pp. 901-904, April 2005.

[13] S. Dong, Y. Wang, Y. Xia, *A finite element analysis for using Brazilian disk in split Hopkinson pressure bar to investigate dynamic fracture behavior of brittle polymer materials*, Polymer Testing, Vol. 25, Issue 7, pp. 943-952, October 2006.

[14] Q.M. Li, H. Meng, *About the dynamic strength enhancement of concrete-like materials in a split Hopkinson pressure bar test, International Journal of Solids and Structures*, Vol. 40, Issue 2, pp. 343-360, January 2003.

[15] C.V. Sligtenhorst, D.S. Cronin, G.W. Brodland, *High strain rate compressive properties of bovine muscle tissue determined using a split Hopkinson bar apparatus*, Journal of Biomechanics, Vol. 39, Issue 10, pp. 1852-1858, 2006.

[16] M.A. Meyers, Dynamic behavior of materials, New York: Wiley; 1994.

[17] J.D. Campbell, W.G. Ferguson, *The temperature and strain-rate dependence of the shear strength of mild steel,* Philosophical Magazine, Vol. 21, Issue 169, pp. 63-82, 1970.

[18] B.L. Boyce, M.F. Dilmore, *The dynamic tensile behavior of tough, ultrahigh-strength steels at strain-rates from 0.0002* s^{-1} *to 200* s^{-1}, International Journal of Impact Engineering, Vol. 36, Issue 2, pp. 263-271, February 2009.

[19] R.O. Smerd, *Constitutive behavior of aluminum alloy sheet at high strain rates*, Master's thesis, University of Waterloo, 2005.

[20] J. Weertman, T. Vreeland Jr., K.M. Jassby, *Dislocation Mechanics at High Strain Rates*, In: Metallurgical Effects at High Strain Rates, R.W. Rohde, B.M. Butcher, J.R. Holland, C.H. Karnes (Ed.), pp. 319-333, Plenum Press, New York, 1973.

[21] P.S. Follansbee, J. Weertman*, On the question of flow stress at high strain rates controlled by dislocation viscous flow*, Mechanics of Materials, Vol. 1, Issue 4, pp. 345-350, December 1982.

[22] U.S. Lindholm, *Dynamic Deformation of Metals*, In: Behavior of Materials Under Dynamic Loading, N.J. Huffington, pp. 42-61, ASME, 1965.

[23] U.S. Lindholm, L.M. Yeakley, A. Nagy, *The dynamic strength and fracture properties of dresser basalt,* International Journal of Rock Mechanics and Mining Sciences & Geomechanics Abstracts, Vol. 11, Issue 5, pp. 181-191, May 1974.

[24] W.J. Nam, C.M. Bae, *Microstructural evolution and its relation to mechanical properties in a drawn dual-phase steel*, Journal of Materials Science, Vol. 34, Issue 22, pp. 5661-5668, November 1999.

[25] S.J. Barnard, G.D.W. Smith, M. Sarikaya, G. Thomas, *Carbon atom distribution in a dual phase steel: An atom probe study*, Scripta Metallurgica, Vol. 15, Issue 4, pp. 384-392, April 1981.

[26] D.K. Mondal, R.M. Dey, *Effect of grain size on the microstructure and mechanical properties of a C-Mn-V dual-phase steel*, Materials Science and Engineering: A, Vol. 149, Issue 2, pp. 173-181, January 1992.

[27] G.S Huppi, D.K. Matlock, G. Krauss, *An evaluation of the importance of epitaxial ferrite in dual-phase steel microstructures*, Scripta Metallurgica, Vol. 14, Issue 11, pp. 1239-1243, August 1980.

[28] R.O. Rocha, T.M.F. Melo, E.V. Pereloma, D.B. Santos, *Microstructural evolution at the initial stages of continuous annealing of cold rolled dual-phase steel*, Materials Science and Engineering: A, Vol. 391, Issue 1-2, pp. 296-304, January 2005.

[29] U. Liedl, S. Traint, E.A. Werner, *An unexpected feature of the stress-strain diagram of dual-phase steel*, Computational Materials Science, Vol. 25, Issue 1-2, pp. 122-128, September 2002.

[30] M. Erdogan, R. Priestner, *Effect of epitaxial ferrite on yielding and plastic flow in dual phase steel in tension and compression*, Materials Science and Technology, Vol. 15, Issue 11, pp. 1273-1284, November 1999.

[31] M. Sarwar and R. Priestner, *Influence of ferrite-martensite microstructural morphology on tensile properties of dual-phase steel*, Journal of Materials Science, Vol. 31, Issue 8, pp. 2091-2095, April 1996.

[32] W.R. Cribb and M. Rigsbee, Structure and Properties of Dual-Phase Steels, A.T. Davenport (Ed.), Warrendale, Pennsylvania, 1979.

[33] S. Curtze, V.-T. Kuokkala, M. Hokka, P. Peura, *Deformation behavior of TRIP and DP steels in tension at different temperatures over a wide range of strain rates*, Material Science and Engineering: A, Vol. 507, Issue 1-2, pp. 124-131, May 2009.

[34] N.D. Beynon, S. Oliver, T.B. Jones and G. Fourlaris, *Tensile and work hardening properties of low carbon dual phase strip steels at high strain rates*, Materials Science and Technology, Vol. 21, Issue 7, pp. 771-778, January 2005.

[35] W. Dabboussi, High strain rate behavior of multiphase transformation induced plasticity

(TRIP) steels, PhD thesis, McGill University, Montreal, Canada, February 2009.

[36] J. Van Slycken, P. Verleysen, J. Degrieck, J. Bouquerel, and B.C. De Cooman, *Dynamic response of aluminum containing TRIP steel and its constituent phases,* Materials Science and Engineering: A, Vol. 460-461, pp. 516-524, July 2007.

[37] P.J. Jacques, E. Girault, T. Catlin, N. Geerlofs, T. Kop, S. Van Der Zwaag, S. and F. Delannay, *Bainite transformation of low carbon Mn-Si TRIP-assisted multiphase steels: Influence of silicon content on cementite precipitation and austenite retention,* Materials Science and Engineering A, Vol. 273-275, pp. 475-479, December 1999.

[38] M. Xia, Z. Tian, L. Zhao, Y.N. Zhou, *Metallurgical and Mechanical Properties of Fusion Zones of TRIP Steels in Laser Welding*, ISIJ International, Vol. 48, Issue 4, pp. 483-488, January 2008.

[39] B. Engl, U. Heidmann, and W. Müschenborn, *Cold Formability and Light Weight Construction – Driving forces for recent steel development*, Modern LC and ULC Sheet Steels for Cold Forming: Processing and Properties, International Symposium, Department of Ferrous Metallurgy, RWTH Aachen University of Technology, Vol. 1, pp. 39-50, 1998.

[40] A. Pichler and P. Stiaszny, *TRIP steel with reduced silicon content,* Steel Research, Vol. 70, Issue 11, pp. 459–465, 1999.

[41] G.B. Olson and M. Cohen, *Stress-assisted isothermal martensitic transformation: Application to TRIP steels,* Metallurgical and Materials Transactions A, Vol. 13, Issue 11, pp. 1907-1914, November 1982.

[42] G.B. Olson and M. Cohen, *A mechanism for the strain-induced nucleation of martensitic transformations,* Journal of the Less Common Metals, Vol. 28, Issue 1, pp. 107-118, March 1972.

[43] K. Eberle, P. Cantinieaus, and Ph. Harlet, *New thermomechanical strategy for production of high strength low alloyed multiphase steel showing transformation induced plasticity effect,* Ironmaking and Steelmaking, Vol. 26, Issue 3, pp. 176-181, May 1999.

[44] B. Gajda, A.K. Lis, *A study of microstructure and phase transformations of CMnAlSi TRIP steel*, Journal of Achievements in Materials and Manufacturing Engineering, Vol. 31, Issue 2, pp. 646-653, December 2008.

[45] K.W. Andrews, *Empirical Formulae for the Calculation of Some Transformation Temperatures*, Journal of the Iron and Steel Institute, Vol. 203, Part 7, pp. 721-727, July 1965.

[46] G.N. Haidemenopoulos, *Austenite stabilization from direct cementite conversion in low-alloy steels*, Steel Research, Vol. 67, pp. 93-99, 1996.

[47] G.N. Haidemenopoulos, and A.N. Vasilakos, *Modelling of austenite stability in low-alloy triple-phase steels,* Steel Research, Vol. 67, pp. 513-519, 1996.

[48] I. B. Timokhina, P. D. Hodgson and E. V. Pereloma, *Effect of microstructure on the stability of retained austenite in transformation-induced-plasticity steels,* Metallurgical and Materials Transactions A, Vol. 35, Issue 8, pp. 2331–2341, August 2004.

[49] G. Krauss, *Steels-Heat Treatment and Processing Principles*, ASM International, Materials Park, OH, 1990.

[50] C.S. Roberts, *Effect of Carbon on the Volume Fractions and Lattice Parameters of Retained Austenite and Martensite*, Trans. AIME: Journal of Metals, pp. 203-204, 1953.

[51] A. Diamatteo, G. Lovicu, M. Desanctis, R. Valentini, A. Solina, *Microstructures and properties of TRansformation Induced Plasticity steels*, Paper presented at the 2nd International Conference HEAT TREATMENT AND SURFACE ENGINEERING IN AUTOMOTIVE APPLICATIONS, Riva del Garda, June 2005.

[52] M. Azrin, G. Olson, R. Gagne, *Inhomogenous deformation and strain-rate effects in high-strength TRIP steels*, Materials Science and Engineering, Vol. 23, Issue 1, pp. 33-41, January 1976.

[53] Y. Tomita, T. Iwamoto, *Constitutive modeling of trip steel and its application to the improvement of mechanical properties*, International Journal of Mechanical Sciences, Vol. 37, Issue 12, pp. 1295-1305, December 1995.

[54] X. Wei, R. Fu, and L. Li, *Tensile deformation behavior of cold-rolled TRIP-aided steels over large range of strain rates*, Material Science and Engineering: A, Vol. 465, Issues 1-2, pp. 260-266, September 2007.

[55] K. Higashi, T. Mukai, K. Kaizu, S. Tsuchida, and S. Tanimura, *THE MICROSTRUCTURAL EVOLUTION DURING DEFORMATION UNDER SEVERAL STRAIN RATES IN A COMMERCIAL 5182 ALUMINIUM ALLOY*, Journal De Physique IV, Vol. 1, pp. C3-347-352, October 1991.

[56] S. Abotula, V.B. Chalivendra, An experimental and numerical investigation of the static and dynamic constitutive behaviour of aluminium alloys, Journal of Strain Analysis for Engineering Design, Vol. 45, Issue 8, pp. 555-565, November 2010.

[57] O. Lademo, O. Engler, A. Benallal, and O. Hopperstad, *Effect of strain rate and dynamic strain ageing on work-hardening for aluminium alloy AA5182-O*, International Journal of Materials Research, Vol. 103, Issue 8, pp. 1035-1041, August 2012.

[58] M. Abbadi, P. Hähner, and A. Zeghloul, *On the characteristics of Portevin-Le Chatelier bands in aluminum alloy 5182 under stress-controlled and strain-controlled tensile testing*, Materials Science and Engineering A, Vol. 337, Issues 1-2, pp. 194-201, November 2002.

[59] R.C. Picu, G. Vincze, F. Ozturk, J.J. Gracio, F. Barlat, and A.M. Maniatty, *Strain rate sensitivity of commercial aluminum alloy AA5182-O*, Materials Science and Engineering: A, Vol. 390, Issues 1-2, pp. 334-343, January 2005.

[60] P.G. McCormick, *A model for the Portevin-Le Chatelier effect in substitutional alloys*, Acta Metallurgica, Vol. 20, Issue 3, pp. 351-354, March 1972.

[61] A. Van den Beukel, *Theory of the effect of dynamic strain aging on mechanical properties*, Physica Status Solidi (a), Vol. 30, Issue 1, pp. 197-206, July 1975.

[62] K. Chihab, Y. Estrin, L.P. Kubin, and J. Vergno, The kinetics of the Portevin-Le Chatelier bands in an Al-5at%Mg alloy, Scripta Metallugica, Vol. 21, Issue 2, pp. 203-208, February 1987.

[63] A. Kalk, Ch. Schwink, *On dynamic strain aging and the boundaries of stable plastic deformation studied on Cu-Mn polycrystals*, Philosophical Magazine A, Vol. 72, Issue 2, pp. 315-339, January 1995.

[64] A. Kalk, Ch. Schwink, *On Sequence of Alternate Stable and Unstable Regions along Tensile Deformation Curves*, Physica Status Solidi (b), Vol. 172, Issue 1, pp. 133-144, July 1992.

[65] H. Ait-Amokhtar and C. Fressengeas, *Crossover from continuous to discontinuous propagation in the Portevin-Le Chatelier effect*, Acta Materialia, Vol. 58, Issue 4, pp. 1342-1349, February 2010.

[66] Ch. Schwink, A. Nortmann, *The present experimental knowledge of dynamic strain ageing in binary f.c.c solid solutions*, Materials and Engineering A, Vol. 234-236, pp. 1-7, August 1997.

[67] F. Kabirian, A. S. Khan, A. Pandey, *Negative to positive strain rate sensitivity in 5xxx series aluminum alloys: Experiment and constitutive modeling*, International Journal of Plasticity, Vol. 55, pp. 232-246, April 2014.

[68] SimTech Simulation et Technologie, Introduction to sheet metal forming process, SIMTECH, 37 rue des Acacias, 75017, Paris, France, 1999.

[69] W.T. Lankford, S.C. Snyder, J.A. Bausher, New criteria for predicting the press performance of deep drawing sheets, Trans. ASM, Vol. 42, pp. 1197–1205, 1950.

[70] W.F. Hosford, R.M. Caddell, Metal Forming Mechanics and Metallurgy, Second Edition, PTR Prentice Hall, Englewood Cliffs, pp. 309-325, 1993.

[71] G. Charca Ramos, M. Stout, R.E. Bolmaro, J.W. Signorelli, P. Turner, *Study of a drawing-*

quality sheet steel. I: Stress/strain behaviors and Lankford coefficients by experiments and micromechanical simulations, International Journal of Solids and Structures, Vol. 47, Issue 17, pp. 2285-2293, August 2010.

[72] R. Pearce, Some aspects of anisotropic plasticity in sheet metals, International Journal of Mechanical Sciences, Vol. 10, Issue 12, pp. 995-1004, December 1968.

[73] R. Pearce, P.G. Joshi, *Uniaxial and Biaxial Tension*, ASM Transactions Quarterly, Vol. 57, pp. 399-413, 1964.

[74] R. Pearce and C.H. Bott, Journal of Australian Institute of Metals, Vol. 12, pp. 119, 1964.

[75] R. Heyer and J. Newby, *Effects of Mechanical Properties on Biaxial Stretchability of Low Carbon Steels*, SAE Technical Paper 680094, 1968.

[76] R.A.C. Filho, L.M.V. Tigrinho, R.C.B. Neto, and P.V.P. Marcondes , *An experimental approach for blankholder force determination for DP600 with different material flow strain rates in the flange during stamping*, Proceedings of the Institution of Mechanical Engineers, Part B: Journal of Engineering Manufacture, Vol. 227, Issue 3, pp. 417-422, March 2013.

[77] W. Wang, C. He, Z. Zhao, and X. Wei, *The limit drawing ratio and formability prediction of advanced high strength dual-phase steels*, Materials & Design, Vol. 32, Issue 6, pp. 3320-3327, June 2011.

[78] S.K. Panda, J. Li, V.H.B. Hernandez, Y. Zhou, F. Goodwin, *Effect of weld location, orientation, and strain path on forming behavior of AHSS tailor welded blanks*, Journal of Engineering Materials and Technology, Vol. 132, Issue 4, October 2010.

[79] A. Nasser, A. Yadav, P. Pathak, and T. Altan, *Determination of the flow stress of five AHSS sheet materials (DP600, DP780, DP780-CR, DP780-HY and TRIP780) using the uniaxial tensile and the biaxial Viscous Pressure Bulge (VPB) tests*, Journal of Materials Processing Technology, Vol. 210, Issue 3, pp. 429-436, February 2010.

[80] M. Dunand, D. Mohr, *Hybrid experimental-numerical analysis of basic ductile fracture experiments for sheet metals*, International Journal of Solids and Structures, Vol. 47, Issue. 9, pp. 1130-1143, May 2010.

[81] M.C. Butuc, G.T. Vincze, J.J. Gracio, A.B. Rocha, *A comparative study between strain and stress based forming limit analysis by applying several phenomenological yield criteria*, AIP Conference Proceedings, Vol. 778, Issue 1, pp. 272-277, August 2005.

[82] J.C. Brem, F. Barlat, R.E. Dick, J.W. Yoon, *Characterization of Aluminum Alloy Sheet Materials, AIP Conference Proceedings*, Vol. 778, Issue 1, pp. 1179-1190, August 2005.

[83] J. Huh, H. Huh, C.S. Lee, *Effect of strain rate on plastic anisotropy of advanced high strength*

steel sheets, International Journal of Plasticity, Vol. 44, pp. 23-46, May 2013.

[84] H. Huh, J.H. Lim, S.H. Park, *High speed tensile test of steel sheets for the stress-strain curve at the intermediate strain rate*, International Journal of Automotive Technology, Vol. 10, Issue 10, pp. 195-204, April 2009.

[85] H. Kolsky, *An investigation of the mechanical properties of materials at very high rates of loading*, Proceedings of the Physical Society of London, Volume 62B, pp. 676-700, March 1949.

[86] G.B. Dudder, *Drop Tower Compression Test,* Metals Handbood, 9th Edition, American Society for Metals, pp. 196-199, 1985.

[87] D.R. Ambur, C. Prasad, W.A. Waters Jr., *A dropped-weight apparatus for low-speed impact testing of composite structures*, Experimental Mechanics, Vol. 35, Issue 1, pp. 77-82, March 1995.

[88] J.B. Hawkyard, C. Highton, P.H. Lo, *A wedge plastometer for hot multistage compression testing*, Journal of Mechanical Working Technology, Vol. 1, Issue 3, pp. 291-298, February 1978.

[89] R. Bouix, P. viot, J.L. Lataillade, Polypropylene foam behaviour under dynamic loadings: Strain rate, density and microstructure effects, International Journal of Impact Engineering, Vol. 36, Issue 2, pp. 329-342, February 2009.

[90] K. Miura, S. Takagi, T. Hira, O. Furukimi, S. Tanimura, *High Strain Rate Deformation of High Strength Sheet Steels for Automotive Parts*, SAE Technical Paper 980952, 1998.

[91] L. Djapic Oosterkamp, A. Ivankovic, G. Venizelos, *High strain rate properties of selected aluminium alloys*, Materials Science and Engineering: A, Vol. 278, Issue 1-2, pp. 225-235, February 2000.

[92] A. Bardelcik, *High Strain Rate Behaviour of Hot Formed Boron Steel with Tailored Properties*, PhD thesis, University of Waterloo, Waterloo, Ontario, Canada, 2012.

[93] A. Bardelcik, M.J. Worswick, and M.A. Wells, *The Influence of Martensite, Bainite and Ferrite on the As-Quenched Constitutive Response of Simultaneously Quenched and Deformed Boron Steel – Experiments and Model*, Materials and Design, Vol. 55, pp. 504-525, March 2014.

[94] High Strain Rate Material Behavior, Forming and Impact Mechanics Research group website. Retrieved October 4, 2014, from: http://www.formingandimpact.uwaterloo.ca/Research/strain.html.

[95] G.T. (Rusty) Gray III, *Classic Split-Hopkinson Pressure Bar Testing*, In: ASM Handbook-Mechanical Testing and Evaluation, Vol. 8, pp. 462-476, H. Kuhn, D. Medlin (Ed), ASM

International, Materials Park, OH, 2000.

[96] B. Hopkinson, *A Method of Measuring the Pressure Produced in the Detonation of High Explosives or by the Impact of Bullets*, Proceedings of The Royal Society-A Mathematical Physical and Engineering Sciences, Vol. 213, pp. 437-456, November 1914.

[97] U.S. Lindholm, L.M. Yeakley, *High strain-rate testing: Tension and compression*, Experimental Mechanics, Vol. 8, Issue 1, pp. 1-9, January 1968.

[98] P.S. Follansbee, *The Hopkinson Bar,* Metals Handbook, ASM, Vol. 8, pp. 198-203, 1978.

[99] T. Yokoyama, K. Kishida, *A novel impact three-point bend test method for determining dynamic fracture-initiation toughness*, Experimental Mechanics, Vol. 29, Issue 2, pp. 188-194, June 1989.

[100] T. Nicholas, *Tensile testing of materials at high rates of strain*, Experimental Mechanics, Vol. 21, Issue 5, pp. 177-185, May 1981.

[101] G.H. Staab and A. Gilat, *A direct-tension split Hopkinson bar for high strain-rate testing*, Experimental Mechanics, Vol. 31, Issue 3, pp. 232-235, September 1991.

[102] A. Bardelcik, C.P. Salisbury, S. Winkler, M.A. Wells, M.J. Worswick, *Effect of Cooling Rate on the High Strain Rate Properties of Boron Steel*, International Journal of Impact Engineering, Vol. 37, Issue 6, pp. 694-702, July 2010.

[103] A. Bardelcik, M.J. Worswick, S. Winkler, and M.A. Wells, *A strain rate sensitivity constitutive model for quenched steel with tailored properties*, International Journal of Impact Engineering, Vol. 50, pp. 49-62, December 2012.

[104] V.T. Kuokkala, M. Apostol, M. Hokka, *High and Low Temperature Techniques in Hopkinson Split Bar Testing*, Proceedings of the IMPLAST 2010 Conference, Society for Experimental Mechanics. October 2010.

[105] M. Quik, K. Labibes, C. Albertini, T. Valentin, and P. Magain, *Dynamic Mechanical Properties of Automotive Thin Sheet Steel in Tension, Compression and Shear*, Journal de Physique IV France, Vol. 7, Number C3, pp. 379-384, August 1997.

[106] V. Tarigopula, O.S. Hopperstad, M. Langseth, A.H. Clausen, F. Hild, *A study of localisation in dual-phase high-strength steels under dynamic loading using digital image correlation and FE analysis*, International Journal of Solids and Structures, Vol. 45, pp. 601-619, September 2007.

[107] P. Verleysen, J. Peirs, J.V. Slycken, K. Faes, L. Duchene, *Effect of strain rate on the forming behaviour of sheet metals*, Journal of Materials Processing Technology, Vol. 211, Issue 8, pp. 1457-1464, August 2011.

[108] P.S. Follansbee and C. Frantz, *Wave Propagation in the Split Hopkinson Pressure Bar*, Journal

of Engineering Materials and Technology, Vol. 105, Issue 1, pp. 61-66, September 2009.

[109] R.M. Davies, *Stress waves in solids*, British Journal of Applied Physics, Vol. 7, Issue 6, pp. 203-209, June 1956.

[110] J.A.M. Clarke, *High Strain Rate Tensile Testing*, Master of Applied Science thesis, Carleton University, Ottawa, Ontario, Canada, 1993.

[111] S. Lang, *Design of a split Hopkinson bar apparatus for use with fiber reinforced composite materials*, Master of Science in Mechanical Engineering thesis, Utah State University, Logan, Utah, USA, 2012.

[112] S. Kurukuri, A. Bardelcik, M.J. Worswick, R.K. Mishra, and J.T. Carter, *High strain rate characterization of ZEK100 magnesium rolled alloy sheet*, EPJ Web of Conference, Vol. 26, pp. 01042, August 2012.

[113] M. Hokka, K. Ostman, J. Ramo, V.T. Kuokkala, *High Temperature Tension HSB Device based on Direct Electrical Heating*, Dynamic Behavior of Materials Vol. 1, Proceedings of the 2014 Annual Conference on Experiment and Applied Mechanics, Ed: B. Song, D. Casem, J. Kimberley, Society for Experimental Mechanics Series, 2014.

[114] L. Pochhammer, *About the initiation of the velocities of small oscillations in unbounded isotropic circular cylinders*, Journal Reine Angew Mathematica, Vol. 81, pp. 324-336, 1876.

[115] C. Chree, *The equations of an isotropic elastic solid in polar and cylindrical co-ordinates: their solution and application*, Transactions of the Cambridge Philosophical Society, Vol. 41, pp. 250-369, 1889.

[116] E.D.H. Davies and S.C. Hunter, *The dynamic compression testing of solids by the method of the split Hopkinson pressure bar*, Journal of the Mechanics and Physics of Solids, Vol. 11, Issue 3, pp. 155-179, June 1963.

[117] W. Chen, B. Song, D.J. Frew, and M.J. Forrestal, *Dynamic small strain measurements of a metal specimen with a split Hopkinson pressure bar,* Experimental Mechanics, Vol. 43, Issue 1, pp. 20-23, March 2003.

[118] G.T. Gray III, S.R. Chen, W. Wright and M.F. Lopez, *Constitutive equations for annealed metals under compression at high strain rates and high temperatures*, Report LA-12669-MS, Los Alamos National Laboratory, 1994.

[119] P. Pelletier, *Mechanical Behaviour of Armco Iron at High Strain Rates and Elevated Temperature*, Masters of Applied Science Thesis, Carleton University, 1995.

[120] R. Liang and A.S. Khan, *A critical review of experimental results and constitutive models for BCC and FCC metals over a wide range of strain rates and temperatures*, International Journal

of Plasticity, Vol. 15, Issue 9, pp. 963-980, February 1999.

[121] P.V. Sivaprasad, S. Venugopal, S. Venkadesan, *Tensile flow and work-hardening behavior of a Ti-modified austenitic stainless steel*, Metallurgical and Materials Transactions A, Vol. 28, Issue 1, pp. 171-178, January 1997.

[122] Y. Estrin, H. Mecking, *A unified phenomenological description of work hardening and creep based on one-parameter models*, Acta Metallurgica, Vol. 32, Issue 1, pp. 57-70, January 1984.

[123] M. Naderi, L. Durrenberger, A. Molinari, W. Bleck, *Constitutive relationships for 22MnB5 boron steel deformed isothermally at high temperatures*, Materials Science and Engineering: A, Vol. 478, Issues 1-2, pp. 130-139, April 2008.

[124] D.M. Bissot, *Development of a Constitutive Equation for HSLA-1000 at Cryogenic Temperatures*, Master's thesis, Naval Postgraduate School, Monterey, California, USA, December 1987.

[125] J.B. Conway, R.H. Stentz, J.T. Berling, *Fatigue, Tensile, and Relaxation behavior of Stainless Steels,* Technical Information Centre, Office of Information Service, United States Atomic Energy Commission, 1975.

[126] U.F. Kocks, *Laws for Work-Hardening and Low-Temperature Creep*, Journal of Engineering Materials and Technology, Vol. 98, pp. 76-85, January 1976.

[127] G.T. Camacho, M. Ortiz, *Adaptive lagrangian modelling of ballistic penetration of metallic targets*, International Journal of Comp Meth Appl Mech Engng, Vol. 142,Issues 3-4 pp. 269-301, 1997.

[128] T. Børvik, O.S. Hopperstad, T. Berstad, M. Langseth, *A computational model of viscoplasticity and ductile damage for impact and penetration*, European Journal of Mechanics A/Solids, Vol. 20, Issue 5 pp. 685-712, 2001.

[129] R. Gray III, ASM Handbook: mechanical testing and evaluation, Material Park, OH, ASM International, 2000.

[130] C.P. Salisbury, *Spectral analysis of wave propagation through a polymeric Hopkinson bar*, Master of Applied Science thesis, University of Waterloo, Waterloo, ON, Canada, 2001.

[131] J.W. Dally, W.F. Riley, *Experimental stress analysis*, 3rd Edition, New York, Montreal, McGraw-Hill, 1991.

[132] Y.H. Wang, J.H. Jiang, C. Wanintrudal, C. Du, D. Zhou, L.M. Smith and L.X. Yang, *WHOLE FIELD SHEET-METAL TENSILE TEST USING DIGITAL IMAGE CORRELATION*, Experimental Techniques, Vol. 34, Issue 2, pp. 54-59, March/April 2010.

[133] M.A. Sutton, J.J. Orteu, H.W. Schreier, *Image Correlation for Shape, Motion and Deformation*

Measurements, Springer Science+Business Media, LLC, New York, USA, 2009.

[134] L. Yang, L. Smith, A. Gothekar, X. Chen, *Measure Strain Distribution Using Digital Image Correlation (DIC) for Tensile Tests*, Final Report, The Advanced High Strength Steel Stamping Team of the Auto/Steel Partnership (A/SP), Department of Mechanical Engineering, Oakland University, MI, January 2010.

[135] D. MacDougall, *Determination of the Plastic Work Converted to Heat Using Radiometry,* Experimental Mechanics, Vol. 40, Issue 3, pp. 298-306, September 2000.

[136] LS-DYNA keyword user's manual, Vol. III – material model, Livermore Software Technology Corporation, California, USA, 2012.

[137] P.W. Bridgman, *Studies in Large Plastic Flow and Fracture*, McGraw-Hill, 1952.

[138] Y. Ling, *Uniaxial true stress-strain after necking*, AMP Journal of Technology, Vol. 5, pp. 37-48, June 1996.

APPENDICES

Appendix A

Engineering stress-strain curves

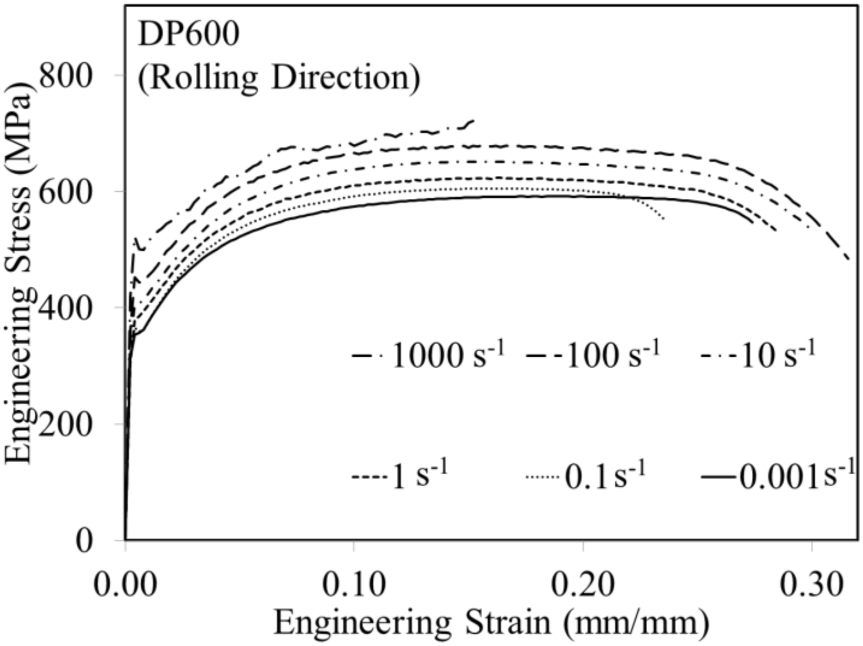

Figure A.1: Averaged engineering stress vs. strain curves for DP600 sheet specimens at room temperature and strain rates from 0.001 s^{-1} to 1000 s^{-1} along rolling direction.

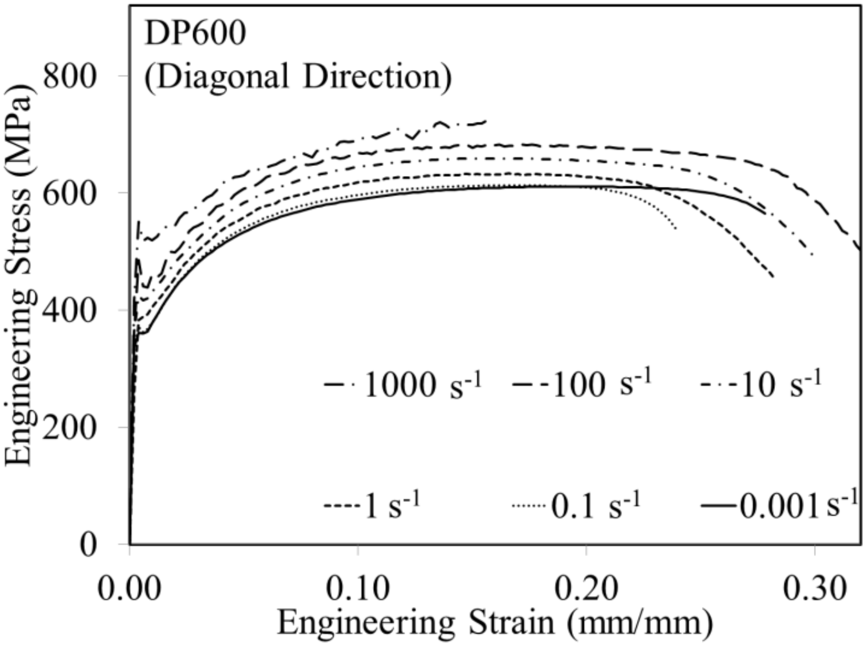

Figure A.2: Averaged engineering stress vs. strain curves for DP600 sheet specimens at room temperature and strain rates from 0.001 s^{-1} to 1000 s^{-1} along diagonal direction.

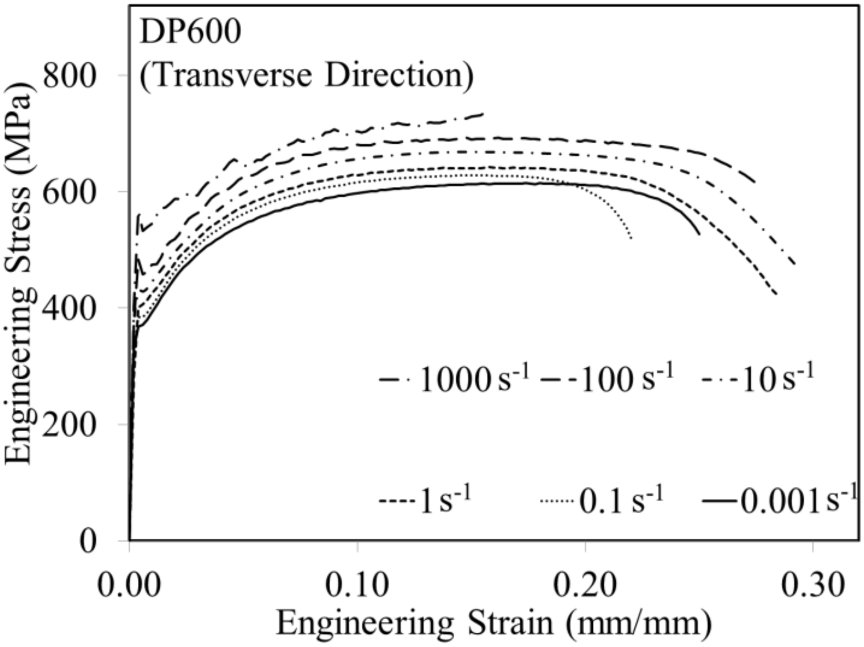

Figure A.3: Averaged engineering stress vs. strain curves for DP600 sheet specimens at room temperature and strain rates from 0.001 s^{-1} to 1000 s^{-1} along transverse direction.

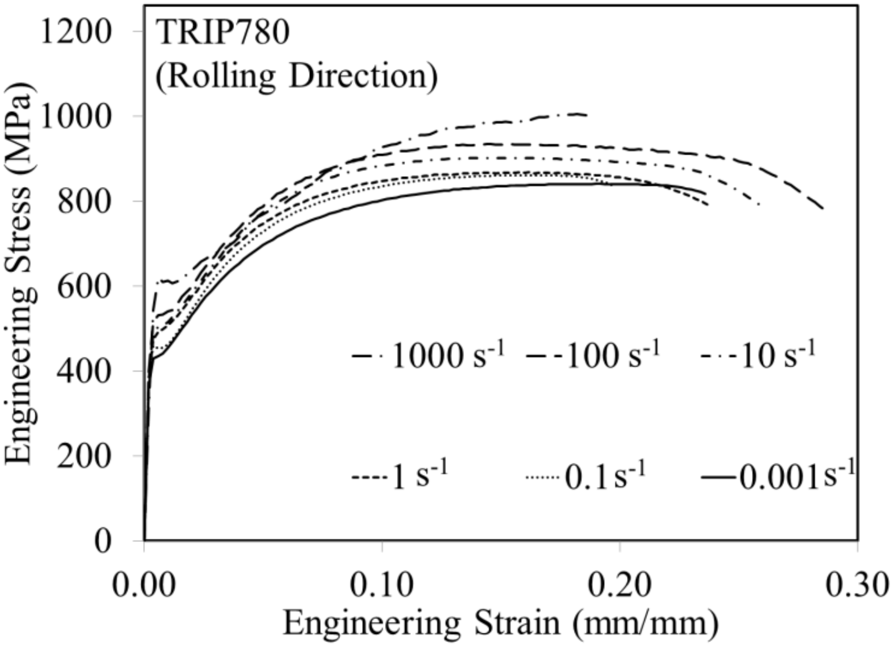

Figure A.4: Averaged engineering stress vs. strain curves for TRIP780 sheet specimens at room temperature and strain rates from 0.001 s^{-1} to 1000 s^{-1} along rolling direction.

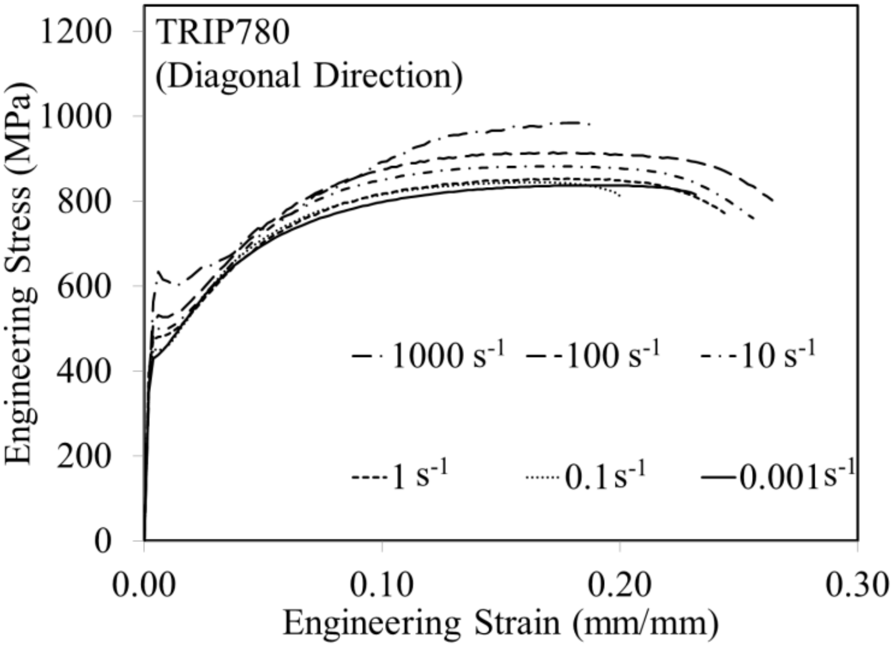

Figure A.5: Averaged engineering stress vs. strain curves for TRIP780 sheet specimens at room temperature and strain rates from 0.001 s^{-1} to 1000 s^{-1} along diagonal direction.

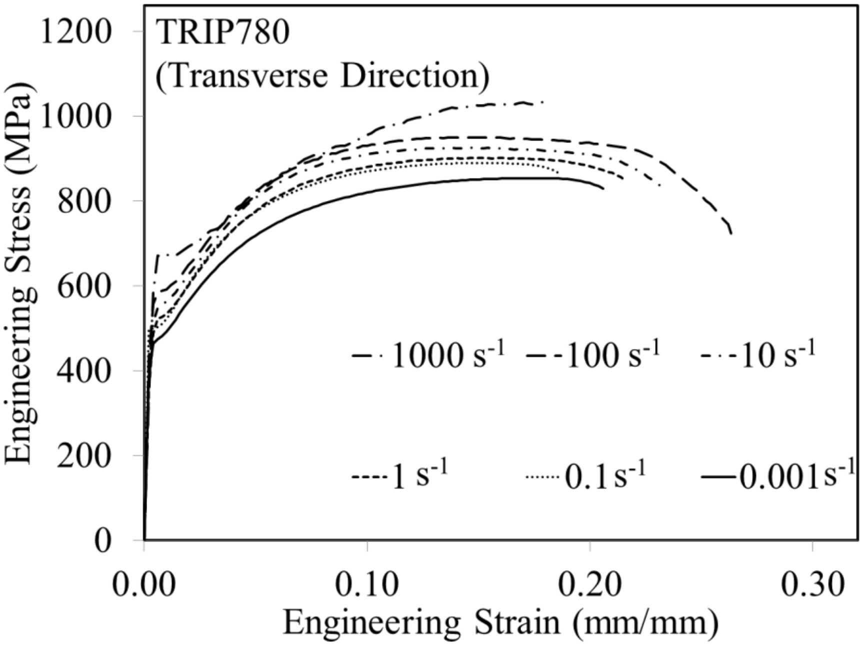

Figure A.6: Averaged engineering stress vs. strain curves for TRIP780 sheet specimens at room temperature and strain rates from 0.001 s^{-1} to 1000 s^{-1} along transverse direction.

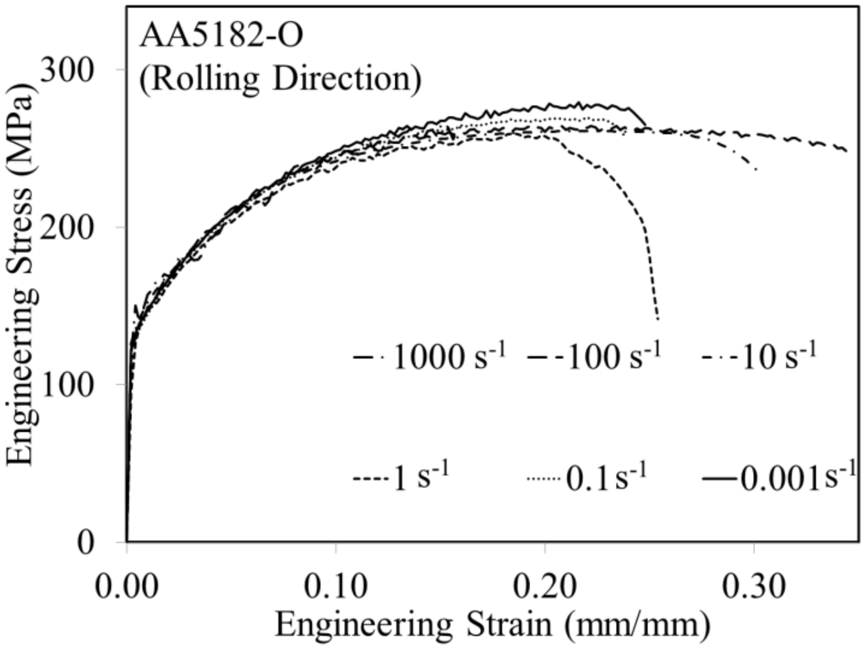

Figure A.7: Averaged engineering stress vs. strain curves for AA5182-O sheet specimens at room temperature and strain rates from 0.001 s^{-1} to 1000 s^{-1} along rolling direction.

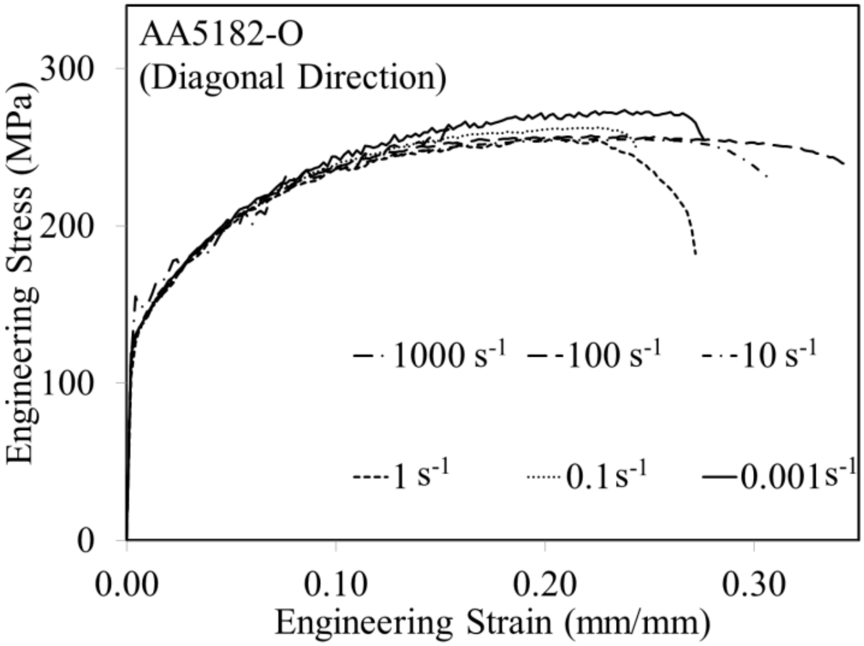

Figure A.8: Averaged engineering stress vs. strain curves for AA5182-O sheet specimens at room temperature and strain rates from 0.001 s^{-1} to 1000 s^{-1} along diagonal direction.

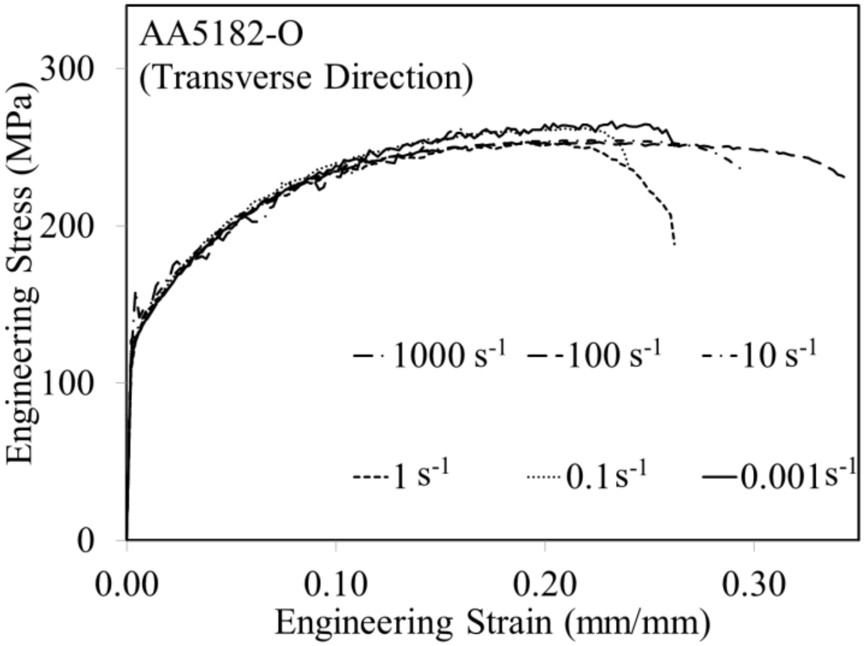

Figure A.9: Averaged engineering stress vs. strain curves for AA5182-O sheet specimens at room temperature and strain rates from 0.001 s^{-1} to 1000 s^{-1} along transverse direction.

Appendix B

Supplemental FEA results

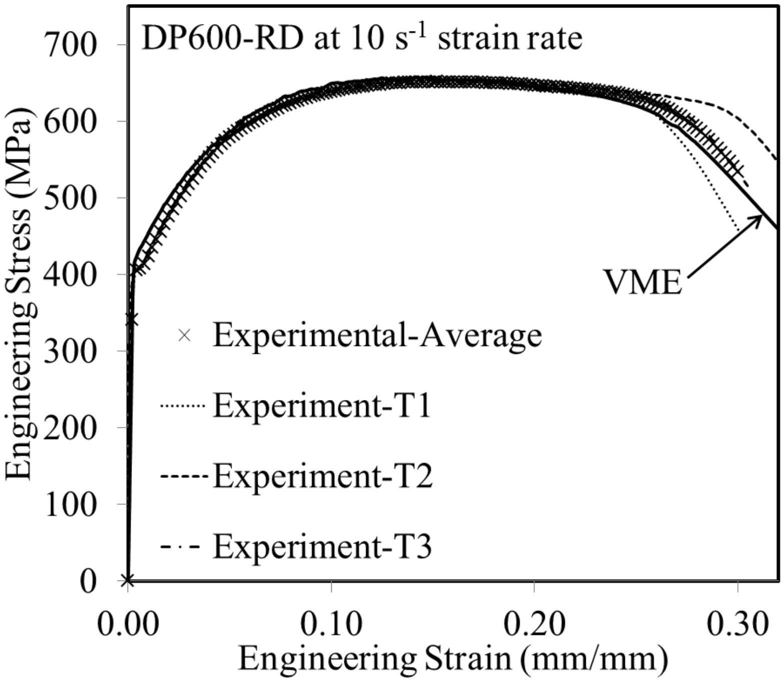

Figure B.1: Measured and predicted (solid lines) engineering stress vs. strain curves using VME model for DP600-RD at 10 s^{-1} strain rate.

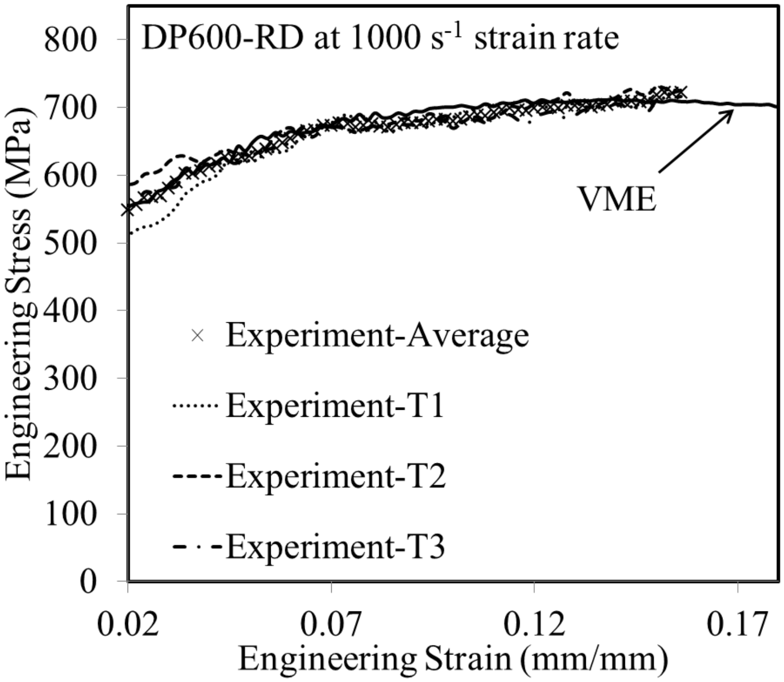

Figure B.2: Measured and predicted (solid lines) engineering stress vs. strain curves using VME model for DP600-RD at 1000 s^{-1} strain rate.

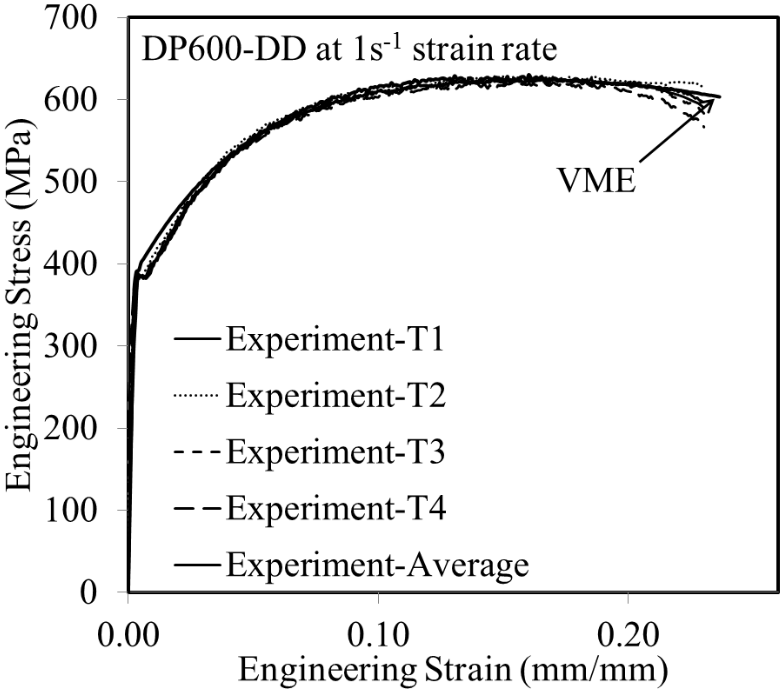

Figure B.3: Measured and predicted (solid lines) engineering stress vs. strain curves using VME model for DP600-DD at 1 s^{-1} strain rate.

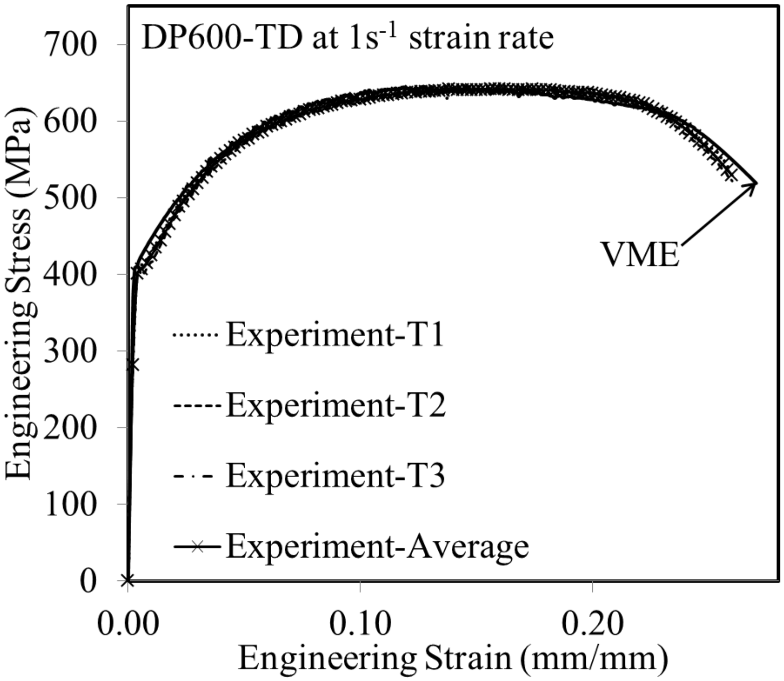

Figure B.4: Measured and predicted (solid lines) engineering stress vs. strain curves using VME model for DP600-TD at 1 s^{-1} strain rate.

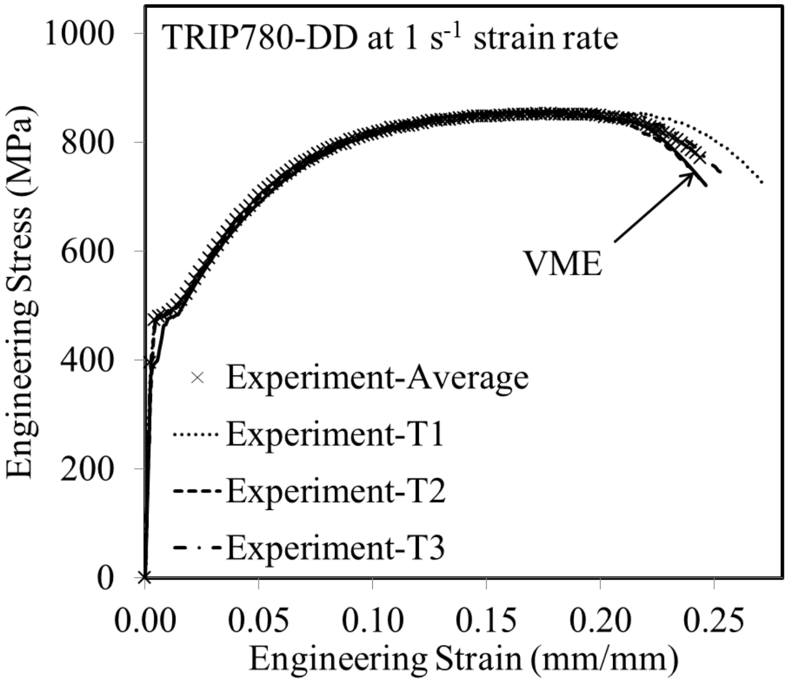

Figure B.5: Measured and predicted (solid lines) engineering stress vs. strain curves using VME model for TRIP780-DD at 1 s^{-1} strain rate.

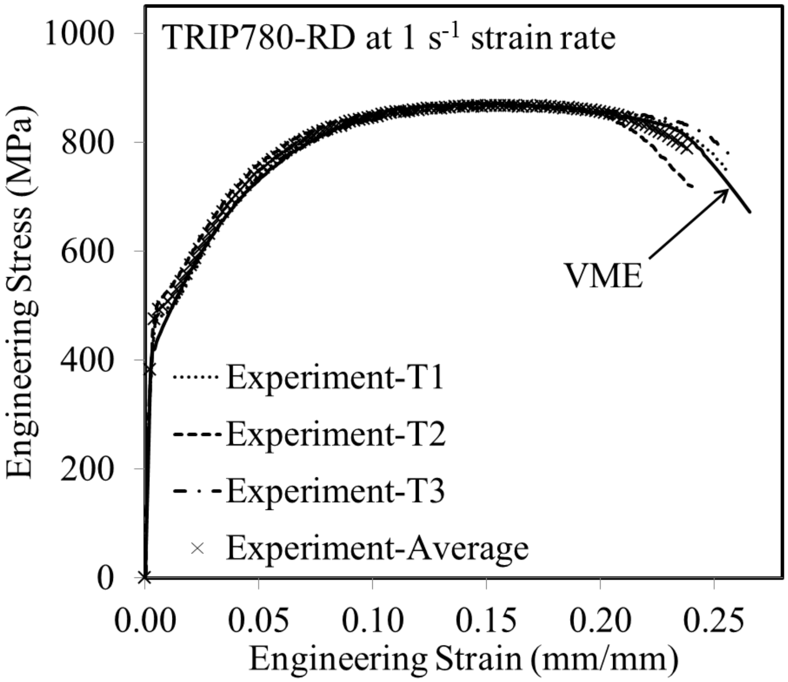

Figure B.6: Measured and predicted (solid lines) engineering stress vs. strain curves using VME model for TRIP780-RD at 1 s^{-1} strain rate.

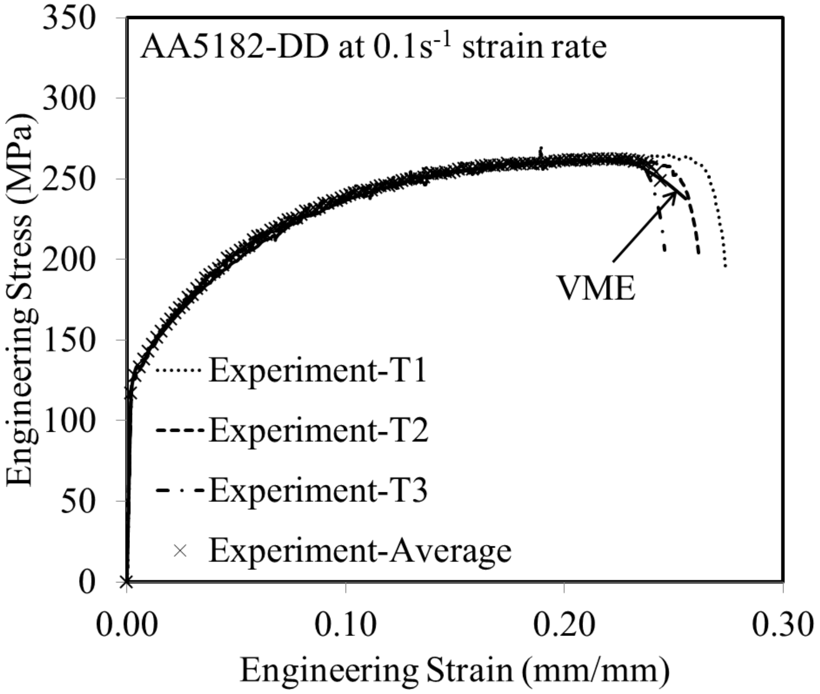

Figure B.7: Measured and predicted (solid lines) engineering stress vs. strain curves using VME model for AA5182-O-DD at 0.1 s^{-1} strain rate.

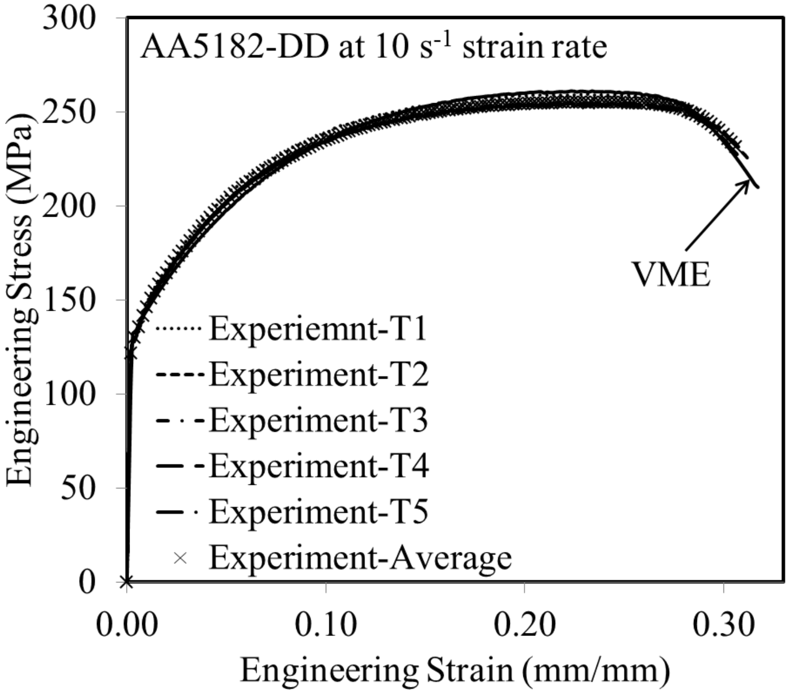

Figure B.8: Measured and predicted (solid lines) engineering stress vs. strain curves using VME model for AA5182-O-DD at 10 s^{-1} strain rate.

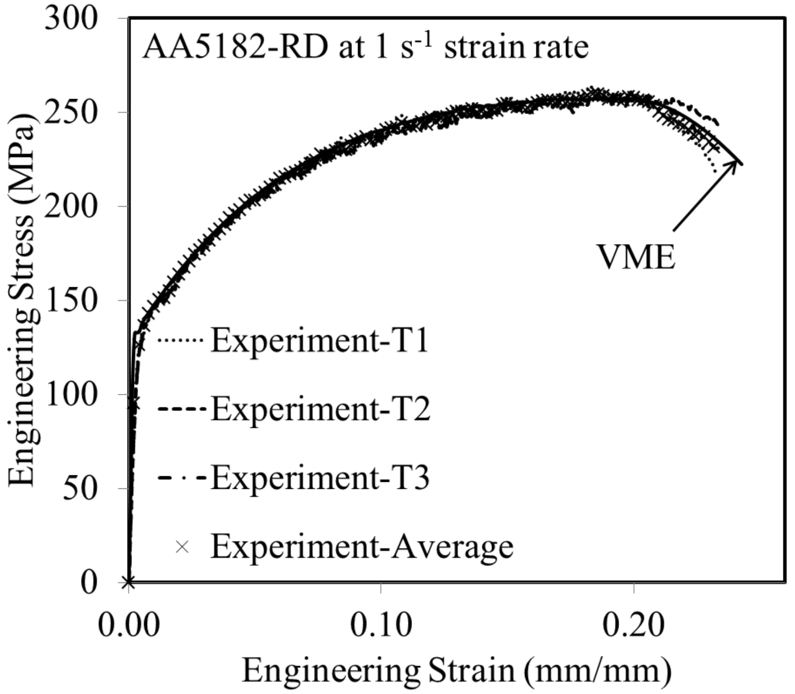

Figure B.9: Measured and predicted (solid lines) engineering stress vs. strain curves using VME model for AA5182-O-RD at 1 s^{-1} strain rate.

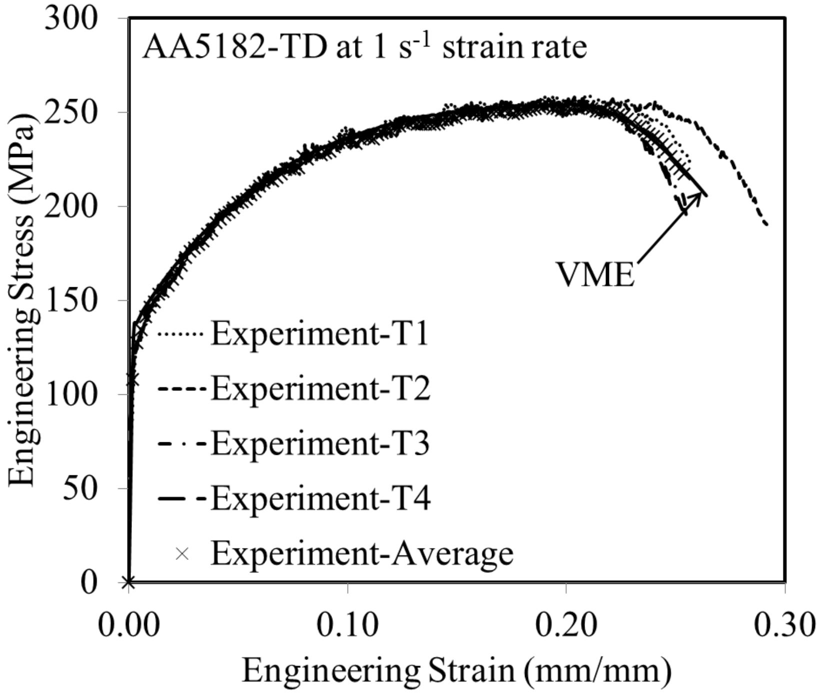

Figure B.10: Measured and predicted (solid lines) engineering stress vs. strain curves using VME model for AA5182-O-TD at 1 s^{-1} strain rate.